



Universidade do Porto

**FEUP** Faculdade de Engenharia



• U



C •

# *Study of Dimensionally Stable Anodes for Chlor-Alkali Electrolysis*

Dissertation presented for the Doctor of Philosophy degree in  
Engineering of Refining, Petrochemistry and Chemistry

by

**João Fernando de Andrade Cardoso da Silva**

**Supervisors:** Professor Adélio Mendes

Professor Christopher Brett

**Enterprise Coordinator:** Doctor Paulo Araújo

Porto, February 2016



This work was financially supported by the projects POCI-01-0145-FEDER-006939 - Laboratory for Process Engineering, Environment, Biotechnology and Energy – LEPABE and NORTE-01-0145-FEDER-000005 – LEPABE-2-ECO-INNOVATION, funded by FEDER funds through COMPETE2020 - Programa Operacional Competitividade e Internacionalização (POCI) and Programa Operacional Regional do Norte (NORTE2020) and by national funds through FCT - Fundação para a Ciência e a Tecnologia; PhD grant co-sponsored by CUF-QI and FCT (SFRH/BDE/51398/2011)



UNIÃO EUROPEIA  
Fundos Europeus  
de Desenvolvimento Regional





## Agradecimentos

Em primeiro lugar gostaria de agradecer ao meu orientador, Professor Adélio Mendes. Obrigado pelas condições que me disponibilizou, os desafios que lançou e conhecimento que partilhou. E obrigado, sobretudo pela paciência e o ânimo que me transmitiu quando mais foi preciso.

Agradeço ao meu co-orientador, Professor Christopher Brett, a disponibilidade que sempre demonstrou, o conhecimento que transmitiu e as discussões que promoveu.

Agradeço à empresa CUF-QI e à FCT oportunidade de desenvolver este projeto em meio industrial. Este primeiro contacto com a indústria foi com certeza, uma mais valia no meu desenvolvimento profissional e pessoal. Agradeço ao Coordenador empresarial, Doutor Paulo Araújo, as condições e os recursos que proporcionou para que este projeto tivesse sido possível. Aos colegas do DTEPD Alejandro, Dulce, Fernando, Hugo, Rui, pelo bom ambiente criado e pelas agradáveis discussões promovidas. Aos colegas da Manutenção, Zé, Rosas, Sebastião, Júlio, ao Ramos e Fernando, agradeço os possíveis e os impossíveis que fizeram, nas muitas vezes a que a eles recorri. A sua criatividade e empenho não têm limites. Um agradecimento especial à Catarina pelo incansável apoio técnico, alento e dedicação a este projeto.

À “Família Palacete” – À Anabela, Ana Leonor, Clara, João, José Gomez, Dionísio, Daniela, Diogo, Daniel, Joana Duarte, Joana Azevedo, Juliana, Rita, Sérgio, Sofia, Tiago obrigado pelos convívios, desabafos e boleias! Convosco vivi momentos que jamais esquecerei!

A todos os amigos da FEUP, em particular aqueles que acompanharam mais de perto este projeto e ouviram os meus desabafos - José, Erica, André, Paula e Catarina.

Aos colegas do Grupo de Corrosão e Eletroquímica, obrigado por ter sido tão bem recebido e acompanhado nos meus primeiros passos no mundo da eletroquímica. Agradeço aos muito colegas do LEPABE que contribuíram para que este projeto se torna-se realidade!

À Margarida Catarino que mais do que uma colega, foi uma amiga! Genuína, incansável e sempre disponível para ajudar. Foi um privilégio ter-te colega!

Um grande obrigado à minha família! Nesta longa e difícil jornada nunca me desamparou e sempre acreditou em mim! Mãe, Pai, Belinha, Du, obrigado pela paciência, pelo carinho e compreensão que tão importante foram nesta fase!

À Mariana! Que o destino fez cruzar-se comigo nomeio desta aventura! Obrigado pela muita paciência, pelo carinho e pelos inesgotáveis mimos com que sempre me tens prendado!

## Resumo

O processo cloro-álcalis é um dos processos químicos com maior consumo energético. A energia requerida por uma célula cloro-álcalis aumenta com o tempo devido à desativação dos eletrodos, particularmente do ânodo dimensionalmente estável (DSA®). A determinação do tempo ótimo de substituição ou revestimento do ânodo são, pois, da máxima importância, no entanto requerem informação do estado dos ânodos que não é disponibilizada pelos meios de monitorização instalados nas células cloro-alcálicas.

O objetivo deste trabalho é desenvolver conhecimento sobre os processos de desativação de ânodos DSA® comerciais com recurso a técnicas eletroquímicas - curvas de polarização, voltametria cíclica e espectroscopia de impedância eletroquímica (EIS) – e técnicas de caracterização de superfície – SEM, EDS e XPS. Devido à sensibilidade da EIS, a obtenção de espectros sem ruído e perturbações só foi possível após o desenvolvimento de uma nova célula eletroquímica. Nesta célula, o ânodo é colocado na base e a agitação é promovida por um agitador mecânico. Com base na informação de curvas de polarização e EIS obtida nesta célula, propõem-se o mecanismo de Volmer-Tafel-Heyrovsky para descrever a cinética da reação de cloro num ânodo DSA® revestido com  $\text{TiO}_2\text{-RuO}_2\text{-IrO}_2$ .

O desempenho do ânodo DSA® foi avaliado por via de um teste de envelhecimento rápido. O teste mostrou a elevada estabilidade do ânodo durante as primeiras 3586 h do teste, não obstante as agressivas condições de operação. Apesar das análises EDS e XPS mostrarem a perda de ruténio e irídio, a atividade do ânodo mostrou-se inalterável durante as primeiras 3586 h do teste. A partir das 3586 h, a redução da densidade de corrente e alteração dos espectros de impedância evidenciaram o início da perda de atividade do ânodo. Neste trabalho, propõe-se um mecanismo de desativação de ânodos DSA® baseado na formação de uma camada passiva de  $\text{TiO}_2$  na interface substrato-revestimento. Esta é consequência da erosão e dissolução do revestimento que promovem um fácil acesso do eletrólito ao interior do revestimento até atingir o substrato.

A metodologia desenvolvida e o conhecimento sobre a cinética da reação de cloro e mecanismos de desativação de ânodos DSA® à escala laboratorial são um importante passo para a previsão do comportamento de ânodos industriais.



## Abstract

The chlor-alkali process is one of the most energy demanding processes in the chemical industry. The electricity consumption in a chlor-alkali cell increases as a function of time due to deactivation processes occurring on the cell elements, particularly on the anode - a dimensionally stable anode (DSA<sup>®</sup>). The minimization of this deactivation and the optimum time for replacement or recoating of the anode is of critical importance and requires information about the deactivation processes occurring during chlorine evolution.

This work aims to study the failure mechanisms of commercial DSA<sup>®</sup> anodes, combining electrochemical techniques, namely polarisation curves, cyclic voltammetry and electrochemical impedance spectroscopy with surface characterisation techniques (SEM, EDS and XPS). Due to the sensitivity of the electrochemical impedance spectroscopy technique, accurate spectra free from noise were only possible to obtain after developing a new electrochemical cell. In this cell, the anode is placed horizontally at the bottom of the cell and the electrolyte is mechanically stirred. Based on the information from the polarisation curves and electrochemical impedance spectroscopy, a Volmer-Tafel-Heyrovsky mechanism with an equilibrium Volmer step was proposed to describe the kinetics of chlorine evolution on a commercial TiO<sub>2</sub>-RuO<sub>2</sub>-IrO<sub>2</sub> DSA<sup>®</sup> anode.

An accelerated ageing test showed the high stability and activity of the DSA<sup>®</sup> anode during the first 3586 h. Despite the reduction of ruthenium and iridium content, deduced from EDS and XPS analyses, a reduction of the anode activity, was only observed after 3586 h. Until this time, the reduction of iridium and ruthenium content was compensated by increased contact between the coating and electrolyte. Although the loss of ruthenium and iridium by dissolution and the mechanical erosion of the coating both contribute to DSA<sup>®</sup> deactivation, the impedance measurements gave strong evidence that the growth of a TiO<sub>2</sub> passive layer at the substrate-coating interface is the main cause of anode performance loss.

The methodology used in this work and the knowledge acquired concerning the kinetics and degradation mechanisms of DSA<sup>®</sup> anodes at the laboratory scale, are valuable assets that will be useful for predicting the behaviour of industrial anodes.



# List of Contents

<b>LIST OF FIGURES</b> .....	<b>V</b>
<b>LIST OF TABLES</b> .....	<b>IX</b>
<b>NOTATION</b> .....	<b>XI</b>
<b>1 INTRODUCTION</b> .....	<b>1</b>
1.1 THE HISTORY OF CHLORINE AND SODIUM HYDROXIDE .....	1
1.2 THE ELECTROCHEMICAL CHLOR-ALKALI PROCESS .....	2
1.2.1 <i>Membrane cell technology</i> .....	4
1.3 OTHER TECHNOLOGIES FOR CHLORINE AND SODIUM HYDROXIDE PRODUCTION .....	5
1.4 THE MARKET .....	6
1.5 END USES OF CHLORINE AND SODIUM HYDROXIDE .....	7
1.6 CUF-QI .....	8
1.7 THE HISTORY OF DIMENSIONALLY STABLE ANODES (DSA <sup>®</sup> ) .....	9
1.8 PROPERTIES OF DSA <sup>®</sup> ANODES .....	11
1.9 THERMODYNAMICS [44] .....	13
1.10 KINETICS [44, 46] .....	16
1.11 MECHANISMS OF CHLORINE EVOLUTION REACTION .....	21
1.12 ACCELERATED AGEING TESTS .....	27
1.13 DEACTIVATION MECHANISMS.....	32
1.14 REFERENCES.....	34
<b>2 ELECTROCHEMICAL AND SURFACE CHARACTERIZATION TECHNIQUES</b> .....	<b>39</b>
2.1 ELECTROCHEMICAL IMPEDANCE SPECTROSCOPY .....	39
2.1.1 <i>Impedance fundamentals [1]</i> .....	39
2.1.2 <i>Impedance of electrochemical processes</i> .....	40
2.1.3 <i>Electrical equivalent circuits used to fit the impedance of DSA<sup>®</sup> anodes</i> .....	44
2.2 CYCLIC VOLTAMMETRY [26, 27] .....	49
2.3 X-RAY PHOTOELECTRON SPECTROSCOPY (XPS) [31].....	51
2.4 SCANNING ELECTRON MICROSCOPY (SEM) [42] .....	52
2.5 X-RAY ENERGY DISPERSIVE SPECTROSCOPY (EDS)[42, 43].....	54

2.6	REFERENCES .....	55
<b>3 ELECTROCHEMICAL CELL DESIGN FOR IMPEDANCE STUDIES OF CHLORINE</b>		
<b>EVOLUTION AT DSA<sup>®</sup> ANODES.....</b>		<b>59</b>
3.1	ABSTRACT .....	59
3.2	INTRODUCTION.....	60
3.3	CELL DESIGN .....	63
3.4	EXPERIMENTAL.....	65
3.4.1	<i>Reagents</i> .....	65
3.4.2	<i>Electrodes</i> .....	65
3.4.3	<i>Electrochemical measurements</i> .....	65
3.5	RESULTS.....	66
3.5.1	<i>Effect of stirring</i> .....	66
3.5.2	<i>Polarization curves</i> .....	68
3.5.3	<i>Cyclic voltammetry</i> .....	70
3.5.4	<i>Electrochemical impedance spectroscopy</i> .....	71
3.6	CONCLUSIONS .....	76
3.7	REFERENCES .....	77
<b>4 KINETIC ANALYSIS OF CHLORINE EVOLUTION ON TiO<sub>2</sub>-RuO<sub>2</sub>-IrO<sub>2</sub> DSA<sup>®</sup> ANODE BY EIS</b>		
<b>AND ANODIC POLARISATION CURVES.....</b>		<b>81</b>
4.1	ABSTRACT .....	81
4.2	INTRODUCTION.....	82
4.3	EXPERIMENTAL.....	86
4.4	CALCULATIONS .....	87
4.5	RESULTS AND DISCUSSION .....	90
4.6	CONCLUSIONS .....	100
4.7	REFERENCES .....	101
<b>5 ON THE DEACTIVATION MECHANISMS OF A TiO<sub>2</sub>-RuO<sub>2</sub>-IrO<sub>2</sub> COATED DSA<sup>®</sup> ANODE</b>		
<b>DURING CHLORINE EVOLUTION REACTION .....</b>		<b>105</b>
5.1	ABSTRACT .....	105
5.2	INTRODUCTION.....	106

5.3	EXPERIMENTAL .....	108
5.4	DISCUSSION AND RESULTS .....	110
5.5	CONCLUSIONS .....	131
5.6	REFERENCES .....	132
<b>6</b>	<b>CONCLUSIONS AND FUTURE WORK.....</b>	<b>137</b>



## List of Figures

Figure 2.1 - Typical voltamogram of a Ti/ RuO <sub>2</sub> -IrO <sub>2</sub> -TiO <sub>2</sub> anode in 0.5 mol dm <sup>-3</sup> NaCl .....	51
Figure 2.2 - XPS spectrum of ruthenium .....	52
Figure 2.3 - SEM images of DSA <sup>®</sup> anodes obtained in BSE mode with a 2000 X magnitude .	53
Figure 3.1 - The new electrochemical cell. a – Photo; b – Schematic cross section. ....	64
Figure 3.2 - Detail of the anode surface during chlorine evolution at 1.50 V vs NHE in 5 mol dm <sup>-3</sup> NaCl, pH 2, T= 60 °C; a - no stirring; b - electrolyte stirred at 500 rpm. Legend was added to highlight the stirring effect.....	67
Figure 3.3 - Effect of stirring on complex plane impedance spectra of DSA <sup>®</sup> anode at 1.50 V vs NHE in 5 mol dm <sup>-3</sup> NaCl, pH 2 at 60 °C. a - no stirring; b - electrolyte stirred at 500 rpm. Arrows identify the points preceding the bubble release. ..	68
Figure 3.4 - Polarization curves for DSA <sup>®</sup> anode in 5 mol dm <sup>-3</sup> NaCl, pH 2 at 60 °C and 80 °C; scan rate 1 mV s <sup>-1</sup> in the positive direction. ....	69
Figure 3.5 a - Cyclic voltammograms of DSA <sup>®</sup> anode as a function of scan rate in 0.5 mol dm <sup>-3</sup> NaCl, pH 2 at 20 °C. b - Plot of anodic peak current density, $j_{pa}$ , vs. scan rate. ....	70
Figure 3.6 a - Complex plane spectra for a DSA <sup>®</sup> electrode in 5 mol dm <sup>-3</sup> NaCl, pH 2 at 60 °C at different potentials. Inset shows the high frequency part of the spectra. Lines show equivalent circuit fitting. b - Bode diagrams of the spectra in Figure 3.6a. Lines show equivalent circuit fitting.....	72
Figure 3.7 - Equivalent electrical circuit used to fit the impedance spectra.....	73
Figure 4.1 - Complex plane spectra for DSA <sup>®</sup> in 1 mol dm <sup>-3</sup> NaCl, pH 2 at 20 °C at different potentials (V vs NHE). The dots are the experimental data and the lines correspond to fitting to the proposed equivalent circuit model. ....	91
Figure 4.2 - Bode diagrams for DSA <sup>®</sup> in 1 mol dm <sup>-3</sup> NaCl, pH 2 at 20 °C at the same potentials as Figure 4.1. The dots are the experimental data and the lines correspond to fitting to the proposed equivalent circuit model. a) shows log (Z) vs log (f) and b) shows phase angle vs log (f) .....	92

Figure 4.3 - Electrical equivalent circuits used to fit the impedance spectra of DSA <sup>®</sup> anodes	93
Figure 4.4 - Simulated curves $\theta$ vs $\eta$ , $C_\phi$ vs $\eta$ , $\tau$ vs $\eta$ and $C_p$ vs $\eta$ calculated from Equations 4.15, 4.16, 4.20 and 4.21, respectively. Dots represent the $C_p$ vs $\eta$ obtained from fitting the impedance spectra to EEC 4 model.....	96
Figure 4.5 - Anodic polarisation curve obtained on DSA <sup>®</sup> anode in 1 mol·dm <sup>-3</sup> NaCl at 20 °C. Symbols represent the experimental values and the continuous line the kinetic model.....	97
Figure 4.6 – Charge transfer resistance obtained from the kinetic model vs charge transfer resistance obtained from the EEC model.....	99
Figure 4.7 – Resistance associated with adsorption estimated from the kinetic model vs low frequency resistance obtained from the EEC model.....	99
Figure 5.1 – Current density history during the accelerated ageing test of DSA <sup>®</sup> anode in 5 mol dm <sup>-3</sup> NaCl .....	111
Figure 5.2 -Cyclic voltammograms obtained at different ageing times of DSA <sup>®</sup> anode in 0.5 mol dm <sup>-3</sup> NaCl. ....	112
Figure 5.3 – Anodic voltammetric charge of the DSA <sup>®</sup> anode over the time, $\nu = 50 \text{ mV s}^{-1}$	113
Figure 5.4 - Complex plane spectra for DSA <sup>®</sup> anode in 5 mol dm <sup>-3</sup> NaCl, pH 2 at 20 °C at 1.4 V vs NHE, recorded at different times of the ageing test. The dots are the experimental data and the lines correspond to fitting to the proposed electrical equivalent circuit model.....	114
Figure 5.5 - EEC used to fit the impedance of the DSA <sup>®</sup> recorded at 1.4 V vs NHE at different stages of the ageing test. a – EEC used to fit the spectra recorded over the first 3000 h of the test; b – EEC used to fit the impedance spectra recorded from 3586 h onwards .....	115
Figure 5.6 - Phase angle obtained from spectra in Figure 5.4.....	116
Figure 5.7 - Evolution of the magnitude of the high frequency CPE with the ageing time of DSA <sup>®</sup> anode in 5 mol dm <sup>-3</sup> NaCl.....	117
Figure 5.8 – Evolution of the high frequency resistance with the time of ageing test of DSA <sup>®</sup> anode in 5 mol dm <sup>-3</sup> NaCl solution .....	119

Figure 5.9 – Evolution of the magnitude of the CPE used to describe the pseudocapacitance of the DSA <sup>®</sup> anode with the ageing time in 5 mol dm <sup>-3</sup> NaCl.....	120
Figure 5.10 - Evolution of the low frequency resistance of the DSA <sup>®</sup> anode with the ageing time in 5 mol dm <sup>-3</sup> NaCl.....	120
Figure 5.11 - EEC used to fit the impedance of the DSA <sup>®</sup> recorded at 0.5 V vs NHE at different stages of the ageing test. a – EEC used to fit the spectra recorded over the first 3000 h of the test; b – EEC used to fit the impedance spectra recorded from 3586 h onwards .....	122
Figure 5.12 - Complex plane spectra for DSA <sup>®</sup> anode in 5 mol dm <sup>-3</sup> NaCl, pH 2 at 20 °C at 0.5 V vs NHE, recorded at different times during the ageing test. The dots are the experimental data and the lines correspond to fitting to the proposed electrical equivalent circuit model. ....	123
Figure 5.13 – Detail of high frequency region of the spectra in Figure 5.12.....	124
Figure 5.14 – SEM images of DSA <sup>®</sup> anode taken at different times during the ageing test.	127
Figure 5.15 – X-Ray mapping image obtained by EDS. a – new anode; b – used anode (4600 h) .....	128



## List of Tables

Table 1.1 - Main equations of the chlor-alkali membrane cell process .....	4
Table 1.2 – Normal operation conditions in the anodic compartment of a chlor-alkali membrane cell.....	28
Table 1.3 – Literature review of the operation conditions of accelerated ageing test of DSA anodes .....	30
Table 1.3 – Literature review of the operation conditions of accelerated ageing test of DSA anodes (continued) .....	31
Table 2.1 – Electrical equivalent circuits to fit the impedance of DSA® at potentials for OER or ClER .....	45
Table 2.2 - Electrical equivalent circuits to fit the impedance of DSA® in the capacitive region of the electrode.....	48
Table 3.1 - Fitting parameters and standard deviation (2 repeat spectra) obtained from the electrochemical impedance spectra at different potentials, data from Figure 3.6.....	74
Table 4.1 - Parameters of EEC 4 obtained fitting the impedance spectra at different potentials.....	94
Table 4.2 – Values of the rate constants and symmetry factors calculated for the individual steps for the ClER on a DSA® .....	98
Table 5.1 - Parameters of the EEC used to fit the impedance of the spectra obtained at different times.....	125
Table 5.2 – Relative atomic composition of the DSA® anode surface composition obtained by EDS.....	129
Table 5.3 - Relative atomic composition of the DSA® anode surface composition obtained by XPS. ....	130



## Notation

$A$	Geometric area	$\text{cm}^2$
$a_i$	Activity of the species $i$	$\text{mV decade}^{-1}$
$b$	Tafel slope	–
$C_{dl}$	Double layer capacitance	$\text{mF cm}^{-2}$
$C$	Capacitance	$\text{mF cm}^{-2}$
$C_f$	Film capacitance	$\text{mF cm}^{-2}$
$C_p$	Pseudocapacitance	$\text{mF cm}^{-2}$
$C_\phi$	Steady-state pseudocapacitance	$\text{mF cm}^{-2}$
$D$	Diffusion coefficient of species	$\text{m}^2 \text{s}^{-1}$
$E$	Electrode potential	V
$E_A$	Activation energy	$\text{J mol}^{-1}$
$E_{cel}$	Cell potential	V
$E_{eq}$	Equilibrium potential	V
$E^\ominus$	Standard electrode potential	V
$E_T^{\ominus'}$	Formal potential	V
$f$	Frequency	Hz
$\Delta G$	Gibbs free energy	$\text{J mol}^{-1}$
$\Delta G^\ddagger$	Standard free energy of activation	$\text{J mol}^{-1}$
$\Delta H^\ddagger$	Standard enthalpy of activation	$\text{J mol}^{-1}$
$i$	Electric current	A
$i_C$	Capacitive current	A
$i_F$	Faradaic current	A
$i_t$	Total current	A
$i_0$	exchange current	A
$j$	Current density	$\text{A cm}^{-2}$
$j$	Imaginary number	–
$j_0$	Exchange current density	$\text{A cm}^{-2}$

$k$	Rate constant	$\text{mol cm}^{-2} \text{s}^{-1}$
$k_a$	Anodic rate constant	$\text{mol cm}^{-2} \text{s}^{-1}$
$k_c$	Cathodic rate constant	$\text{mol cm}^{-2} \text{s}^{-1}$
$k_0$	Standard rate constant	$\text{mol cm}^{-2} \text{s}^{-1}$
$K$	Equilibrium constant	–
$L$	Inductance	H
Me	Metal	–
$q$	Electric charge	–
$n$	Number of electrons transferred	–
$n$	Exponent of CPE	–
$O_i$	Oxidized species	–
$p$	Pressure	bar
$r$	Reaction rate	$\text{mol cm}^{-2} \text{s}^{-1}$
$r_0$	Charge balance	$\text{mol cm}^{-2} \text{s}^{-1}$
$r_1$	Mass balance of adsorbed species	$\text{mol cm}^{-2} \text{s}^{-1}$
$R_{ct}$	Charge transfer resistance	$\Omega \text{ cm}^2$
$R_f$	Film resistance	$\Omega \text{ cm}^2$
$R_i$	Reduced species	–
$R_p$	Adsorption resistance	$\Omega \text{ cm}^2$
$R_\Omega$	Ohmic resistance	$\Omega \text{ cm}^2$
S	Active site	–
$\Delta S^\ddagger$	Standard entropy of activation	$\text{J mol}^{-1} \text{K}^{-1}$
$T$	Absolute temperature	K
$t$	Time	s
$Y_0$	CPE magnitude	$\text{F cm}^{-2} \text{s}^{n-1}$
$Z$	Impedance	$\Omega \text{ cm}^2$
$Z'$	Real component of impedance	$\Omega \text{ cm}^2$
$Z''$	Imaginary component of impedance	$\Omega \text{ cm}^2$
$Z_0$	Magnitude of impedance	$\Omega \text{ cm}^2$

$Z_{CPE}$	Capacitance of the CPE	$\Omega \text{ cm}^2$
$Z_w$	Impedance of the Warburg element	$\Omega \text{ cm}^2$
$\alpha$	Charge transfer coefficient	–
$\beta$	Symmetry factor of the Volmer step	–
$\gamma$	Symmetry factor of the Heyrovsky step	–
$\gamma_i$	Activity coefficient of the species $i$	–
$\eta$	Overpotential	V
$\theta$	Fraction of occupied active sites	–
$\nu$	scan rate	$\text{mV s}^{-1}$
$\nu_i$	Stoichiometric number	–
$\sigma_D$	Warburg coefficient	$\Omega \text{ s}^{-1/2}$
$\tau$	Relaxation time	s
$\phi$	Phase shift	°
$\omega$	Angular frequency	$\text{rad s}^{-1}$

## Abbreviations

BSE	Backscattered electrons
CIER	Chlorine evolution reaction
CPE	Constant phase element
CV	Cyclic voltammetry
DSA®	Dimensionally stable anode
EDS	X-Ray energy dispersive spectroscopy
EEC	Electrical equivalent circuit
EIS	Electrochemical impedance spectroscopy
ESCA	Spectroscopy for Chemical Analysis
MDI	Methylene diphenyl diisocyanate
NHE	Normal Hydrogen Electrode

OER	Oxygen Evolution reaction
PTFE	Polytetrafluoroethylene
PVC	Polyvinyl chloride
SCE	Saturated calomel electrode
SE	Secondary Electrons
SEM	Scanning Electron Microscopy
VHT	Volmer-Heyrovsky-Tafel mechanism
XPS	X-Ray photoelectron spectroscopy

## Fundamental physical constants

$F$	Faraday constant	$9.6485 \times 10^4 \text{ C mol}^{-1}$
$R$	Ideal gas constant	$8.314462 \text{ J K}^{-1} \text{ mol}^{-1}$

## Subscript

0	Reference condition
a	Anodic
c	Cathodic
*	At electrode surface
$\infty$	At the bulk
pa	Anodic peak
ads	adsorbed species

# 1 Introduction

## 1.1 The history of chlorine and sodium hydroxide

The chlor-alkali is one of the most important worldwide commodity industries which underpins about 60 % of the chemical industry turnover [1]. In fact, the broad range of applications of the chlorine and sodium hydroxide produced put them among the top 10-chemicals produced in the world [2].

The production of chlorine was firstly reported by C. W. Scheele in 1774 [3]. Chlorine was the greenish yellow gas product of the reaction of hydrochloric acid with manganese oxide; this reaction produces manganese chloride as by-product. C. W. Scheele found the bleaching effect of chlorine on vegetable matter, although the large scale use of chlorine application, as potassium hypochlorite, for bleaching application is assigned to McPherson in 1789 [2]. Nine years later, a patent to produce calcium hypochlorite solution was issued [2]. Despite its previous applications, only in 1808 H. Davy identified the chlorine as a pure element. In 1823 the first utilization of chlorine as hospital disinfectant is reported [2] though, at that time, the main use of chlorine was for bleaching the paper pulp.

In 1866, the yield of the technology for producing chlorine was improved when Weldon introduced the recirculation of manganese chloride. In 1868, Deacon developed an alternative chlorine production process involving the oxidation of hydrogen chloride with  $\text{CuCl}_2$  catalyst [1]. This route allowed achieving yields up to 65 % which were almost double of those obtained by Weldon process (35 %) [3]. The use of chlorine compounds to water and sewage treatments were addressed already in 1890; by 1912, the use of chlorine for these applications became widespread. As a consequence, the incidence of waterborne diseases such as typhoid dramatically reduced [2]. Many other chlorine uses were boosted during the first and the second World wars. Due to its low price and reactivity, the range of applications of chlorine has widespread for critical fields, from pharmaceuticals to fertilizers and polymers industries [2].

The first evidence of sodium hydroxide utilization dates back to the 3<sup>rd</sup> century B.C., which made this compound one of the first chemicals synthesized. However, the first records of caustic solution production came from Egypt and India in the early years A.D. [4]. At the beginning of the 20<sup>th</sup> century, caustic soda was produced by reacting lime with sodium carbonate - the so-called lime stone process. Currently, this process accounts for 1-2 % of the worldwide caustic soda production [5]. During World Wars, the larger chlorine demand led to the co-production of chlorine and caustic soda by electrochemical routes and, until now, this has remained as the preferable way for manufacturing both inorganic compounds [2].

## **1.2 The electrochemical chlor-alkali process**

The first electrochemical process for chlorine and sodium hydroxide production was developed by Cruickshank in 1800 [2]. However, the first patent for the electrochemical production of chlorine was filled only 51 years later by Charles Watt [3, 6], who described the diaphragm cell process [3]. This technology became commercial in Germany in 1888 by the Griesheim Company [2]. The anode was made of magnetite or graphite and the cathode of iron sheets. The diaphragm was a porous barrier made of cement [2]. In 1890, in the United States, Le Sueur introduced a percolating diaphragm that permitted achieving higher efficiencies [3]. However, the electrochemical route to produce chlorine began to have industrial relevance only in 1892 thanks to Siemens, Acheson and Castner, who developed the mercury cell [3]. While Siemens developed reliable current generators, Acheson and Castner, introduced synthetic graphite anodes in the mercury cells [3]. In 1910, carbon steel cathodes were introduced in the diaphragm cells. In the 1920s, Billiter introduced asbestos wool as the main component of the diaphragm and Kenneth Stewart from Hooker Chemical developed a vacuum process to deposit asbestos fibers onto the cathode [1, 2]. This development is considered one of the most important milestones of the chlor-alkali industry [2]. This diaphragm remained in use up to the 1970s when polytetrafluoroethylene (PTFE) was added to asbestos diaphragm composition [1, 2].

During 1950 – 1960s several firms strived to develop electrochemical membranes cells for the chlor-alkali process that, unlike the diaphragm, are ion-selective barriers. The progress achieved by the joint-venture Diamond-Ionics showed the viability of the membrane technology, although limitations such as the high cell voltage and the short membrane life suspended the research on this technology [2].

In the 1960s, the awareness of the toxicological effects of asbestos and mercury used in the chlor-alkali cells led to a further impulse in the search for alternative technologies for chlor-alkali production. Over this decade, two accomplishments revolutionized the chlor-alkali industry: 1) the launching of high resistance perfluorinated ion-exchange Nafion® membranes by Dupont; and 2) the development of coated metal anodes [2, 6]. The introduction of metal anodes, commercially available under DSA® designation, by Henry Beer, is even today considered one of the greatest progresses not only of the chlor-alkali industry, but also of the history of electrochemistry [2, 7]. Boosted by these two achievements, a pilot plant incorporating cell membranes was installed in Ohio, in 1972. At the same time, the graphite electrodes that were used in diaphragm and mercury cells started to be replaced by DSA®. In 1975, in Japan, the first industrial scale plant equipped with membrane cell technology was commissioned [1, 2].

In the early 1980s, carbon steel cathodes were replaced by stainless steel and nickel cathodes. Although steel is more active for the hydrogen evolution reaction, nickel presents greater resistance to sodium hydroxide corrosion than iron [2]. In order to increase the activity of the cathode towards the hydrogen evolution reaction, nickel cathodes have been coated doped with different metals (e. g. Ir, Ru, Fe, W, Co, Al, Mo) and have their surface area increased by thermal decomposition or plasma spraying preparation techniques. Raney nickel, one of the most active coatings, consists of aluminium-nickel or zinc-nickel Raney alloys which exhibit a high porous structure. The high surface area is obtained by leaching aluminium and zinc from the cathode with high concentrated sodium hydroxide [2]. This type of coating allows reducing the overpotential for hydrogen evolution from by ca. 200 mV [2].

Up to the end of the first decade of the 21<sup>st</sup> century, membrane cell technology has been the state of art of the chlor-alkali industry and currently all new plants were assembled with this technology [2, 3]. In 2012, membrane cell technology accounted for around 63 % of the worldwide chlorine production capacity. In the same year, the share of the diaphragm was 26 % and the mercury cell technology represented 6-7 % of the global capacity of chlorine production [8]. In Europe the phase-out of mercury cells should be completed by 2017 [9].

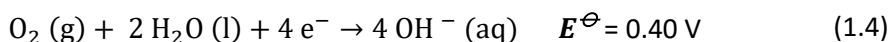
### 1.2.1 Membrane cell technology

The membrane cell consists of three main components - the DSA<sup>®</sup> anode, a nickel cathode and an ion-selective membrane. This membrane divides the electrochemical cell in two compartments. The anodic compartment is fed with high concentrated sodium chloride solution (brine ca. 26 wt. %) from which the chloride ions contacting to the anode are oxidized to chlorine. The sodium ions are transported through the membrane towards the cathode compartment, which is fed with a sodium hydroxide solution (ca. 30 wt. %). In the cathode compartment, water is reduced to hydrogen and hydroxyl ions. The hydroxyl ions combine with the sodium ions from the anodic reaction to produce sodium hydroxide leading to an outlet stream with a higher sodium hydroxide concentration (ca. from 30 to 32 wt. %). On the other hand, the solution exiting the anode side is a diluted sodium chloride solution (ca. 20 wt. %) [1, 2]. Equations 1.1 and 1.2 describe the half-reactions on each electrode and Equation 1.3 is the global equation. The standard reduction potential of each half-cell and the thermodynamic potential of the full cell are given in Table 1.1.

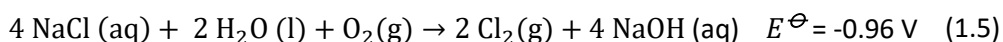
Table 1.1- Main equations of the chlor-alkali membrane cell process

Equations	$E^\ominus / \text{V vs NHE}$	
$\text{Cl}_2(\text{g}) + 2 \text{e}^- \rightarrow 2 \text{Cl}^- (\text{aq})$	1.36	(1.1)
$2 \text{H}_2\text{O} (\text{l}) + 2 \text{e}^- \rightarrow \text{H}_2(\text{g}) + 2 \text{OH}^- (\text{aq})$	- 0.83	(1.2)
$2 \text{NaCl} (\text{aq}) + 2 \text{H}_2\text{O} (\text{l}) \rightarrow \text{Cl}_2(\text{g}) + \text{H}_2(\text{g}) + 2 \text{NaOH} (\text{aq})$	- 2.19	(1.3)

Despite the improvements carried out during the last years by the chlor-alkali producers and licensors, no significant progress has been accomplished. During the 90's and the first decade of the 21<sup>st</sup> century, the most relevant improvements are related to electrolyser design. There is, however, potential for disruptive new technology in the chlor-alkali industry - the oxygen depolarized cathodes [10]. The application of this type of electrode in the chlor-alkali cells has been addressed by different companies and was the issue of two patents filled in 2010 [11, 12]. Three years later, lab [13] and pilot cells [14] equipped with this technology showed a reduction on the energy demand of about 30 % to 40 % compared to the cells using conventional cathodes. In opposition to the previous chlor-alkali cell technologies, in the oxygen depolarized cathodes cells, a different reaction occurs on the cathode:



and, since the anodic reaction remains unchanged (Equation 1.1), the equation of the full cell is:



### **1.3 Other Technologies for chlorine and sodium hydroxide production**

Nowadays, chlorine and caustic soda are produced almost exclusively by electrolytic processes. More than 95 % of the chlorine and around 98-99 % of caustic soda produced worldwide are co-produced by electrochemical technologies [2]. Since the demand of both chemicals does not follow the fixed stoichiometry of the chlor-alkali process, alternative processes to produce these chemicals have been pursued. Regarding chlorine production, the alternative processes are the electrolysis of hydrochloric acid, the electrolysis of alkali metal chlorides (LiCl) and alkaline earth metal chlorides (MgCl<sub>2</sub>). In 2010, these techniques accounted for less than 3% of the total production capacity in Europe [8]; an other process

with some relevance, which is currently used at industrial level, is the catalytic oxidation of hydrogen chloride by oxygen[3].

Concerning caustic soda, currently, limestone process accounts to 1-2% of the worldwide caustic soda production. This pathway is mostly implemented in USA where it is profitable [6].

## 1.4 The market

In 1970, the world chlorine capacity was about 20 Mt/year and it was concentrated in USA (48 %), western Europe (25%), Japan (12 %) and eastern Europe (12 %) [2]. From 1970 to 2008, the total installed capacity has increased about 2.8 % per year, achieving 62.8 Mt in 2008 [3]. However, the growth of chlorine capacity has been geographically asymmetric and has been displaced to east. In 2008, China was the largest chlorine producer representing 26 % of the global capacity, followed by USA (23 %) and Europe (20 %) [3]. While in Europe, USA and Japan the capacity has kept almost constant, China has boost chlorine production capacity in 50 % from 2004 to 2008. In 2012 the total capacity of chlorine production attained 76.8 Mt/ year with China representing 41 % of share, followed by North America with 18 % and Europe with 16 % of the worldwide production of chlorine [8].

Around 98-99% of the sodium hydroxide is co-produced electrochemically with chlorine, so its availability is strongly dependent on the chlorine production [6, 8]. From Equation 1.3, a sodium hydroxide-chlorine mass ratio of 1 : 0.88 is expected. Thus, the worldwide caustic soda capacity would be around 82.9 Mt in 2012. However, the inefficiencies of the chlor-alkali process and the existence of alternative route to produce chlorine (around 5 %) result in an overall caustic soda production capacity to around 80 Mt.

Due to the co-production of chlorine and sodium hydroxide, the price of each of the two commodities depends on the demand of both chemicals [6]. Hence, to respond to the rising demand for one of the products, the other product will be in excess and its price will fall [8]. This interdependence of chlorine and caustic soda results in extreme

fluctuation of their prices, which is critical to the profitability of the chlor-alkali industry. [3, 6, 8]

Despite the demand for NaOH have had greater importance than chlorine in the past, from World War II the chlorine demand overcame the caustic soda demand. The major contributor for the increase of chlorine demand has been the PVC industry, which is the main consumer of this commodity. Since it is forecasted that PVC and chlorine demand will keep increasing more than the caustic soda demand, search for alternative synthesis of chlorine his being pursued [2].

## **1.5 End uses of chlorine and sodium hydroxide**

Chlorine is a component present in end used products like PVC, hydrochloric acid or sodium hypochlorite, although it also has an important role as intermediate to the production of chlorine-free end products such as polyurethanes. Beyond the critical use of chlorine for water treatment, chlorine plays an important role in pharmaceutical industry, where chlorine is used along the production chain of 93 % of the total of products available on the market. In addition, chlorine is effectively present in 25 % of the final compounds [15]. Chlorine is particularly important to the crop protection industry, where 96 % of the chemicals are produced using chlorine [3]. These numbers reflects the fundamental role of chlorine in our lives, although it is just a snapshot of the application fields of the chlorine. A schematic and detailed end use and intermediate applications of chlorine is organised in compiled in the chlorine tree [9].

Concerning sodium hydroxide, some important applications are the industrial water treatment, the soaps and detergents industry and food industries. However, the main uses of caustic soda are the synthesis of organic and inorganic compounds and the pulp and paper industry [2, 16]. The sodium chlorine tree, which shows the manifold uses of sodium hydroxide, is available in [9].

## 1.6 CUF-QI

CUF-QI is a chemical company located in Estarreja, being a key player in the Estarreja petrochemical site. Operating in both organic and inorganic fields, CUF-QI produces aniline used needed for the production of the methylene diphenyl diisocyanate (MDI), chlorine and sodium hydroxide. Other important products are sodium hypochlorite, hydrogen, hydrochloric acid mononitrobenzene, nitric acid, sulphanilic acid, cyclohexylamine and cyclohexanol.

CUF-QI is the only chlorine producer in Portugal and the third in the Iberian Peninsula with an installed capacity of 116,000 tonnes per year [9]. Two different technologies are used: chlor-alkali electrolysis by the membrane process (72,000 tonnes per year) and hydrochloric acid electrolysis using the diaphragm process technology (44,000 per year) [9]. CUF-QI has been a leading-edge company and one of the first worldwide chlor-alkali companies replacing, in 2002, all the mercury cells by the most environmental friendly membrane technology.

Chlor-alkali electrolysis is one of the most electricity intensive processes among all the industries so energy consumption is one of the critical issues and one the main research vectors in this industry.

Despite the most recent technology allows operating the new cells near to the thermodynamic consumption, the cell performance declines with time leading to an increase on energy consumption due to the loss of activity of the electrodes. Recoating or replacing electrodes, mainly anodes, is expensive since noble metals are needed. The evaluation tools used to follow the cell performance do not provide information about the state of each electrode, making the maintenance decision to happen at a safe distance from the optimal time.

The aim of this thesis is to develop a toolbox of electrochemical techniques to allow monitoring the performance of each electrode, particularly the DSA® anode. Furthermore, the techniques developed will be useful to determine the root causes of anode deactivation and to provide relevant information to decide the optimal instant to recoat the anodes.

## 1.7 The history of dimensionally stable anodes (DSA®)

The origin and success of the dimensionally stable anodes (DSA®) cannot be separated from the history of the chlor-alkali industry. Indeed, the great promoter of the origin of DSA® anodes was the chlor-alkali industry. During the first half of the 20<sup>th</sup> century, chlor-alkali cells were equipped with graphite anodes [2]. Despite having been a well-established technology for the anodic evolution of chlorine, the disadvantages related to the consumption of graphite were evident [6]. The oxidation of graphite, not only caused the contamination of the chlorine, but also reduced the service life of the anodes to a maximum of 24 months. Besides, the consumption of graphite increases the gap between electrodes leading to an increase in energy consumption over the electrode lifespan. Even with such limitations, the chlorine industry seemed to be resigned to use graphite anodes [17]. Indeed, apart the experiments carried out by Beer and Stevens, no other documents addressing the study of electrodes for the anodic chlorine are known. In 1913, Stevens [18] patented a tungsten electrode plated with platinum which could be applied to the chlorine evolution. This electrode resembles the DSA® anodes since they were made of a valve metal and a metal from the platinum group. This combination of metals suggests the synergetic effect of the stability provided by the valve metal and the activity of the platinum. The next reference to similar anodes is a patent filled by Cotton and co-workers in 1961 [19]. The inventors patented an anode made of platinum supported on a titanium substrate. However, the high wear rate of platinum and the consequent short service life of this anode made this combination of materials unfeasible to replace the graphite [3]. Four years later, in 1965, Beer filled a patent that would revolutionize the chlor-alkali industry [20]. This patent marks the official invention of dimensionally stable anodes (DSA®), although in an article published in 1980, Beer confirmed that his research on anodic materials for chlorine evolution had started long before the issuing of the patent - in the 1930s [17]. Despite using elements of the same groups of the periodic table that had been used before, instead of pure elements, Beer used oxides of those elements. The patent filled by Beer refers that the electrode consists of a metallic substrate (titanium, tantalum, zirconium, niobium) and a coating made of at least two oxides. One of the oxides

contains one metal from platinum group (platinum, iridium, rhodium, palladium, ruthenium or osmium) and the second is an oxide of one of the following metals: manganese, lead, chromium, cobalt, iron, titanium, tantalum, zirconium and silicon. Beer patented not only the composition, but also the thermal decomposition method for depositing the coatings electrodes. This method consists in preparing a solution by dissolving the metal precursors in an organic solvent. The solution is then applied to the substrate followed by a drying annealing treatment [20-22]. This still is the method used for preparing industrial DSA<sup>®</sup> anodes [2]. After this patent, other patents addressing the same topic were filled by Beer (GB1195871 [23], US3265526 [24], US3632498 [25], US3711385 [26] ), although most of them claim only small improvements in the preparation method of the electrodes or minor changes in their composition. In a previous patent, US 3214110 [24], Beer claimed titanium as the preferred metal for the substrate since titanium forms a spontaneous protective titanium oxide layer that prevents the substrate from electrolyte attack and do not exhibit significant resistance to the current flow. These features made titanium the most suitable material to be used as substrate for anodes in chlor-alkali cells. Regarding the choice of the active metal, the selection of ruthenium, in the oxide form, was first based on its price compared with platinum or iridium. Attempts to improve the stability of the coating led to the addition of titanium oxide as a stabilizer of the metal oxide. Therefore, the final composition for the first commercial anodes was a titanium substrate coated with a binary ruthenium-titanium oxide film. Nowadays the composition of DSA<sup>®</sup> for chlorine evolution has remained almost unchanged [2]. Only the addition of iridium oxide to the original composition, was a relevant milestone [6]. The addition of iridium oxide was shown to prevent the loss of ruthenium, leading to the extension of the service life of the anodes from 2-3 years [6] to 8 years [7]. The stabilization of ruthenium oxide by iridium oxide was firstly reported by Kötzt and Stucki in 1986 [27].

## 1.8 Properties of DSA® anodes

Although DSA® anodes were introduced more than 50 years ago, this type of anodes remains the state of art as anodes for the chlor-alkali industry. Since the beginning of the 21<sup>st</sup> century, all new chlor-alkali plants in the world, regardless of the cell technology, have been equipped with DSA® anodes [6]. Besides, the use of this type of anodes has spread to other fields like electrogalvanization or cathodic protection [28]. In fact, the high activity and stability ensured by DSA® anodes led to energy savings that made these electrodes unrivalled.

The development of DSA® anodes was mostly empiric rather than by fundamental research. It was only after the successful industrial implementation, in 1968, that scientific interest in the properties of DSA® anodes arose [7]. The first article addressing the fundamental properties of DSA® anodes was published in 1971 [29]. Since then, a number of authors have attempted to establish correlations between the physicochemical properties of the electrode and its electrochemical behaviour [30-36].

In their work, Trasatti and Buzzanca [29] performed cyclic voltammetry experiments to study a thermally decomposed RuO<sub>2</sub> film similar to the oxide coating used in DSA® anodes. In this work, the authors found that thermally decomposed RuO<sub>2</sub> films exhibited a profile similar to an electrical capacitor rather than the typical redox voltammogram obtained for a single RuO<sub>2</sub> crystal obtained by a vapor-phase process. Trasatti and Buzzanca also evaluated the dependence of the voltammetric charge on the coating thickness, annealing temperature and O<sub>2</sub>/N<sub>2</sub> ratio. Based on the voltammetric charge increase with the coating thickness increase, Trasatti and Buzzanca concluded that the voltammetric charge is caused by electrochemical processes occurring not only at the electrode surface, but also in the electrode bulk. The contribution of the internal surface is so relevant that roughness factors (real area/geometric area) around 200-400 are typically reported [2, 37]. However, according to Zheng and co-authors [38], the effect of the surface area (internal or external) should not be overestimated and the effect of water molecules in the coating should be taken into account. These authors showed that the

specific capacitance of hydrous RuO<sub>2</sub> electrodes is larger than that determined for anhydrous RuO<sub>2</sub>, though the latter exhibited larger BET areas.

Concerning the annealing temperature and oxygen fraction, Trasatti and Buzzanca [29] found that the voltammetric charge decreases with increasing temperature and O<sub>2</sub>/N<sub>2</sub> ratio. The lower annealing temperature and O<sub>2</sub>/N<sub>2</sub> ratio lead to a lower degree of decomposition of the RuCl<sub>3</sub>·xH<sub>2</sub>O resulting in the presence of H<sub>2</sub>O and Cl<sup>-</sup> in the film that leads to a non-stoichiometric of the RuO<sub>2</sub> film with O/Ru < 2 [29]. The non-stoichiometry in the oxide suggests the presence of ruthenium in the form Ru<sup>3+</sup>. Between 0.3 V and 1.35 V, this lack of Ru atoms in the lattice will promote the reduction/oxidation of Ru<sup>4+</sup> to Ru<sup>3+</sup> resembling the charging and discharging processes of a capacitor.

According to Roginskaya and co-authors [39] and Lassali and co-workers [40], the presence of water molecules in the lattice promotes the diffusion of protons through the coating allowing the participation of the inner iridium sites in the solid state redox reactions of IrO<sub>2</sub> based coatings. Also for RuO<sub>2</sub> based coatings, Lokhande and co-workers [41] mentioned the role of the diffusion of protons over the hydrous ruthenium compounds to explain the participation of the active sites in the bulk of the coating. The penetration or ejection of protons to/from electroactive sites is a reversible responsible for the pseudocapacitive behavior of the electrode. This process is described by Equation 1.6 [29, 42, 43].



where Me is the metal, in this case, ruthenium or iridium.

According to Lokhande and co-authors, the electron supply shown in Equation 1.6 is conducted through a three-step process:

- i) Electron hopping within RuO<sub>2</sub>·xH<sub>2</sub>O particles;
- ii) Electron hopping between particles;
- iii) Hopping between electrode materials and current collectors.

Since the iridium and ruthenium exhibit different oxidation/reduction couples, the capacitor-shape voltammograms obtained for DSA<sup>®</sup> are likely to be related to the overlapping of these oxidation-reduction reactions [37].

Despite representing a significant part of the total charge of the electrode, pseudocapacitance is not the only source of voltammetric charge. The double layer capacitance has a contribution that Conway [37] mentions to account for up to 10 % of the total charge .

## 1.9 Thermodynamics [44]

Thermodynamics provides information about the spontaneity of reactions. The parameter that provides this information is the Gibbs free energy,  $\Delta G$ . For electrochemical systems, at constant pressure and temperature, it is calculated by Equation 1.7, where  $n$  is the number of electrons transferred between each species,  $F$  is Faraday constant and  $E_{cel}$  is the cell potential [44].

$$\Delta G = -nFE_{cel} \quad (1.7)$$

If  $\Delta G < 0$ , reactions are spontaneous and the cell is a galvanic cell. On the contrary, if  $\Delta G > 0$ , reactions require energy from the exterior and the cell is an electrolytic cell. This is the case of the chlor-alkali cell. The value of  $\Delta G$  represents the maximum energy that the cell can supply (galvanic cell) or the minimum energy that the system requires (electrolytic cell) [44, 45].

The cell potential,  $E_{cel}$ , results from the contribution of the potential of the half-cell reaction occurring in each electrode. By IUPAC convention, the cell potential is obtained by Equation 1.8:

$$E_{cel} = E_c - E_a \quad (1.8)$$

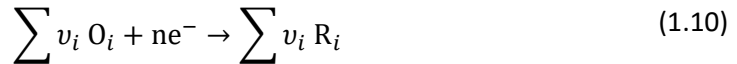
where  $E_c$  and  $E_a$  are the reduction potentials of the cathodic and anodic reactions, respectively.

The electrode potential,  $E$ , is a property of each half-cell reaction and measures the ability of a species to be reduced or oxidized. The electrode potential is not an absolute value, but it is measured against a reference. The most used reference is the potential of the hydrogen formation reaction, Equation 1.9, on a platinized platinum foil. The potential of this reaction is considered 0 V at 25 °C, with the species at unit activity or pressure ( $p_{\text{H}_2}=1$  bar,  $a_{\text{H}^+}=1.0$ ).



When the activity of the species is unity, the reduction potential is stated as the standard electrode potential,  $E^\ominus$ . The data for standard electrode potentials at 25 °C are easily found in the literature [44, 46].

The value of the cell potential must be modified to take into the temperature and the activities of the species involved in the reaction using the Nernst equation. Considering a generic half-reaction (where O is the oxidized species and R the reduced species),



the corresponding Nernst Equation is given by Equation 1.11 [44].

$$E = E_T^\ominus - \frac{RT}{nF} \sum v_i \ln a_i \quad (1.11)$$

or alternatively

$$E = E_T^\ominus + \frac{RT}{nF} \ln \frac{\prod a_{\text{O}_i}^{v_i}}{\prod a_{\text{R}_i}^{v_i}} \quad (1.12)$$

where  $R$  is the ideal gas constant,  $T$  is the absolute temperature in K,  $n$  is the stoichiometric number of electrons transferred for each species,  $F$  is the Faraday constant and  $a_i$  is the activity of each species involved in the reaction.  $v_i$  is positive for products and negative for reactants.

Although the Nernst equation includes a temperature term, it does not take the temperature effect on the half-cell potential fully into account [2, 47]. Indeed, also the standard electrode potential must be adjusted to the effective operation temperature. At a temperature,  $T$ , the half-cell standard potential,  $E_T^\ominus$ , can be calculated by Equation 1.13:

$$E_T^\ominus = E_{T_0}^\ominus + \left( \frac{dE^\ominus}{dT} \right)_{T_0} (T - T_0) + \frac{1}{2} \left( \frac{d^2E^\ominus}{dT^2} \right)_{T_0} (T - T_0)^2 \quad (1.13)$$

in which  $E_{T_0}^\ominus$  is the standard electrode potential available in literature at temperature  $T_0$ , usually 25 °C and the derivative terms are specific of each redox couple.

For practical convenience, activities are replaced by concentrations or partial pressures. With exception to ideal systems, i.e. diluted solution or ideal gases, this change implies the substitution of the standard electrode potential by the formal potential,  $E_T^{\ominus'}$ . While standard electrode potentials are easily found in the literature, formal potentials need to be calculated. Equation 1.14 relates both quantities [44].

$$E_T^{\ominus'} = E_T^\ominus + \frac{RT}{nF} \ln \frac{\prod \gamma_{iO_i}}{\prod \gamma_{iR_i}} \quad (1.14)$$

where  $\gamma_i$  is the activity coefficient of the specie  $i$ . For dilute solutions or ideal gases, the activity coefficients are around unity and the standard potential and formal potential have the same value.

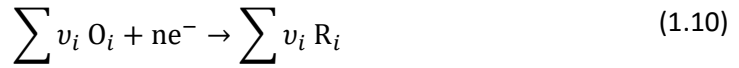
Thus, Equation 1.12 can be transformed into Equation 1.15 [44]:

$$E = E_T^{\ominus'} + \frac{RT}{nF} \ln \frac{\prod [O_i]}{\prod [R_i]} \quad (1.15)$$

where  $[i]$  is the concentration or the partial pressure of species  $i$ .

## 1.10 Kinetics [44, 46]

From Equation 1.10,



the reaction rate,  $r$ , is calculated from the difference of forward and backward reactions as shown in Equation 1.16:

$$r = k_c[O]_* - k_a[R]_* \quad (1.16)$$

where  $k_c$  and  $k_a$  being the cathodic and anodic rate constants.

The subscript asterisk refers to the concentration of species at the electrode surface.

Unlike homogeneous reactions, which depend on the reactor volume, since electrochemical reactions take place at the electrode surface and not in the bulk, the reaction rate depends on the area of the electrode instead. Thus, the dimensions of reaction rate considered throughout this work are normalized by the electrode area as given by Equation 1.17:

$$r = \frac{1}{A} \frac{dN}{dt} \quad (1.17)$$

In electrochemical systems, as well as reaction rate, it is usual to consider the current passing through the electrode. Equation 1.18 relates both quantities.

$$i = nFAr \quad (1.18)$$

and

$$i = i_c - i_a \quad (1.19)$$

where  $i_c$  is the cathodic current and  $i_a$  the anodic current.

From Equations 1.16, 1.18 and 1.19, the current can be computed:

$$i = nFAk_c[O]_* - nFAk_a[R]_* \quad (1.20)$$

The values of rate constants,  $k$ , are given by the Arrhenius equation:

$$k = B e^{-E_A/RT} \quad (1.21)$$

where  $E_A$  is the activation energy and  $B$  is the frequency factor and can be expressed in the following form:

$$B = C e^{\Delta S^\ddagger/R} \quad (1.22)$$

in which  $C$  is a constant and  $\Delta S^\ddagger$  is the standard entropy of activation.

If the pressure is constant,

$$E_A \approx \Delta H^\ddagger \quad (1.23)$$

where  $\Delta H^\ddagger$  is the standard enthalpy of activation.

Substituting Equations 1.22 and 1.23 in Equation 21, Equation 1.24 is obtained:

$$k = C e^{-(\Delta H^\ddagger - T\Delta S^\ddagger)/RT} \quad (1.24)$$

which can be rewritten as Equation 1.25.

$$k = C e^{-\Delta G^\ddagger/RT} \quad (1.25)$$

with  $\Delta G^\ddagger$  representing the standard free energy of activation.

When a potential,  $E$ , is imposed on the electrode relative to the formal potential,  $E^{\ominus'}$ , the standard free energy of activation of reduction,  $\Delta G_c^\ddagger$ , and oxidation,  $\Delta G_a^\ddagger$ , can be calculated by Equations 1.26 and 1.27, respectively:

$$\Delta G_c^\ddagger = \Delta G_{c,0}^\ddagger + \alpha_c nF(E - E^{\ominus'}) \quad (1.26)$$

$$\Delta G_a^\ddagger = \Delta G_{a,0}^\ddagger - \alpha_a nF(E - E^{\ominus'}) \quad (1.27)$$

where  $\alpha_c$  and  $\alpha_a$  are the cathodic and the anodic charge transfer coefficients, respectively; the subscript 0 refers to the reference state at formal potential.

From Equations 1.26 and 1.27, if  $E > E^{\ominus'}$ ,  $\Delta G_c^\ddagger$  will increase and  $\Delta G_a^\ddagger$  will be reduced so oxidation is favoured. On the other hand, if  $E < E^{\ominus'}$ , reduction is promoted.

Using Equations 1.25 to 1.27, the constants for cathodic,  $k_c$ , and anodic semi-reactions,  $k_a$ , are calculated by Equations 1.28 and 1.29, respectively:

$$k_c = C_c e^{-(\Delta G_{c,0}^\ddagger)/RT} e^{-(\alpha_c n F (E - E^{\phi'}))/RT} \quad (1.28)$$

$$k_a = C_a e^{-(\Delta G_{a,0}^\ddagger)/RT} e^{(\alpha_a n F (E - E^{\phi'}))/RT} \quad (1.29)$$

Since  $B e^{-(\Delta G_{c,0}^\ddagger)/RT}$  and  $B e^{-(\Delta G_{a,0}^\ddagger)/RT}$  are constant, these quantities are replaced by  $k_{c,0}$  and  $k_{a,0}$  and Equations 1.30 and 1.31 are obtained.

$$k_c = k_{c,0} e^{-(\alpha_c n F (E - E^{\phi'}))/RT} \quad (1.30)$$

$$k_a = k_{a,0} e^{(\alpha_a n F (E - E^{\phi'}))/RT} \quad (1.31)$$

At equilibrium, for a first order reaction,

$$k_a [O]_* = k_c [R]_* \quad (1.32)$$

And if  $[O]_* = [R]_*$ ,

$$k_a = k_c = k_0 \quad (1.33)$$

in which  $k_0$  is the standard rate constant.

Substituting Equation 1.33 in Equation 1.30 and 1.31,  $k_c$  and  $k_a$  can be written as

$$k_c = k_0 e^{-\alpha_c n F (E - E^{\phi'})/RT} \quad (1.34)$$

$$k_a = k_0 e^{\alpha_a n F (E - E^{\phi'})/RT} \quad (1.35)$$

Considering a single charge transfer and a single step reaction,  $\alpha_a + \alpha_c = 1$ , Equation 1.36 is obtained by substituting Equations 1.34 and 1.35 in Equation 1.20.

$$i = F A k_0 \left[ [O]_* e^{-\alpha_c n F (E - E^{\phi'})/RT} - [R]_* e^{(1 - \alpha_c) n F (E - E^{\phi'})/RT} \right] \quad (1.36)$$

At equilibrium,  $E = E_{eq}$ , the net current is zero and the concentrations at the electrode surface and in the bulk are equal, i. e.,  $[O]_* = [O]_\infty$  and  $[R]_* = [R]_\infty$ , so:

$$i = F A k_0 \left[ [O]_\infty e^{-\alpha_c n F (E_{eq} - E^{\ominus'}) / RT} - [R]_\infty e^{(1-\alpha_c) n F (E_{eq} - E^{\ominus'}) / RT} \right] \quad (1.37)$$

since  $i = 0$ ,

$$\frac{[O]_\infty}{[R]_\infty} = e^{n F (E_{eq} - E^{\ominus'}) / RT} \quad (1.38)$$

At equilibrium, the magnitude of the cathodic current,  $i_c$ , equals that of the anodic current,  $i_a$ , which results in zero net current,  $i_0 = 0$ . The current in each of the directions is called the exchange current,  $i_0$ :

$$|i_0| = |i_c| = |i_a| \quad (1.39)$$

$i_0$  can be calculated in terms of forward reaction:

$$i_0 = F A k_0 [ [O]_\infty e^{-\alpha_c n F (E_{eq} - E) / RT} ] \quad (1.40)$$

Raising Equation 1.38 to the  $-\alpha_c$  power:

$$\left( \frac{[O]_\infty}{[R]_\infty} \right)^{-\alpha_c} = e^{-\alpha_c n F (E_{eq} - E^{\ominus'}) / RT} \quad (1.41)$$

and substituting Equation 1.41 in Equation 1.36, Equation 1.42 is obtained:

$$i_0 = F A k_0 [O]_\infty^{(1-\alpha_c)} [R]_\infty^{(\alpha_c)} \quad (1.42)$$

Dividing Equation 1.36 by Equation 1.42,

$$\frac{i}{i_0} = \frac{[O]_* e^{-\alpha_c n F (E - E^{\ominus'}) / RT}}{[O]_\infty^{(1-\alpha_c)} [R]_\infty^{(\alpha_c)}} - \frac{[R]_* e^{(1-\alpha_c) n F (E - E^{\ominus'}) / RT}}{[O]_\infty^{(1-\alpha_c)} [R]_\infty^{(\alpha_c)}} \quad (1.43)$$

And rearranging:

$$\frac{i}{i_0} = \frac{[O]_* e^{-\alpha_c nF(E-E^{\ominus'})/RT}}{[O]_{\infty}} \left( \frac{[O]_{\infty}}{[R]_{\infty}} \right)^{\alpha_c} - \frac{[R]_* e^{(1-\alpha_c)nF(E-E^{\ominus'})/RT}}{[R]_{\infty}} \left( \frac{[O]_{\infty}}{[R]_{\infty}} \right)^{-(1-\alpha_c)} \quad (1.44)$$

Using  $[O]_{\infty}/[R]_{\infty}$  from Equation 1.38, Equation 1.44 can be written as:

$$i = i_0 \left[ \frac{[O]_*}{[O]_{\infty}} e^{-\alpha_c nF\eta/RT} - \frac{[R]_*}{[R]_{\infty}} e^{(1-\alpha_c)nF\eta/RT} \right] \quad (1.45)$$

where  $\eta = E - E_q$  called the activation overpotential.

If the solution is well stirred or the current is very small, the concentration in the bulk and at the electrode surface are identical and Equation 1.43 can be simplified to : [46].

$$i = i_0 \left[ e^{-\alpha_c nF\eta/RT} - e^{(1-\alpha_c)nF\eta/RT} \right] \quad (1.46)$$

Equation 1.46 is the well-known Butler-Volmer Equation, which relates the current with the activation overpotentials.

In terms of current density, Equation 1.46 can be written in the form of Equation 1.47.

$$j = j_0 \left[ e^{-\alpha_c nF\eta/RT} - e^{(1-\alpha_c)nF\eta/RT} \right] \quad (1.47)$$

Equation 1.47 has two limiting cases:

a) Small overpotentials ( $|\eta| < 5$  mV) - Equation 1.47 may be linearized by the first terms of a Taylor series expansion ( $e^x \approx 1 + x$ ) leading to Equation 1.48.

$$j = j_0 \left( \frac{-n\eta F}{RT} \right) \quad (1.48)$$

- b) Large positive or large negative overpotentials. For example, at large positive potentials, the backward reaction is predominant and the forward reaction can be neglected. In this case, Equation 1.47 can be simplified to Equation 1.49.

$$|j| = j_0 \exp\left(\frac{(1 - \alpha_c)n\eta F}{RT}\right) \quad (1.49)$$

Applying logarithms and rearranging Equation 1.49:

$$\eta = b\{\ln(j_0) - \ln(|j|)\} \quad (1.50)$$

where  $b$  is the Tafel slope.

$$b = \left(\frac{RT}{(1 - \alpha_c)nF}\right) \quad (1.51)$$

## 1.11 Mechanisms of chlorine evolution reaction

Since the introduction of DSA<sup>®</sup> anodes as anodes for chlor-alkali cells, several scientific articles addressing the mechanism of the chlorine evolution reaction (CIER) have been published.

The first mechanistic study of chlorine evolution on titanium coated with mixed oxides of noble metals dates back to 1972 [48]. In this work, Faita and Fiori proposed a two-step mechanism (Mechanism 1) for the evolution of chlorine on a thermally deposited RuO<sub>2</sub>-IrO<sub>2</sub>-TiO<sub>2</sub> coating on a titanium substrate. This mechanism is supported by the 30 - 40 mV decade<sup>-1</sup> Tafel slopes found in the experiments carried out in their work. The mechanism is similar to the one found for Pt-Ir alloys on titanium and includes a first electrochemical step, followed by a chemical step [49]. Faita and Fiori proposed the second step to be the rate-determining step.

### Mechanism 1



where S is the active site in which the chloride ions adsorb.

In the same year, using a DSA® anode coated with 30 RuO<sub>2</sub> + 70 % TiO<sub>2</sub> (molar fraction), Erenburg and co-workers (cited in [50]) presented a mechanism which considers three steps, similar to the so-called Volmer-Heyrovsky-Tafel steps applied to the mechanism of cathodic hydrogen evolution (Mechanism 2). This approach leads to two different pathways. Regardless of the pathway, the first or Volmer step is the chloride discharge, i. e., the adsorption of chloride on the metal oxide active site. Then, two parallel routes are possible: the Volmer step may be followed by the Heyrovsky step in which a chloride ion in solution reacts with the adsorbed species leading to the formation and desorption of chlorine; on the other hand, two adsorbed chloride ions may react with each other to form a desorbed chlorine molecule; this last is known as the Tafel or recombination step.

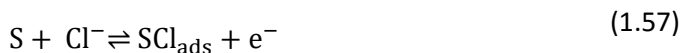
### Mechanism 2



According to these authors, pathway (1.54) + (1.56) is expected close to equilibrium potentials whereas pathway (1.54) + (1.55) prevails at higher potentials.

Although this mechanism predicts 30-40 mV decade<sup>-1</sup> Tafel slopes, the mechanism is not compatible with a reaction order of 1 in relation to chloride concentration, found later by the same group (cited in [50]). In order to respect the first order dependence of the reaction rate on the chloride concentration, Erenburg and co-workers proposed in 1975 a new CIER mechanism:

### Mechanism 3



Mechanism 3 predicts the formation of a positively charged chlorine compound,  $SCl_{ads}^+$ , although the nature of this compound was not specified.

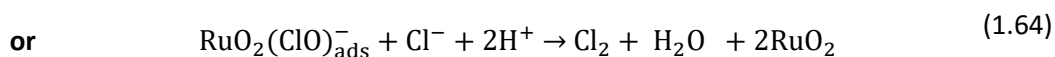
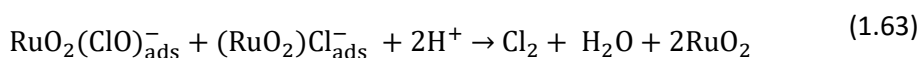
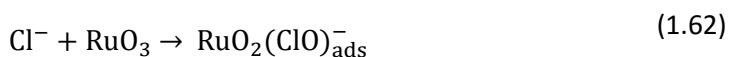
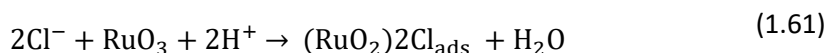
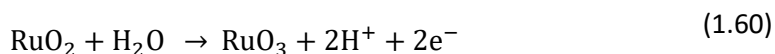
Mechanisms 1 to 3 have been proposed on the assumption of the independence of the CIER on the solution pH. The first CIER study in which the effect of the pH was assessed was carried out by Janssen and co-authors in 1977 [51]. Within the pH range analysed, 0 to 3, the CIER was reported to be independent of the solution pH. In their study, Janssen and co-authors, working with two different DSA® anode coatings (one similar to the one used by Erenburg - 30 %  $RuO_2$  + 70 %  $TiO_2$  (molar fraction) - and other coating made of pure ruthenium) reported Tafel slopes between 40 and 60  $mV \text{ decade}^{-1}$ . Values around 40  $mV \text{ decade}^{-1}$  support the Volmer-Heyrovsky mechanism with the Heyrovsky as rate-determining step. The values around 60  $mV \text{ decade}^{-1}$  were justified by the ineffective electric contact between the titanium substrate and the coating.

In the same year, Harrison and co-workers published their first article on the study of the CIER on metallic oxides [52]. In this article, based on the results obtained by electrochemical impedance spectroscopy and on the 30  $mV \text{ decade}^{-1}$  Tafel slope, the authors proposed the Volmer- Tafel mechanism with the Tafel as rate-determining step for the CIER on a titanium electrode coated with a  $RuO_2$  -  $TiO_2$  film. In the following year, the same authors published a new article on the same topic [53], this time, addressing the effect of ratio  $RuO_2$  -  $TiO_2$  on the CIER. Tafel slopes between 40 and 61  $mV \text{ decade}^{-1}$  were reported in this work. The higher values correspond to the lowest  $RuO_2$  relative composition tested (5 % molar fraction) and the lower values were found to  $RuO_2$  relative composition beyond 20 % molar fraction. These authors also reported 30  $mV \text{ decade}^{-1}$

Tafel slopes for some samples with 35 % in mole of RuO<sub>2</sub>. This last result supports the findings of the previous study that suggests the Volmer-Tafel mechanism, although the 40 mV decade<sup>-1</sup> Tafel slopes supports the Volmer-Heyrovsky mechanism.

In the same year Augustynski and co-authors, based only on X-Ray photoelectron spectroscopic (XPS) studies of new and used samples of RuO<sub>2</sub> and RuO<sub>2</sub> – TiO<sub>2</sub> DSA<sup>®</sup> anodes proposed a new mechanism for the CIER [54]. The XPS analysis detected the presence of RuO<sub>3</sub> and the analysis of the used samples showed a large amount of chlorine species. These authors assigned these chlorine species to adsorbed chlorine compounds which would support a high fraction of surface sites occupied by Cl<sub>ads</sub> ( $\theta \approx 1$ ). This assumption was later rejected since the high chloride content detected by XPS could be justified by trapped chlorine and not only by adsorbed chlorine [50]. The mechanism proposed by Augustynski and co-authors is described by Equations 1.60 to 1.64 and, for the first time, a surface oxidation step preceding the chloride adsorption is mentioned (Equation 1.60).

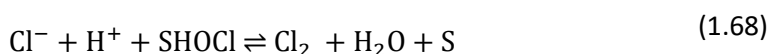
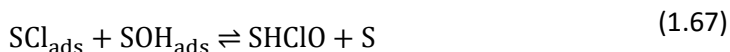
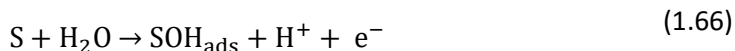
#### Mechanism 4



One year later, in 1979, the group headed by Harrison [55] suggested a new mechanism compatible with the 40 mV decade<sup>-1</sup> Tafel slope and a reaction order of 1 with respect to chloride. This mechanism described by Equations 1.65 to 1.68, involves the

participation of water in the CIER. This mechanism was confirmed by the same group in articles published in the following years [56, 57].

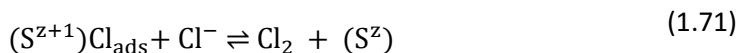
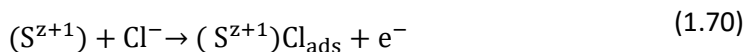
#### Mechanism 5



With the presence of protons ( $H^{+}$ ), this mechanism suggests that pH has an important role on the CIER, although the authors do not mention this pH effect.

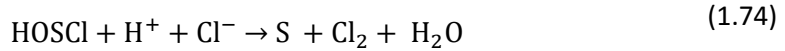
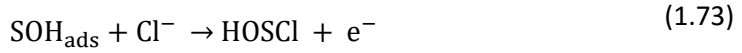
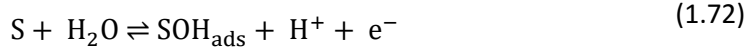
Continuing their investigation in this field, Krishtalik published an article in 1981 in which he proposes two alternatives to describe the CIER at DSA<sup>®</sup> anodes[58]. The first is Mechanism 3; the alternative mechanism is Mechanism 6. This mechanism predicts the oxidation of the substrate preceding the chloride adsorption. Mechanism 6 is described by Equation 1.69 to 1.71.

#### Mechanism 6



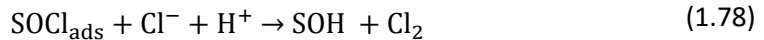
In the same year, 1981, Erenburg claimed for the first time the effect of pH on the CIER (cited in [50]). According to his findings, the  $H^{+}$  concentration has negative effect on the rate of the CIER. The mechanism proposed by Erenburg is Mechanism 7.

### Mechanism 7



Three years later, in 1984 (cited in [50]), Erenburg restated the negative order of the reaction with respect to  $H^+$  concentration. However, Erenburg mentioned that this effect did not necessarily require that water discharge (Equation 1.72) is part of the mechanism of the ClER. According to the author, the pH effect could be due to acid-base equilibrium processes that occur on metal oxide electrodes, preceding the ClER. According to this, Erenburg suggested Mechanism 8.

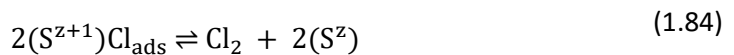
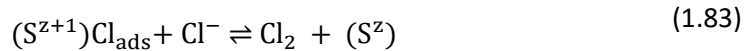
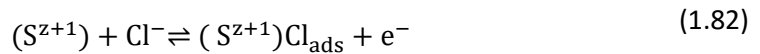
### Mechanism 8



More recently, in 2002, Fernández and co-workers addressed the study of ClER by analysing the polarization resistance [59, 60]. This technique was applied to the study ClER on titanium electrodes coated with a  $RuO_2$  films. The first of these articles [59] addresses the influence of pH on the ClER and confirmed the inhibition of the ClER when  $H^+$  concentration increases. After assessing the Volmer-Krishtalik mechanism in their second article [59], the authors concluded that this mechanism describes only partially the ClER. In

the search for a more complete model to describe the CIER, in the last of the three articles [60], the authors proposed a new mechanism for the CIER – Mechanism 9. This mechanism restates the existence of a first step independent of the CIER, which is related to the acid-base equilibrium of the electrode and shows the active role of the pH on the reaction. This step is followed by the electrochemical oxidation of active sites in which chloride ions will adsorb. Chlorine can then be generated by two different routes – by the recombination of two adsorbed chloride intermediates or by the reaction between one adsorbed species and one chloride ion in solution. Mechanism 9 is described by equation 1.79 to 1.83. The last three equations are the Volmer-Krishtalik-Tafel reactions, already mentioned in Mechanism 2 and Mechanism 6.

### Mechanism 9



## 1.12 Accelerated Ageing tests

Taking into account the long life of the DSA anodes (up to 8 years in operation), the study of the deactivation phenomena occurring on these electrodes is infeasible in a reasonable range of time if the cell is under nominal industrial conditions. Accelerated ageing tests have been developed to increase the rate of the deactivation processes leading to a sharp and measurable loss of anode activity in a reasonable period of time [61]. This reduction of the lifetime of the electrodes is achieved by exposing the electrodes to harsh operation conditions that promote their degradation. The typical manipulated

variables are the temperature, the electrolyte composition or concentration, pH and current density.

Table 1.3 lists the operation conditions used for accelerated ageing tests available in literature. Here, only the studies on DSA<sup>®</sup> anodes prepared by thermal decomposition methods and coated with a metal oxide mixture containing at least two out of the following metal oxides TiO<sub>2</sub>, RuO<sub>2</sub>, IrO<sub>2</sub> are presented. As a reference, the normal operation conditions in the anodic compartment of a chlor-alkali membrane cell are present in Table 1.2 [2, 3].

**Table 1.2 – Normal operation conditions in the anodic compartment of a chlor-alkali membrane cell**

<b>Current density / A cm<sup>-2</sup></b>	<b>Temperature / °C</b>	<b>Inlet NaCl concentration / wt. %</b>	<b>pH</b>
0.3 – 0.6	90 - 96	24 - 26	2 - 4

Despite several variables can be manipulated to promote very fast degradation of the electrode active coating, the ageing tests should mimic and intensify the processes occurring during normal operation conditions of the cell and not to create new degradation pathways. This is a key point that should not be underestimated since the aim is to correlate the data obtained with the industrial operation. As Comninellis and Vercesi [61] refer, the wear mechanisms are dependent on the electrolyte. It is pointless using H<sub>2</sub>SO<sub>4</sub> as electrolyte to study electrodes for chlorine evolution since the processes occurring in the electrode will not be the same as those occurring during normal operation of the electrodes is sodium chloride solutions. This has been shown by Hoseinieh et al. [62] who found different deactivation mechanisms for similar DSA<sup>®</sup> anodes (RuO<sub>2</sub>-IrO<sub>2</sub>-TiO<sub>2</sub>) ageing in NaCl 0.5 mol dm<sup>-3</sup> and in 1.0 mol dm<sup>-3</sup> H<sub>2</sub>SO<sub>4</sub>. While in NaCl solutions the main deactivation processed was assigned to the growth of a passive TiO<sub>2</sub> layer at the coating-substrate interface, for DSA<sup>®</sup> anodes aged in H<sub>2</sub>SO<sub>4</sub>, the electrode performance loss resulted from the dissolution of the noble metals ruthenium and iridium.

The large range of failure times seen in Table 1.3, from some minutes to many hours, found in the literature, is a result of the wide range of coating specifications as well as different ageing conditions applied in each study. Even in tests with similar operating conditions and compositions, the results of the different tests are not easily comparable. Indeed, the variables such as the coating thickness, the annealing temperature and time, among others have a critical role on the electrode properties and so on the ageing times of the electrodes [2, 61, 63, 64] which make immediate comparison of the electrode performance not possible.

**Table 1.3 – Literature review of the operation conditions of accelerated ageing test of DSA anodes**

Reference	Year	Electrolyte	Temperature / °C	Current density /A cm <sup>-2</sup>	Electrode composition	Failure time /h
[65]	1977	0.25 M H <sub>2</sub> SO <sub>4</sub>	20	1.5	Ti/ TiO <sub>2</sub> -RuO <sub>2</sub>	2.5
[66]	1979	2 M HClO <sub>4</sub> + xM NaCl, x= [0-2]	40	1	Ti/ TiO <sub>2</sub> -RuO <sub>2</sub>	1 –inf
[66]	1979	2 M HClO <sub>4</sub> + xM NaCl, x= [0-2]	40	2	Ti/ TiO <sub>2</sub> -RuO <sub>2</sub>	0.5 –250
[66]	1979	2 M HClO <sub>4</sub> + 0.2 M NaCl	40	4	Ti/ TiO <sub>2</sub> -RuO <sub>2</sub>	0.1
[67]	1981	1 M H <sub>2</sub> SO <sub>4</sub>	25	1.0	Ti/ TiO <sub>2</sub> -RuO <sub>2</sub>	20
[68]	1981	1 M KOH	30	0.50	Ti/ TiO <sub>2</sub> -RuO <sub>2</sub>	113
[61]	1991	3.85 M H <sub>2</sub> SO <sub>4</sub>	80	0.75	Ti/ Ta <sub>2</sub> O <sub>5</sub> -IrO <sub>2</sub>	50- 250
[63]	1997	0.5 M H <sub>2</sub> SO <sub>4</sub>	25	0.50	Ti/ RuO <sub>2</sub> -TiO <sub>2</sub>	0.5 – 3
[69]	1997	2 M H <sub>2</sub> SO <sub>4</sub>	25	1.5	Ti/ TiO <sub>2</sub> -RuO <sub>2</sub>	16
[70]	1998	1 M HClO <sub>4</sub>	32	0.40	Ti/ Ir <sub>0.3</sub> Ti <sub>0.7</sub> O <sub>2</sub>	510
[71]	2000	0.5 M NaCl, pH 2	33	2	Ti/ RuO <sub>2</sub> -TiO <sub>2</sub>	10-33
[72]	2003	1 M H <sub>2</sub> SO <sub>4</sub>	30	2	Ti/ IrO <sub>2</sub> -Ta <sub>2</sub> O <sub>5</sub>	482
[73]	2004	0.5 M H <sub>2</sub> SO <sub>4</sub>	80	0.75	Ti/ RuO <sub>2</sub> -TiO <sub>2</sub>	2.5
[74]	2005	0.5 M NaCl, pH 2	25	0.70	Ti/TiO <sub>2</sub> -RuO <sub>2</sub>	31
[75]	2006	0.5 M H <sub>2</sub> SO <sub>4</sub>	80	0.75	Ti/ RuO <sub>2</sub> -Ta <sub>2</sub> O <sub>5</sub>	N/A

**Table 1.3 – Literature review of the operation conditions of accelerated ageing test of DSA anodes (continued)**

<b>Reference</b>	<b>Year</b>	<b>Electrolyte</b>	<b>Temperature / °C</b>	<b>Current density /A cm-2</b>	<b>Electrode composition</b>	<b>Failure time /h</b>
[76]	2006	1 M HClO <sub>4</sub>	25	0.80	Ti/ Ir <sub>0.3</sub> Ti <sub>0.7</sub> O <sub>2</sub>	40
[21]	2010	0.5 M NaCl, pH 2	25	2	Ti/ TiO <sub>2</sub> -RuO <sub>2</sub> -IrO <sub>2</sub>	293
[77]	2011	0.5 M NaCl, pH 2	25	0.60	Ti/ Ru <sub>0.3</sub> Ti <sub>0.7</sub> O <sub>2</sub> Ti/ Ru <sub>0.3</sub> Ti <sub>0.4</sub> Ir <sub>0.3</sub> O <sub>2</sub>	18 30
[78]	2011	0.5 M NaCl	35	1	Ti/ RuO <sub>2</sub> -SbO <sub>5</sub> -SnO <sub>2</sub>	266
[62]	2013	1 M H <sub>2</sub> SO <sub>4</sub> 0.5 M NaCl, pH 2	25	2	Ti/ Ru <sub>0.25</sub> Ir <sub>0.25</sub> Ti <sub>0.5</sub> O <sub>2</sub>	104 293

## 1.13 Deactivation mechanisms

The main purpose of accelerated ageing tests is to obtain, in useful time, information about the processes that lead to the performance loss of the electrode. If the tests are trustworthy, i.e., are able to mimic the normal operation of the electrodes, meaningful information about the deactivation mechanism of the industrial electrodes operating in normal operation condition can be extrapolated. The identification of the deactivation mechanisms of the DSA® anodes is critical to define strategies to reduce its rate and to increase the electrode lifetime. The cause for anode deactivation can be aggregated in four main categories:

1. Contamination of the active surface by impurities such as  $\text{MnO}_2$ ,  $\text{SiO}_2$ ,  $\text{BaSO}_4$ , or iron compounds. Impurities affect the electrode performance via two different routes: blockage of the surface ( $\text{MnO}_2$ ,  $\text{SiO}_2$ ,  $\text{BaSO}_4$ ) or via the reaction of the impurities such as iron compounds that oxide on the anode [2].
2. Selective electrochemical dissolution by oxidation of electroactive metals (Ir and Ru) to higher oxidation degrees, forming soluble species [22, 69, 70, 72, 74];
3. Erosion of the electroactive species present in the coating caused by the intense gas evolution in the electrode [21, 69, 70, 72]

The reduction of electrocatalysts (points 2 and 3) in the coating leads to the increase of the anode overpotential increase which may happen in two different ways [2]:

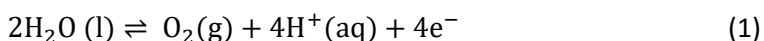
- The coating conductivity decreases due to the higher resistivity of the valve metal ( $\text{TiO}_2$ ) that remains on the electrode and has its fraction in the coating increased after the active metal oxides partially leave it;

- The change of the chlorine evolution mechanism from one involving intermediates (Tafel slopes 30-40  $\text{mV decade}^{-1}$ ) to a slow electron transfer step (120  $\text{mV decade}^{-1}$  Tafel slope). This is a result of the reduction of the number of electroactive sites for reaction.

4. Growth of a passive  $\text{TiO}_2$  layer at the substrate-coating interface [21, 22, 70, 72, 74, 75]. This phenomenon takes place due to the penetration of the electrolyte through the oxide coating towards to the titanium substrate-oxide coating interface. In contact with the

electrolyte, the titanium substrate is oxidized to  $\text{TiO}_2$ . The formation of this insulating layer causes a sudden increase of the potential [21, 22] and could be the precursor of coating detachment [22],

While the contamination of the surface by impurities can be prevented and minimized by improving the feed brine treatment, erosion and dissolution of the coating cannot be easily addressed since they are intrinsically related with the chlorine evolution itself or with oxygen evolution. The evolution of oxygen via water oxidation (Equation 1.85) is the main side reaction occurring on anodes in chlor-alkali cells [2]. Since the standard reduction potential for the oxygen evolution (1.23 V) is lower than the potential for chlorine evolution, oxygen evolution is thermodynamically favored.



This side reaction not only reduces the efficiency of the process, but also promotes the oxidation and dissolution of ruthenium species [2]. The reduction of the oxygen fraction can be minimized by operating the cell at lower pH (about 2) or increasing the sodium chloride concentration [1, 2]. Operating the chlor-alkali cell at higher current density also reduces the production ratio  $\text{O}_2 / \text{Cl}_2$  since the chlorine formation is kinetically favored [2, 3]. Concerning the ruthenium dissolution, it can be minimized by adding iridium oxide to the binary titanium oxide-ruthenium [2, 21, 77].

Regarding the growth of the titanium oxide passive layer at the substrate-coating interface, since this is related to the access of the electrolyte through the coating, the coating porosity is a critical parameter; the coating porosity depends on the calcination temperature of the electrode preparation. Higher calcination temperatures increase the roughness and porosity of the electrode, increasing the internal surface area and double layer capacitance, but also facilitate the penetration of the electrolyte towards the substrate [40]. The buildup of a  $\text{TiO}_2$  at the coating-substrate interface is often consequence of the erosion and dissolution of the coating since these phenomena lead to the reduction of the coating thickness and compactness making the substrate easier to access. This sequence of events has been reported by various authors. [22, 70, 74].

## 1.14 References

1. Schmittinger, P., *Chlorine: Principles & Industrial Practice*. 2000, Weinheim: Wiley-VCH.
2. O'Brien, T., T.V. Bommaraju, and F. Hine, *Handbook of chlor-alkali technology*. 2005, New York: Springer.
3. Schmittinger, P., et al., *Chlorine in Ullmann's Encyclopedia of Industrial Chemistry, Electronic release*, B. Elvers, Editor. 2012, Wiley-VCH: Weinheim. p. 531-621.
4. Kurt, C. and J. Bittner, *Sodium Hydroxide in Ullmann's Encyclopedia of Industrial Chemistry, Electronic release*. 2000, Wiley-VCH Weinheim. p. 371-382.
5. Eggeman, T., *Sodium Hydroxide in Kirk-Othmer Encyclopedia of Chemical Technology, Electronic release*. 2000, John Wiley & Sons, Inc.: New York.
6. Bommaraju, T.V., et al., *Chlorine in Kirk-Othmer Encyclopedia of Chemical Technology, Electronic release*, R.E. Kirk and D.F. Othmer, Editors. 2002, John Wiley & Sons, Inc.: New York.
7. Trasatti, S., *Electrocatalysis: understanding the success of DSA<sup>®</sup>*. *Electrochimica Acta*, 2000. **45**(15-16): p. 2377-2385.
8. Brinkmann, T., et al., *Best Available Techniques - Reference Document for the Production of Chlor-alkali*. 2014, Luxembourg.
9. *Euro Chlor*. Accessed in: September 2015; Available from: [www.eurochlor.org](http://www.eurochlor.org).
10. Moussallem, I., et al., *Chlor-alkali electrolysis with oxygen depolarized cathodes: history, present status and future prospects*. *Journal of Applied Electrochemistry*, 2008. **38**(9): p. 1177-1194.
11. Faita, G. and F. Federico, Patent US7670472, (2010).
12. Perry, M.L., Patent US20100314261, (2010).
13. Figueiredo, R.S., R. Bertazzoli, and C.A. Rodrigues, *Copper/Carbon/PTFE Oxygen-Depolarized Cathodes for Chlor-alkali Membrane Cells*. *Industrial & Engineering Chemistry Research*, 2013. **52**(16): p. 5611-5615.
14. Woltering, P., et al., *Energy-saving chlorine production – Chlor-alkali electrolysis using innovative cathode technology*. *Thyssenkrupp techforum*, 2013(1): p. 18 - 23.
15. *American Chemistry Council*. Accessed in: September 2015; Available from: [chlorine.americanchemistry.com](http://chlorine.americanchemistry.com).
16. Hammond, J.S., et al., *The application of X-ray photoelectron-spectroscopy to a study of interfacial composition in corrosion-induced paint de-adhesion*. *Corrosion Science*, 1981. **21**(3): p. 239-253.
17. Beer, H.B., *The Invention and Industrial Development of Metal Anodes*. *Journal of The Electrochemical Society*, 1980. **127**(8): p. 303C-307C.
18. Stevens, R.H., Patent US 1077894, (1913).
19. Cotton, J.B., E.C. Williams, and A.H. Barber, Patent GB 877901, (1961).
20. Beer, H.B., Patent GB 1147442, (1969).
21. Hoseinie, S.M., F. Ashrafizadeh, and M.H. Maddahi, *A Comparative Investigation of the Corrosion Behavior of RuO<sub>2</sub> – IrO<sub>2</sub> – TiO<sub>2</sub> Coated Titanium Anodes in Chloride Solutions*. *Journal of The Electrochemical Society*, 2010. **157**(4): p. E50-E56.

22. Hu, J.M., et al., *Degradation mechanism of long service life Ti/IrO<sub>2</sub>-Ta<sub>2</sub>O<sub>5</sub> oxide anodes in sulphuric acid*. Corrosion Science, 2002. **44**(8): p. 1655-1668.
23. Beer, H.B., Patent GB 1195871, (1970).
24. Beer, H.B., Patent US 3265526, (1966).
25. Beer, H.B., Patent US 3632498, (1972).
26. Beer, H.B., Patent US 3711385, (1973).
27. Kötzt, R. and S. Stucki, *Stabilization of RuO<sub>2</sub> by IrO<sub>2</sub> for anodic oxygen evolution in acid media*. Electrochimica Acta, 1986. **31**(10): p. 1311-1316.
28. Liederbach, T.A., *Metal Anodes in Kirk-Othmer Encyclopedia of Chemical Technology, Electronic release*. 2000, John Wiley & Sons, Inc.: New York.
29. Trasatti, S. and G. Buzzanca, *Ruthenium dioxide: A new interesting electrode material. Solid state structure and electrochemical behaviour*. Journal of Electroanalytical Chemistry and Interfacial Electrochemistry, 1971. **29**(2): p. A1-A5.
30. Ardizzone, S., G. Fregonara, and S. Trasatti, "Inner" and "outer" active surface of RuO<sub>2</sub> electrodes. Electrochimica Acta, 1990. **35**(1): p. 263-267.
31. Arikado, T., C. Iwakura, and H. Tamura, *Electrochemical behaviour of the ruthenium oxide electrode prepared by the thermal decomposition method*. Electrochimica Acta, 1977. **22**(5): p. 513-518.
32. Lodi, G., et al., *On some debated aspects of the behaviour of RuO<sub>2</sub> film electrodes*. Materials Chemistry, 1978. **3**(3): p. 179-188.
33. Michell, D., D.A.J. Rand, and R. Woods, *A study of ruthenium electrodes by cyclic voltammetry and X-ray emission spectroscopy*. Journal of Electroanalytical Chemistry and Interfacial Electrochemistry, 1978. **89**(1): p. 11-27.
34. Galizzioli, D., F. Tantardini, and S. Trasatti, *Ruthenium dioxide: a new electrode material. I. Behaviour in acid solutions of inert electrolytes*. Journal of Applied Electrochemistry, 1974. **4**(1): p. 57-67.
35. Galizzioli, D., F. Tantardini, and S. Trasatti, *Ruthenium dioxide: a new electrode material. II. Non-stoichiometry and energetics of electrode reactions in acid solutions*. Journal of Applied Electrochemistry, 1975. **5**(3): p. 203-214.
36. Trasatti, S., *Surface-chemistry of oxides and electrocatalysis*. Croatica Chemica Acta, 1990. **63**(3): p. 313-329.
37. Conway, B.E., *Electrochemical Supercapacitors: Scientific Fundamentals and Technological Applications*. 1999: Springer US.
38. Zheng, J.P., P.J. Cygan, and T.R. Jow, *Hydrous Ruthenium Oxide as an Electrode Material for Electrochemical Capacitors*. Journal of the Electrochemical Society, 1995. **142**(8): p. 2699-2703.
39. Roginskaya, Y.E., et al., *Formation, structure and electrochemical properties of IrO<sub>2</sub>-RuO<sub>2</sub> oxide electrodes*. Materials Chemistry and Physics, 1991. **30**(2): p. 101-113.
40. Lassali, T.A.F., J.F.C. Boodts, and L.O.S. Bulhões, *Charging processes and electrocatalytic properties of IrO<sub>2</sub>/TiO<sub>2</sub>/SnO<sub>2</sub> oxide films investigated by in situ AC impedance measurements*. Electrochimica Acta, 1999. **44**(24): p. 4203-4216.
41. Lokhande, C.D., D.P. Dubal, and O.-S. Joo, *Metal oxide thin film based supercapacitors*. Current Applied Physics, 2011. **11**(3): p. 255-270.

42. Panić, V.V., et al., *Differences in the electrochemical behavior of ruthenium and iridium oxide in electrocatalytic coatings of activated titanium anodes prepared by the sol-gel procedure*. Journal of the Serbian Chemical Society, 2010. **75**(10): p. 1413-1420.
43. Trasatti, S., *Oxide/aqueous solution interfaces, interplay of surface chemistry and electrocatalysis*. Materials Chemistry and Physics, 1987. **16**(2): p. 157-174.
44. Brett, C.M.A. and A.M. Oliveira-Brett, *Electrochemistry : principles, methods, and applications*. 1993, Oxford ; New York: Oxford University Press.
45. Dias, A.C., *Chlor-alkali membrane cell process study and characterization*. 2010, Universidade do Porto: Porto.
46. Bard, A.J. and L.R. Faulkner, *Electrochemical methods : fundamentals and applications*. 2nd ed. 2001, New York: Wiley. xxi, 833 p.
47. O'Hayre, R.P., *Fuel cell fundamentals*. 2006, Hoboken, NJ: John Wiley & Sons. xxii, 409 p.
48. Faita, G. and G. Fiori, *Anodic discharge of chloride ions on oxide electrodes*. Journal of Applied Electrochemistry, 1972. **2**(1): p. 31-35.
49. Faita, G., G. Fiori, and J.W. Augustynski, *Electrochemical Processes of the Chlorine-Chloride System on Platinum-Iridium-Coated Titanium Electrodes*. Journal of The Electrochemical Society, 1969. **116**(7): p. 928-932.
50. Trasatti, S., *Progress in the understanding of the mechanism of chlorine evolution at oxide electrodes*. Electrochimica Acta, 1987. **32**(3): p. 369-382.
51. Janssen, L.J.J., et al., *Mechanism of the chlorine evolution on a ruthenium oxide/titanium oxide electrode and on a ruthenium electrode*. Electrochimica Acta, 1977. **22**(10): p. 1093-1100.
52. Burrows, I.R., J.H. Entwisle, and J.A. Harrison, *The mechanism of oxidation of Cl<sup>-</sup> on platinum and RuO<sub>2</sub>/TiO<sub>2</sub> electrodes, and the reduction of Cl<sub>2</sub> on platinum*. Journal of Electroanalytical Chemistry and Interfacial Electrochemistry, 1977. **77**(1): p. 21-34.
53. Burrows, I.R., D.A. Denton, and J.A. Harrison, *Chlorine and oxygen evolution on various compositions of RuO<sub>2</sub>/TiO<sub>2</sub> electrodes*. Electrochimica Acta, 1978. **23**(6): p. 493-500.
54. Augustynski, J., L. Balsenc, and J. Hinden, *X-Ray Photoelectron Spectroscopic Studies of RuO<sub>2</sub> - Based Film Electrodes*. Journal of The Electrochemical Society, 1978. **125**(7): p. 1093-1097.
55. Denton, D.A., J.A. Harrison, and R.I. Knowles, *Chlorine evolution and reduction on RuO<sub>2</sub>/TiO<sub>2</sub> electrodes*. Electrochimica Acta, 1979. **24**(5): p. 521-527.
56. Harrison, J.A., D.L. Caldwell, and R.E. White, *Electrocatalysis and the chlorine evolution reaction*. Electrochimica Acta, 1983. **28**(11): p. 1561-1568.
57. Harrison, J.A., D.L. Caldwell, and R.E. White, *Electrocatalysis and the chlorine evolution reaction - II. Comparison of anode materials*. Electrochimica Acta, 1984. **29**(2): p. 203-209.
58. Krishtalik, L.I., *Kinetics and mechanism of anodic chlorine and oxygen evolution reactions on transition metal oxide electrodes*. Electrochimica Acta, 1981. **26**(3): p. 329-337.

59. Fernández, J.L., M.R. Gennero de Chialvo, and A.C. Chialvo, *Kinetic study of the chlorine electrode reaction on Ti/RuO<sub>2</sub> through the polarisation resistance: Part I: experimental results and analysis of the pH effects*. *Electrochimica Acta*, 2002. **47**(7): p. 1129-1136.
60. Fernandez, J.L., M.R.G. de Chialvo, and A.C. Chialvo, *Kinetic study of the chlorine electrode reaction on Ti/RuO<sub>2</sub> through the polarisation resistance Part III: proposal of a reaction mechanism*. *Electrochimica Acta*, 2002. **47**(7): p. 1145-1152.
61. Comninellis, C. and G.P. Vercesi, *Characterization of DSA-type oxygen evolving electrodes: choice of a coating*. *Journal of Applied Electrochemistry*, 1991. **21**(4): p. 335-345.
62. Hoseinieh, S.M. and F. Ashrafizadeh, *Influence of electrolyte composition on deactivation mechanism of a Ti/Ru<sub>0.25</sub>Ir<sub>0.25</sub>Ti<sub>0.5</sub>O<sub>2</sub> electrode*. *Ionics*, 2013. **19**(1): p. 113-125.
63. Vallet, C.E., et al., *Rutherford Backscattering Spectroscopic Study of the Failure Mechanism of (RuO<sub>2</sub> + TiO<sub>2</sub>) / Ti Thin Film Electrodes in H<sub>2</sub>SO<sub>4</sub> Solutions*. *Journal of The Electrochemical Society*, 1997. **144**(4): p. 1289-1295.
64. Alves, V.A., L.A.d. Silva, and J.F.C. Boodts, *Surface characterisation of IrO<sub>2</sub>/TiO<sub>2</sub>/CeO<sub>2</sub> oxide electrodes and Faradaic impedance investigation of the oxygen evolution reaction from alkaline solution*. *Electrochimica Acta*, 1998. **44**(8-9): p. 1525-1534.
65. Loučka, T., *The reason for the loss of activity of titanium anodes coated with a layer of RuO<sub>2</sub> and TiO<sub>2</sub>*. *Journal of Applied Electrochemistry*, 1977. **7**(3): p. 211-214.
66. Hine, F., et al., *Electrochemical behavior of the oxide-coated metal anodes*. *Journal of the Electrochemical Society*, 1979. **126**(9): p. 1439-1445.
67. Loucka, T., *The reasons for the loss of activity of titanium-ruthenium dioxide anodes in sulphuric acid media*. *Journal of Applied Electrochemistry*, 1981. **11**(2): p. 143-144.
68. Iwakura, C., et al., *The anodic evolution of oxygen and chlorine on foreign metal-doped SnO<sub>2</sub> film electrodes*. *Electrochimica Acta*, 1981. **26**(4): p. 579-584.
69. Pilla, A.S., et al., *Evaluation of anode deactivation in chlor-alkali cells*. *Journal of Applied Electrochemistry*, 1997. **27**(11): p. 1283-1289.
70. Alves, V.A., L.A.d. Silva, and J.F.C. Boodts, *Electrochemical impedance spectroscopic study of dimensionally stable anode corrosion*. *Journal of Applied Electrochemistry*, 1998. **28**(9): p. 899-905.
71. Panić, V.V., et al., *The influence of the aging time of RuO<sub>2</sub> and TiO<sub>2</sub> sols on the electrochemical properties and behavior for the chlorine evolution reaction of activated titanium anodes obtained by the sol-gel procedure*. *Electrochimica Acta*, 2000. **46**(2-3): p. 415-421.
72. Xu, L.K. and J.D. Scantlebury, *A study on the deactivation of an IrO<sub>2</sub> -Ta<sub>2</sub>O<sub>5</sub> coated titanium anode*. *Corrosion Science*, 2003. **45**(12): p. 2729-2740.
73. Ribeiro, J. and A.R. De Andrade, *Characterization of RuO<sub>2</sub> Ta<sub>2</sub>O<sub>5</sub> Coated Titanium Electrode: Microstructure, Morphology, and Electrochemical Investigation*. *Journal of The Electrochemical Society*, 2004. **151**(10): p. D106-D112.

74. Panić, V., et al., *On the deactivation mechanism of RuO<sub>2</sub>-TiO<sub>2</sub>/Ti anodes prepared by the sol-gel procedure*. Journal of Electroanalytical Chemistry, 2005. **579**(1): p. 67-76.
75. Ribeiro, J. and A.R. de Andrade, *Investigation of the electrical properties, charging process, and passivation of RuO<sub>2</sub>-Ta<sub>2</sub>O<sub>5</sub> oxide films*. Journal of Electroanalytical Chemistry, 2006. **592**(2): p. 153-162.
76. Profeti, D., T.A.F. Lassali, and P. Olivi, *Preparation of Ir<sub>0.3</sub>Sn<sub>(0.7-x)</sub>Ti<sub>x</sub>O<sub>2</sub> electrodes by the polymeric precursor method: Characterization and lifetime study*. Journal of Applied Electrochemistry, 2006. **36**(8): p. 883-888.
77. Fathollahi, F., et al., *Comparison of morphology, stability and electrocatalytic properties of Ru<sub>0.3</sub>Ti<sub>0.7</sub>O<sub>2</sub> and Ru<sub>0.3</sub>Ti<sub>0.4</sub>Ir<sub>0.3</sub>O<sub>2</sub> coated titanium anodes*. Russian Journal of Electrochemistry, 2011. **47**(11): p. 1281-1286.
78. Chen, S., et al., *Ti/RuO<sub>2</sub>-Sb<sub>2</sub>O<sub>5</sub>-SnO<sub>2</sub> electrodes for chlorine evolution from seawater*. Chemical Engineering Journal, 2011. **172**(1): p. 47-51.

## 2 Electrochemical and surface characterization techniques

### 2.1 Electrochemical impedance spectroscopy

Electrochemical impedance spectroscopy (EIS) is a powerful electrochemical characterization technique which provides information on the electrochemical phenomena occurring at electrode-electrolyte interfaces. The great contribution of EIS to the electrochemical research is its ability to resolve phenomena occurring at different time scales [1].

The impedance is a property of a system to oppose to the electric current flux. This opposition can be modelled as an electrical equivalent circuit (EEC) of resistors, capacitors and inductors [1, 2]. However, since different EEC can exhibit the same impedance, previous knowledge of the system is required [1].

#### 2.1.1. Impedance fundamentals [1]

For assessing the impedance of a system at equilibrium a small AC perturbation is superimposed. This perturbation, a sinusoidal potential, typically 5 mV or 10 mV, should originate a pseudo-linear response. The current response will be a sinusoid at the same frequency but shifted in phase.

For a sinusoidal AC perturbation on potential,  $E_t$ :

$$E_p = E_0 \sin(\omega t) \quad (2.1)$$

where  $E_0$  is the magnitude of the perturbation,  $t$  is the time,  $\omega$  is the angular frequency (in  $\text{rad s}^{-1}$ ),  $\omega = 2\pi f$ , and  $f$  is the frequency in Hz. The response in current is given by:

$$i_p = i_0 \sin(\omega t - \phi) \quad (2.2)$$

where  $i_0$  is the magnitude of the current response and  $\phi$  is the phase shift. Assuming local linearity, the impedance,  $Z$ , is given by:

$$Z = \frac{E_p}{i_p} = \frac{E_0 \sin(\omega t)}{i_0 \sin(\omega t - \phi)} = Z_0 \frac{\sin(\omega t)}{\sin(\omega t - \phi)} \quad (2.3)$$

Using complex notation, Equation 2.3 can be expressed as Equation 2.4.

$$Z = \frac{E_0 e^{j\omega t}}{i_0 e^{j(\omega t - \phi)}} = Z_0 e^{j\phi} = Z_0 [\cos(\phi) + j\sin(\phi)] \quad (2.4)$$

The impedance is expressed in terms of two parameters, the magnitude,  $Z_0$ , and phase shift,  $\phi$ ;  $j$  is the imaginary number ( $j^2 = -1$ );

From Equation 2.4, the real component of impedance,  $Z' = Z_0 \cos(\phi)$ , and the imaginary component,  $Z'' = Z_0 \sin(\phi)$ , are easily calculated.

### 2.1.2. Impedance of electrochemical processes

The analysis of the impedance spectra requires the accurate fitting of the spectrum to electrical equivalent circuit. A suitable model provides relevant information about reaction kinetics, mass transfer, adsorption processes, double layer and ohmic resistance. Hereafter, a brief description of the main phenomena presented in electrochemical systems and the correspondence to EEC elements will be done.

**Ohmic resistance** – This comprises the impedance caused by the hardware (cables, connectors), the ohmic resistance of the electrolyte between the working electrode and the reference electrode. The ohmic resistance has no phase shift; it is easily read in the Nyquist plot since it corresponds to the value of the intersection of the impedance spectrum with the abscissa axis. The equivalent electric circuit element representing the ohmic resistance is a resistor and its impedance is equal to  $R_\Omega$ .

**Double layer capacitance** – An electric double layer arises at the electrode-electrolyte interfacial region. It is formed by the accumulation of ions and other charged species from the electrolyte at the electrode surface of opposite charge [2]. Between the electrodes and the first layers of species there is a nanometric gap where a potential drop is created. The potential difference, which permits charge separation, establishes a capacitor. Thus, the impedance of the double layer,  $Z_{dl}$ , is equivalent to the capacitor impedance:

$$Z_{dl} = \frac{1}{j\omega C_{dl}} \quad (2.5)$$

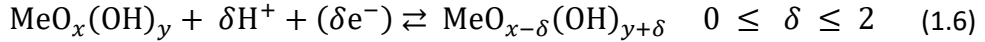
where  $C_{dl}$  is the double layer capacitance.

Regarding aqueous solutions, the double layer capacitance is typically detected in frequency range 10-1000 Hz [2]. The capacitance of the double layer depends on the electrode properties, operating conditions and molecular and intermolecular structure of the charged species and of on the solvent. The typical magnitude of the capacitance of the double layer is in the tens of  $\mu\text{F}/\text{cm}^2$  range [1, 2]. However, DSA<sup>®</sup> anodes typically exhibit values of capacitance in the range of  $\text{mF}/\text{cm}^2$  [3-5]. Lassali and co-authors assigned such high values to the porosity and roughness of these oxide electrodes due to the incomplete decomposition of the coating precursors [6]. These properties, porosity and roughness, lead to a non-uniform current distribution over the electrode surface which makes the double layer capacitance diverge from an ideal capacitor [1, 3, 7]. In this case, an artificial element, the constant phase element, CPE, can be used to substitute the capacitor [2]. The capacitance of the CPE is defined as:

$$Z_{CPE} = \frac{1}{j\omega Y_0^n} \quad (2.6)$$

where  $Y_0$  is the magnitude of the CPE and its units depend on the value of  $n$ .  $n$  is a function of the phase shift  $\phi$ ,  $n = \phi / (\pi/2)$ ; For the particular case of  $n= 1$ , the CPE is an ideal capacitor.

**Pseudocapacitance** – The pseudocapacitance is a process of Faradaic nature and it is related to the adsorption of species at the electrode surface that causes surface charging [2]. On metal oxides, like iridium or ruthenium oxides, which exhibit several oxidation states, the pseudocapacitance arises from oxidation/reduction associated with the bi-directional proton transfer between oxide and solution [2]. For ruthenium and iridium oxides, these phenomena occur in the potential range between the hydrogen and oxygen evolution reaction potential (0 V to 1.20 V vs NHE) and are described by Equation 1.6.



where Me is the metal. Besides, pseudocapacitance can arise at higher potentials due to the adsorption of intermediates such as for the chlorine evolution reaction (CIER) [8]. The pseudocapacitance is faradaic not capacitive, but its behaviour is well represented by a capacitor. Typical values for pseudocapacitance are in the range 700-800  $\mu\text{F}/\text{cm}^2$  [2]. The contribution of the pseudocapacitance is not always distinguishable from the double layer capacitance [2].

**Charge transfer resistance** – When the potential of an electrode is forced away from equilibrium, the electrode is polarized [1, 2]. In these circumstances, current flows due to electrochemical reactions at electrode surface. The current flux is controlled by both the kinetics of the electrochemical reactions and the diffusion of reactants and products. The charge transfer resistance,  $R_{\text{ct}}$ , relates the electrode potential with the current flowing through it. In the absence of concentration gradients, the Butler-Volmer equation (Equation 1.47) describes the relation between overpotential,  $\eta$ , and current density,  $j$ , and, implicitly, it is also related to the charge transfer resistance. For limit cases of overpotential lesser than 5 mV, Equation 1.48 applies:

$$|j| = j_0 \left( \frac{n\eta F}{RT} \right) \quad (2.7)$$

and rearranging:

$$\frac{\eta}{|j|} = \frac{RT}{nFj_0} = R_{\text{ct}} \quad (2.8)$$

Where  $n$  is the number of electrons transferred between each species,  $F$  is Faraday constant,  $R$  is the ideal gas constant,  $T$  is the absolute temperature in K and  $j_0$  is the exchange current density.

Dimensional analysis shows that the ratio  $\eta/j$  is consistent with resistance units. In the range of validity of the equation, the equation is linear and the charge transfer resistance is the slope of the curve  $\eta$  vs  $j$ .

Following a similar approach for higher positive potentials, Equation 2.9 is obtained from Equation 1.47.

$$\eta = \left( \frac{RT}{(1 - \alpha_c)nF} \right) \ln(j) - \left( \frac{RT}{(1 - \alpha_c)nF} \right) \ln(j_0) \quad (2.9)$$

where  $\alpha_c$  is the cathodic charge transfer coefficient.

In this case it is not possible to express the ratio  $\eta/j$ , but its derivative at a given value can be considered instead:

$$\frac{d\eta}{dj} = \left( \frac{RT}{(1 - \alpha_c)F} \right) \frac{1}{j} = R_{ct} \quad (2.10)$$

Equation 2.10 shows that, at higher potentials, the charge transfer resistance is not constant and decreases with the current.

**Mass transport impedance** – Diffusion mass transport is driven by concentration gradients between the bulk and the electrode surface. Concentration gradients are caused by reaction or adsorption processes at the electrode surface that cause the depletion of reactants/ adsorbing species and the excess of products near the electrode surface in relation to the bulk [2]. The impedance related to diffusion can be modeled by a Warburg circuit element. Considering semi-infinite diffusion limitations, the impedance of the Warburg,  $Z_w$ , element is given by Equation 2.11.

$$Z_w = \frac{\sigma_D}{\sqrt{\omega}} (1 - j) \quad (2.11)$$

where  $\sigma_D$  is the Warburg coefficient and is given by Equation 2.12.

$$\sigma_D = \frac{RT}{(n_i F)^2 A \sqrt{2}} \left( \frac{1}{[i]_\infty \sqrt{D_i}} \right) \quad (2.12)$$

$[i]_\infty$  is the bulk concentration of species  $i$ ,  $A$  is the surface area and  $D_i$  is the diffusion coefficient of species  $i$ . Equations 2.11 and 2.12 show the impedance of the Warburg coefficient decreases with the diffusion coefficient and bulk concentration.

If the reaction is fast, the charge transfer resistance will be small, and the impedance of the mass transport limitation will be predominant. In this case, Warburg impedance, a 45° degrees line, is visible over the whole range of frequency in a Nyquist diagram. For the opposite scenario, if the system is kinetically sluggish, then the impedance of mass transport will be negligible compared to the impedance of charge transfer and will be masked by the latter leading to a semicircle. For intermediate scenarios, two different regions of spectra are identifiable – the first at high frequencies corresponding to the region under kinetic control and the second, at low frequencies, in which the system is controlled by mass transport limitations. At high frequencies, the spectrum exhibits a semicircle associated with reaction impedance and at low frequencies the Nyquist spectra will show a diagonal line with slope 1.

### **2.1.3. Electrical equivalent circuits used to fit the impedance of DSA® anodes**

A literature survey of models used to represent the impedance of DSA® anodes has been carried out and presented in Tables 2.1 and 2.2. Table 2.1 shows the EEC used to fit the impedance of the DSA® in the region of potential in which chlorine/oxygen evolution occurs while Table 2.2 shows the EEC used to fit the impedance of DSA® in the capacitive region of the electrode. Despite of the diversity electrolytes and DSA® compositions found in literature, the impedance models used do not differ considerably between studies; ohmic resistance, double layer capacitance and charge transfer resistance, capacitance,  $C_f$ , and resistance,  $R_f$  of the coating are considered in most of the literature models.

Table 2.1 – Electrical equivalent circuits to fit the impedance of DSA® at potentials for OER or CIER

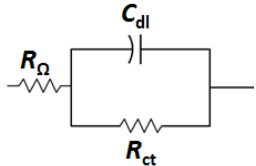
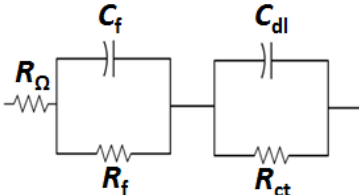
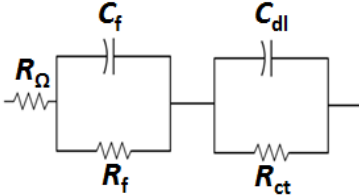
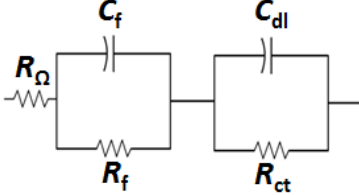
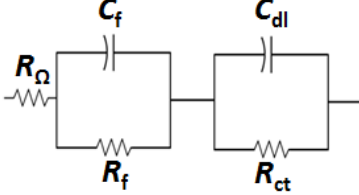
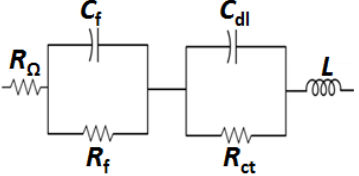
Reference	Year	DSA® composition	Electrolyte	$E$ vs NHE / V	EEC
[9]	1997	Ti/ TiO <sub>2</sub> -RuO <sub>2</sub>	0.5 M H <sub>2</sub> SO <sub>4</sub>	1.50	
[10]	1998	Ti/ (Ir <sub>0.3</sub> Ti <sub>(0.7-x)</sub> Ce <sub>x</sub> )O <sub>2</sub>	1.0 M KOH	1.50	
[5]	1998	Ti / ( Ir <sub>0.3</sub> -Ti <sub>0.7</sub> )O <sub>2</sub>	1.0 M HClO <sub>4</sub>	1.50	
[6]	1999	Ti/ (Ir <sub>0.3</sub> Ti <sub>(0.7-x)</sub> Sn <sub>x</sub> )O <sub>2</sub>	1.0 M HClO <sub>4</sub>	1.50	
[11]	2000	Ti/ (Ir <sub>0.3</sub> Ti <sub>0.7</sub> )O <sub>2</sub> Ti/ (Ir <sub>0.3</sub> Sn <sub>0.7</sub> )O <sub>2</sub>	0.5 M HClO <sub>4</sub>	1.475	
[12]	2002	Ti/ RuO <sub>2</sub> +Co <sub>3</sub> O <sub>4</sub>	0.5 M H <sub>2</sub> SO <sub>4</sub>	1.47	

Table 2.1 - Electrical equivalent circuits to fit the impedance of DSA® at potentials for OER or CIER (Continuation)

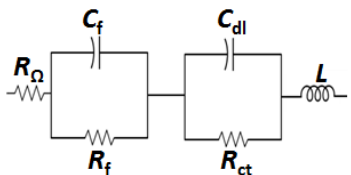
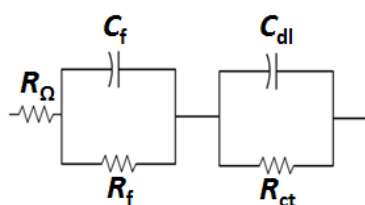
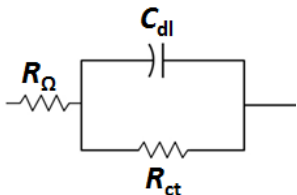
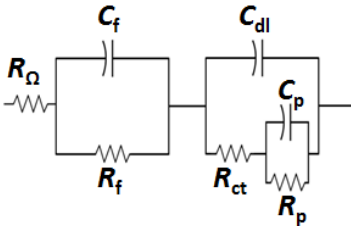
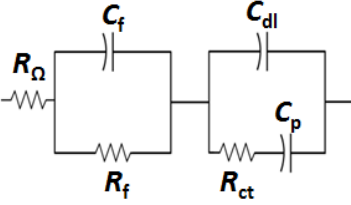
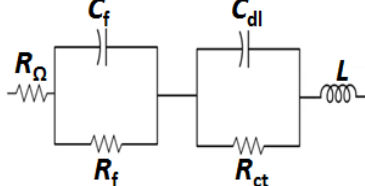
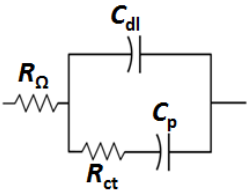
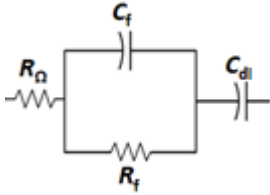
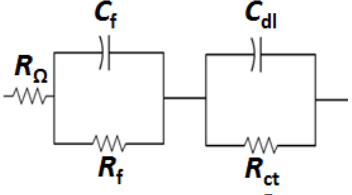
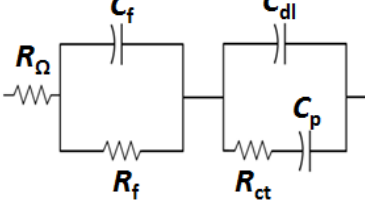
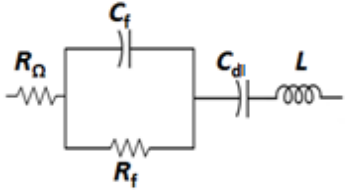
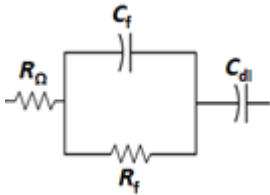
Reference	Year	DSA® composition	Electrolyte	<i>E</i> vs NHE / V	EEC
[13]	2002	Ti / IrO <sub>2</sub> -Ta <sub>2</sub> O <sub>5</sub>	0.5 M H <sub>2</sub> SO <sub>4</sub>	1.59	
[14]	2003	Ti / IrO <sub>2</sub> -Ta <sub>2</sub> O <sub>5</sub>	0.5 M Na <sub>2</sub> SO <sub>4</sub>	1.39	
[15]	2003	Ti/ RuO <sub>2</sub> -TiO <sub>2</sub>	1.0 M HClO <sub>4</sub>	1.49	
[16]	2004	Ti/ IrO <sub>2</sub> -Ta <sub>2</sub> O <sub>5</sub>	0.5 M H <sub>2</sub> SO <sub>4</sub>	1.50	
[17]	2006	Ti/ IrO <sub>2</sub> -Ta <sub>2</sub> O <sub>5</sub>	0.5 M H <sub>2</sub> SO <sub>4</sub>	1.5	
[18]	2006	Ti/ (Ru <sub>0.3</sub> Ti <sub>0.7</sub> )O <sub>2</sub>	0.5 M H <sub>2</sub> SO <sub>4</sub>	1.50	

Table 2.1 - Electrical equivalent circuits to fit the impedance of DSA® at potentials for OER or ClER  
(Continuation)

Reference	Year	DSA® composition	Electrolyte	<i>E</i> vs NHE / V	EEC
[4]	2010	Ti/RuO <sub>2</sub> -IrO <sub>2</sub> -TiO <sub>2</sub>	0.5 M NaCl, pH 2	1.49	
[3]	2013	Ti/RuO <sub>2</sub> -IrO <sub>2</sub> -TiO <sub>2</sub>	0.5 M NaCl, pH 2	1.49	
[3]	2013	Ti/RuO <sub>2</sub> -IrO <sub>2</sub> -TiO <sub>2</sub>	H <sub>2</sub> SO <sub>4</sub> 0.5 M	1.49	

Table 2.2 - Electrical equivalent circuits to fit the impedance of DSA® in the capacitive region of the electrode

Reference	Year	DSA® composition	Electrolyte	E vs NHE / V	EEC
[19]	1997	Ti / RuO <sub>2</sub> -TiO <sub>2</sub>	5.0 M NaCl, pH 2		
[10]	1998	Ti/ (Ir <sub>0.3</sub> Ti <sub>(0.7-x)</sub> Ce <sub>x</sub> )O <sub>2</sub>	1.0 M KOH	0.80	
[6]	1999	Ti/ (Ir <sub>0.3</sub> Ti <sub>(0.7-x)</sub> Sn <sub>x</sub> )O <sub>2</sub>	1.0 M HClO <sub>4</sub>	0.8	
[17]	2006	Ti/ IrO <sub>2</sub> -Ta <sub>2</sub> O <sub>5</sub>	0.5 M H <sub>2</sub> SO <sub>4</sub>	1.0	
[18]	2006	Ti/(Ru <sub>0.3</sub> Ti <sub>0.7</sub> )O <sub>2</sub>	0.5 M H <sub>2</sub> SO <sub>4</sub>	0.75	
[18]	2006	Ti/(Ru <sub>0.3</sub> Ti <sub>0.7</sub> )O <sub>2</sub>	0.5 M H <sub>2</sub> SO <sub>4</sub>	0.75	

In the electrical circuits above the capacitors can be replaced by CPEs; CPE are used due to the roughness and porosity of the DSA® coatings [3, 4, 13, 14].

In addition to the electric equivalent circuits shown above, several authors proposed more complex approaches. Panic et al. [7, 20, 21], Terezo et al. [22], Carvalho et al. [23] and Hoseinie and Ashrafizadeh [3] have used transmission line models of diverse orders to adjust the impedance of DSA® anodes. The transmission line model is a useful tool to adjust the impedance of porous electrodes; however, it can lead to a complexity and non-comprehensive correlation between the elements and the physical phenomena occurring at the electrode [24, 25].

## 2.2 Cyclic voltammetry [26, 27]

Cyclic voltammetry is a potentiodynamic electrochemical technique. In potentiodynamic techniques, the potential applied to the working electrode is changed while the current response is recorded. During cyclic voltammetry, the potential sweep rate is kept constant, although the direction of sweep is reverted when the potential attains the predetermined minimum and maximum potentials. The main parameters to set in a voltammetric measurement are the potential range and the sweep rate,  $\nu$ . The main phenomena revealed by cyclic voltammetry are the oxidation and the reduction of electroactive species in solution, adsorption/desorption phenomena and charging / discharging of the double layer.

The total current exhibited on voltamograms,  $i_t$ , results not only from the contribution of the faradaic processes,  $i_F$ , but also from the capacitive contribution of the charging of the double layer,  $i_C$ . This is shown in Equation 2.13.

$$i_t = i_C + i_F = C_{dl} \frac{dE}{dt} + i_F \quad (2.13)$$

with

$$\frac{dE}{dt} = \nu \quad (2.14)$$

The dependence of current on the sweep rate is partially shown in Equation 2.13, although the faradaic term is also related to the sweep rate. While the capacitive current is linearly sweep rate dependent, the faradaic current is proportional to the square root of sweep rate for electroactive species in solution [26, 28]. Thus, by increasing the sweep rate the term of the double layer charging contributes the most for the total current. In these cases, to accurately obtain the electrochemical reaction rate, the double layer charging current should be subtracted. This correction is particularly relevant when performing experiments with electrodes which present high double layer capacitances, as with the highly porous and rough DSA<sup>®</sup> electrodes [28].

Figure 2.1 presents a voltammogram obtained for a RuO<sub>2</sub>-IrO<sub>2</sub>-TiO<sub>2</sub> coating on a titanium substrate anode in 0.5 mol dm<sup>-3</sup> NaCl. The shape of the voltammogram is typical of an oxide coating applied by the thermodecomposition method. The voltammogram exhibits a broad anodic band between 0.4 and 1.0 V vs SCE (0.64 and 1.24 V vs NHE) rather than well-defined oxidation current peaks. This profile has been assigned to the existence of different oxidation states of iridium and ruthenium. Since most of the transitions between different states of the metals occur between the hydrogen and oxygen evolution potentials, the broad band is the result of the overlapping of current due to these metal transitions [29]. The oxidation and reduction of the metals is facilitated by the hydrous character of the DSA<sup>®</sup> anodes prepared by thermodecomposition. The water molecules in the coating promote the injection and ejection of protons to the electrode and make the internal areas of the coating to contribute to the voltammetric current [6, 30]. These pseudocapacitive currents are the main contribution to the total current observed in the voltammograms, although the double layer capacitance also has a relevant contribution [29].

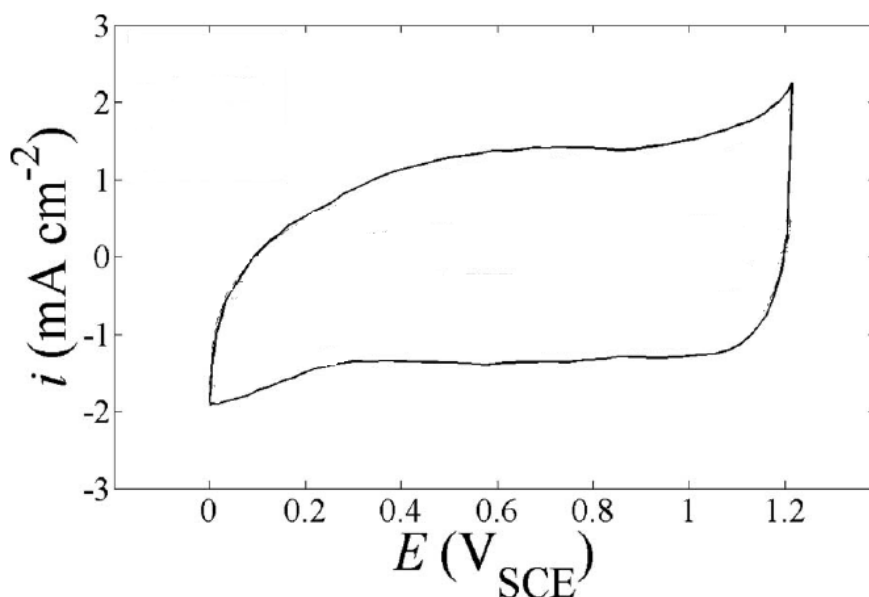


Figure 2.1 - Typical voltamogram of a Ti/ RuO<sub>2</sub>-IrO<sub>2</sub>-TiO<sub>2</sub> anode in 0.5 mol dm<sup>-3</sup> NaCl (adapted from [4])

### 2.3 X-ray photoelectron spectroscopy (XPS) [31]

X-ray photoelectron spectroscopy, also known as electron spectroscopy for chemical analysis (ESCA), is a technique for surface analysis since it provides information about both chemical composition and chemical structure of the materials. XPS is a non-destructive analytical tool that provides qualitative and semi quantitative information of all chemical elements except hydrogen and helium. Its success and broad range of application is confirmed by the huge number of published reports including XPS analysis. From the corrosion field [32-34] or catalysis [35, 36], to semiconductors [37, 38] and polymers [39, 40], XPS has been widely used because its flexibility, simple sample preparation and straightforward interpretation of results.

In XPS measurements the atomic layers under study are located at the surface (1 nm depth) and near surface region (up to 10 nm depth). These are the regions of the materials in which some important phenomena like catalysis, corrosion or passivation occur.

Figure 2.2 shows the XPS spectrum of pure ruthenium. The binding energies are unique and identify each element and the area of the peaks provides information about the relative composition of the element.

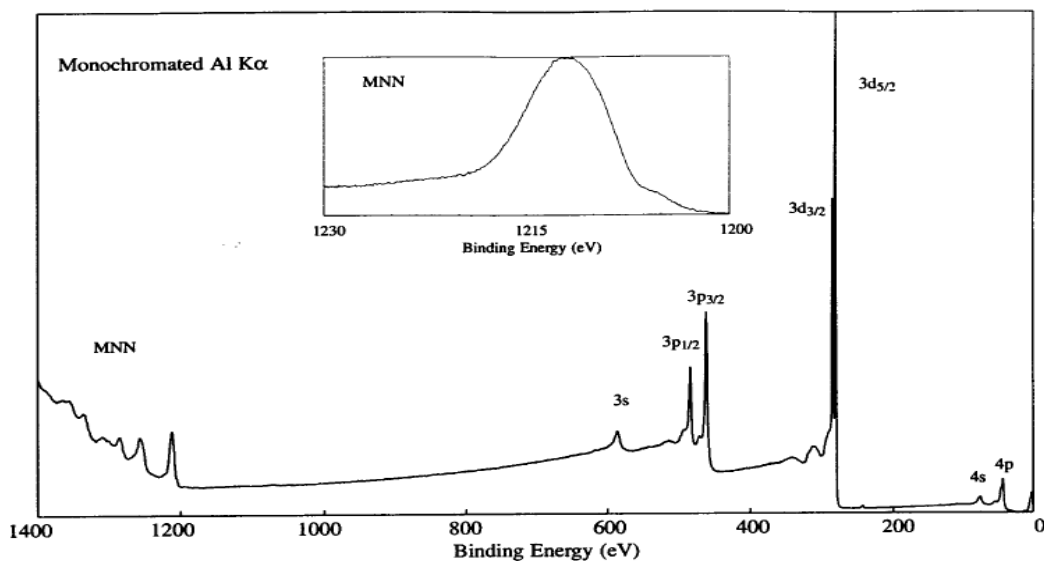
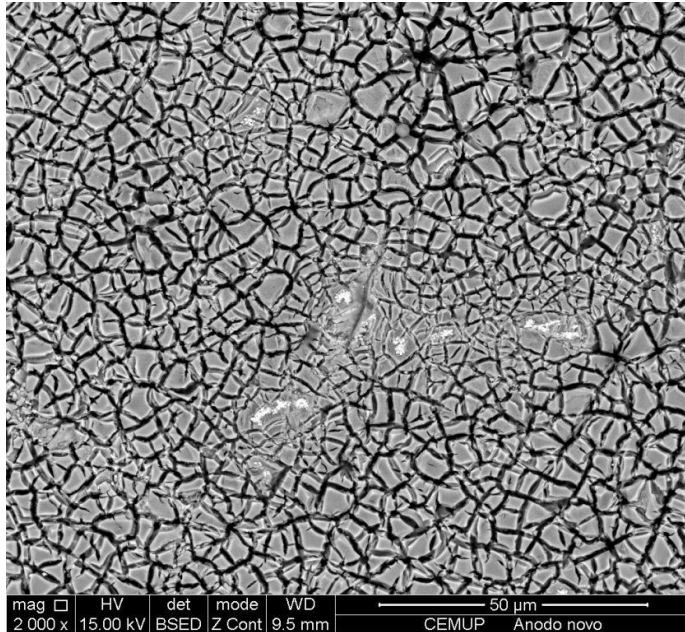


Figure 2.2 - XPS spectrum of ruthenium [41]

## 2.4 Scanning Electron Microscopy (SEM) [42]

Scanning electron microscopy (SEM) is a high resolution microscopic technique that provides information about the surface of materials with nanometric resolution and with large depth of field. This technique is the most used of the electron microscopy techniques for the characterization of DSA<sup>®</sup> anodes [4, 14]. Figure 2.3 shows the mud-crack structure of a DSA<sup>®</sup> anode obtained by SEM.



**Figure 2.3 - SEM images of DSA<sup>®</sup> anodes obtained in BSE mode with a 2000 X magnitude**

SEM images provide information about morphology, chemical composition and crystalline structure of the samples based on the emission of electrons from the excited sample.

Two types of electrons escape from a sample in a SEM experiment: backscattered electrons (BSE) and secondary electrons (SE). SE are less energetic (around 3-5 eV), and are released from the top layers of the sample (up to 50 nm). Therefore, SE provide information about the morphology and surface topography. Conversely, since BSE are high energy electrons, this type of electrons is able to escape from depths up to 300 nm. Since atoms of elements with higher atomic number tend to release more BSE, the images created are brighter than those with lower atomic number which are darker. Therefore, SEM images from samples containing diverse chemical elements will exhibit contrast and provides information of the distribution on those elements over the sample surface.

## **2.5 X-Ray Energy Dispersive Spectroscopy (EDS)[42, 43]**

X-ray spectroscopy is one of the most popular techniques that provides information about both chemical composition of the materials. The identification of the elements in the sample is based on the emission of X-rays from atoms excited by a higher energy X-Ray (typically from 10 keV to 30 keV). The region evaluated is located up to 10  $\mu\text{m}$  below the sample surface, although the exact depth depends on the beam energy, on the density of the sample and on the material.

EDS is a technique that provides not only qualitative, but also semi-quantitative analysis with accuracies up to 99 % for flat polished samples and if standards are available.

Usually, EDS devices are coupled to scanning or transmission electron microscopes in the form of a microanalyzer that allows evaluating the chemical composition in a microscopic area. Several authors that carried out ageing tests of DSA<sup>®</sup> anodes have used this technique to monitor the composition of the DSA<sup>®</sup> anodes during the test [3-5, 14].

## 2.6 References

1. Orazem, M.E. and B. Tribollet, *Electrochemical impedance spectroscopy*. The Electrochemical Society series. 2008, Hoboken, N.J.: Wiley. xxxi, 523 p.
2. Lvovich, V.F. and Wiley InterScience (Online service), *Impedance spectroscopy applications to electrochemical and dielectric phenomena*. 2012, Wiley,; Hoboken, N.J. p. 1 online resource (xiii, 353 p.).
3. Hoseinieh, S.M. and F. Ashrafizadeh, *Influence of electrolyte composition on deactivation mechanism of a Ti/Ru<sub>0.25</sub>Ir<sub>0.25</sub>Ti<sub>0.5</sub>O<sub>2</sub> electrode*. Ionics, 2013. **19**(1): p. 113-125.
4. Hoseinieh, S.M., F. Ashrafizadeh, and M.H. Maddahi, *A Comparative Investigation of the Corrosion Behavior of RuO<sub>2</sub>–IrO<sub>2</sub>–TiO<sub>2</sub> Coated Titanium Anodes in Chloride Solutions*. Journal of The Electrochemical Society, 2010. **157**(4): p. E50-E56.
5. Alves, V.A., L.A.d. Silva, and J.F.C. Boodts, *Electrochemical impedance spectroscopic study of dimensionally stable anode corrosion*. Journal of Applied Electrochemistry, 1998. **28**(9): p. 899-905.
6. Lassali, T.A.F., J.F.C. Boodts, and L.O.S. Bulhões, *Charging processes and electrocatalytic properties of IrO<sub>2</sub>/TiO<sub>2</sub>/SnO<sub>2</sub> oxide films investigated by in situ AC impedance measurements*. Electrochimica Acta, 1999. **44**(24): p. 4203-4216.
7. Panić, V.V., et al., *On the deactivation mechanism of RuO<sub>2</sub>-TiO<sub>2</sub>/Ti anodes prepared by the sol-gel procedure*. Journal of Electroanalytical Chemistry, 2005. **579**(1): p. 67-76.
8. Conway, B.E. and G. Ping, *Evaluation of Cl<sup>-</sup> adsorption in anodic Cl<sub>2</sub> evolution at Pt by means of impedance and potential-relaxation experiments. Influence of the state of surface oxidation of the Pt*. Journal of the Chemical Society, Faraday Transactions, 1991. **87**(17): p. 2705-2714.
9. Pilla, A.S., et al., *Evaluation of anode deactivation in chlor-alkali cells*. Journal of Applied Electrochemistry, 1997. **27**(11): p. 1283-1289.
10. Alves, V.A., L.A.d. Silva, and J.F.C. Boodts, *Surface characterisation of IrO<sub>2</sub>/TiO<sub>2</sub>/CeO<sub>2</sub> oxide electrodes and Faradaic impedance investigation of the oxygen evolution reaction from alkaline solution*. Electrochimica Acta, 1998. **44**(8-9): p. 1525-1534.
11. Lassali, T.A.F., J.F.C. Boodts, and L.O.S. Bulhões, *Faradaic impedance investigation of the deactivation mechanism of Ir-based ceramic oxides containing TiO<sub>2</sub> and SnO<sub>2</sub>*. Journal of Applied Electrochemistry, 2000. **30**(5): p. 625-634.
12. Silva, L.M.d., L.A.d. Faria, and J.F.C. Boodts, *Electrochemical impedance spectroscopic (EIS) investigation of the deactivation mechanism, surface and electrocatalytic properties of Ti/RuO<sub>2</sub>(x)+Co<sub>3</sub>O<sub>4</sub>(1-x) electrodes*. Journal of Electroanalytical Chemistry, 2002. **532**(1-2): p. 141-150.
13. Hu, J.M., et al., *Degradation mechanism of long service life Ti/IrO<sub>2</sub>-Ta<sub>2</sub>O<sub>5</sub> oxide anodes in sulphuric acid*. Corrosion Science, 2002. **44**(8): p. 1655-1668.
14. Xu, L.K. and J.D. Scantlebury, *A study on the deactivation of an IrO<sub>2</sub> -Ta<sub>2</sub>O<sub>5</sub> coated titanium anode*. Corrosion Science, 2003. **45**(12): p. 2729-2740.

15. Panić, V.V., et al., *The role of titanium oxide concentration profile of titanium oxide of RuO<sub>2</sub>-TiO<sub>2</sub> coatings obtained by the sol-gel procedure on its electrochemical behavior*. Vol. 68. 2003, Belgrade, SERBIE: Serbian Chemical Society. 10.
16. Hu, J.-M., J.-Q. Zhang, and C.-N. Cao, *Oxygen evolution reaction on IrO<sub>2</sub>-based DSA® type electrodes: kinetics analysis of Tafel lines and EIS*. International Journal of Hydrogen Energy, 2004. **29**(8): p. 791-797.
17. Ribeiro, J. and A.R. de Andrade, *Investigation of the electrical properties, charging process, and passivation of RuO<sub>2</sub>-Ta<sub>2</sub>O<sub>5</sub> oxide films*. Journal of Electroanalytical Chemistry, 2006. **592**(2): p. 153-162.
18. Malpass, G.R.P., R.S. Neves, and A.J. Motheo, *A comparative study of commercial and laboratory-made Ti/Ru<sub>0.3</sub>Ti<sub>0.7</sub>O<sub>2</sub> DSA® electrodes: "In situ" and "ex situ" surface characterisation and organic oxidation activity*. Electrochimica Acta, 2006. **52**(3): p. 936-944.
19. Vallet, C.E., et al., *Rutherford Backscattering Spectroscopic Study of the Failure Mechanism of (RuO<sub>2</sub> + TiO<sub>2</sub>) / Ti Thin Film Electrodes in H<sub>2</sub>SO<sub>4</sub> Solutions*. Journal of The Electrochemical Society, 1997. **144**(4): p. 1289-1295.
20. Panić, V.V., et al., *Capacitive properties of RuO<sub>2</sub>-coated titanium electrodes prepared by the alkoxide ink procedure*. Journal of Electroanalytical Chemistry, 2007. **609**(2): p. 120-128.
21. Panić, V.V., et al., *The effect of the addition of colloidal iridium oxide into sol-gel obtained titanium and ruthenium oxide coatings on titanium on their electrochemical properties*. Physical Chemistry Chemical Physics, 2010. **12**(27): p. 7521-7528.
22. Terezo, A.J., et al., *Separation of transport, charge storage and reaction processes of porous electrocatalytic IrO<sub>2</sub> and IrO<sub>2</sub>/Nb<sub>2</sub>O<sub>5</sub> electrodes*. Journal of Electroanalytical Chemistry, 2001. **508**(1-2): p. 59-69.
23. Carvalho, L.A.d., A.R.d. Andrade, and P.R. Bueno, *Espectroscopia de impedância eletroquímica aplicada ao estudo das reações heterogêneas em ânodos dimensionalmente estáveis*. Química Nova, 2006. **29**: p. 796-804.
24. Orazem, M.E., P. Agarwal, and L.H. Garcia-Rubio, *Critical issues associated with interpretation of impedance spectra*. Journal of Electroanalytical Chemistry, 1994. **378**(1): p. 51-62.
25. Doyle, M., J.P. Meyers, and J. Newman, *Computer Simulations of the Impedance Response of Lithium Rechargeable Batteries*. Journal of The Electrochemical Society, 2000. **147**(1): p. 99-110.
26. Brett, C.M.A. and A.M. Oliveira-Brett, *Electrochemistry : principles, methods, and applications*. 1993, Oxford ; New York: Oxford University Press.
27. Bard, A.J. and L.R. Faulkner, *Electrochemical methods : fundamentals and applications*. 2nd ed. 2001, New York: Wiley. xxi, 833 p.
28. Gileadi, E., *Electrode kinetics for chemists, chemical engineers, and materials scientists*. 1993, New York: VCH. xviii, 597 p.
29. Conway, B.E., *Electrochemical Supercapacitors: Scientific Fundamentals and Technological Applications*. 1999: Springer US.

30. Lokhande, C.D., D.P. Dubal, and O.-S. Joo, *Metal oxide thin film based supercapacitors*. Current Applied Physics, 2011. **11**(3): p. 255-270.
31. Vickerman, J.C. and I. Gilmore, *Surface Analysis: The Principal Techniques*. 2011: Wiley.
32. Outirite, M., et al., *AC impedance, X-ray photoelectron spectroscopy and density functional theory studies of 3,5-bis(n-pyridyl)-1,2,4-oxadiazoles as efficient corrosion inhibitors for carbon steel surface in hydrochloric acid solution*. Electrochimica Acta, 2010. **55**(5): p. 1670-1681.
33. Lebrini, M., et al., *Enhanced corrosion resistance of mild steel in normal sulfuric acid medium by 2,5-bis(n-thienyl)-1,3,4-thiadiazoles: Electrochemical, X-ray photoelectron spectroscopy and theoretical studies*. Applied Surface Science, 2007. **253**(23): p. 9267-9276.
34. Hammond, J.S., et al., *The application of X-ray photoelectron-spectroscopy to a study of interfacial composition in corrosion-induced paint de-adhesion*. Corrosion Science, 1981. **21**(3): p. 239-253.
35. Kallury, K.M.R., P.M. Macdonald, and M. Thompson, *Effect of surface-water and base catalysis on the silanization of silica by (aminopropyl)alkoxysilanes studied by X-ray photoelectron spectroscopy and <sup>13</sup>C cross-polarization/magic angle spinning nuclear magnetic resonance*. Langmuir, 1994. **10**(2): p. 492-499.
36. Duong, H.T., et al., *Oxygen reduction catalysis of the Pt<sub>3</sub>Co alloy in alkaline and acidic media studied by x-ray photoelectron Spectroscopy and electrochemical methods*. Journal of Physical Chemistry C, 2007. **111**(36): p. 13460-13465.
37. Perego, M. and G. Seguni, *Charging phenomena in dielectric/semiconductor heterostructures during x-ray photoelectron spectroscopy measurements*. Journal of Applied Physics, 2011. **110**(5): p. 11.
38. Nomura, K., et al., *Subgap states in transparent amorphous oxide semiconductor, In-Ga-Zn-O, observed by bulk sensitive x-ray photoelectron spectroscopy*. Applied Physics Letters, 2008. **92**(20): p. 3.
39. Thomas, H.R. and J.J. Omalley, *Surface studies on multicomponent polymer systems by X-ray photoelectron-spectroscopy - polystyrene - poly(ethylene oxide) diblock copolymers*. Macromolecules, 1979. **12**(2): p. 323-329.
40. Chan, H.S.O., et al., *Preparation and characterization of electrically conducting copolymers of aniline and anthranilic acid - evidence for self-doping by X-ray photoelectron-spectroscopy*. Macromolecules, 1992. **25**(22): p. 6029-6034.
41. Moulder, J.F. and J. Chastain, *Handbook of X-ray Photoelectron Spectroscopy: A Reference Book of Standard Spectra for Identification and Interpretation of XPS Data*. 1995: Physical Electronics.
42. Leng, Y., *Materials Characterization: Introduction to Microscopic and Spectroscopic Methods*. 2009: Wiley.
43. Goldstein, J., et al., *Scanning Electron Microscopy and X-ray Microanalysis: Third Edition*. 2012: Springer US.



### **3 Electrochemical cell design for impedance studies of chlorine evolution at DSA<sup>®</sup> anodes**

#### **3.1 Abstract**

A new electrochemical cell design suitable for electrochemical impedance spectroscopy (EIS) studies of chlorine evolution on dimensionally stable anodes (DSA<sup>®</sup>) has been developed. Despite being considered a powerful tool, EIS has rarely been used to study the kinetics of chlorine evolution at DSA<sup>®</sup> anodes. Cell designs in the open literature are unsuitable for EIS analysis at high DSA<sup>®</sup> anode current densities for chlorine evolution because they allow gas accumulation at the electrode surface. Using the new cell, impedance spectra of the DSA<sup>®</sup> anode during chlorine evolution at high sodium chloride concentration (5 mol dm<sup>-3</sup> NaCl) and high current densities (up to 140 mA cm<sup>-2</sup>) were recorded. Additionally, polarization curves and voltammograms were obtained showing little or no noise. EIS and polarization curves evidence the role of the adsorption step in the chlorine evolution reaction, compatible with the Volmer-Heyrovsky and Volmer-Tafel mechanisms.

## 3.2 Introduction

The chlor-alkali industry is one of the most important worldwide commodity industries and it underpins about 60 % of the chemical industry turnover [1]. Indeed, the broad range of uses of both sodium hydroxide and chlorine in industry (e.g. pharmaceutical or fertilizer industries) and for consumers as disinfectant or detergents place them among the top 10 chemicals [2]. The electrochemical route is almost the only one to produce chlorine and sodium hydroxide, representing more than 95 % of the chlorine and 99.5 % of the sodium hydroxide total worldwide production [2]. Three electrochemical cell technologies are well established for producing chlorine and sodium hydroxide – mercury, diaphragm and membrane cells [2, 3]. However, due to economic and environmental issues, mercury and diaphragm cells have been replaced and almost all new plants are equipped with membrane cells [3, 4]. In a membrane cell, the anode and the cathode compartments are separated by a cation exchange membrane. At the cathode, a nickel plate, hydrogen and hydroxide ions are produced by water reduction. At the anode, a DSA<sup>®</sup> (dimensionally stable anode), chloride is oxidized to chlorine. Sodium ions are transported through the cation exchange membrane from anode to cathode compartment. Water reduction and chloride oxidation are the main electrochemical reactions; however, undesired reactions also occur. The most critical undesired reaction occurs at the anode and consists in oxygen evolution via water oxidation. This reaction affects not only the purity of the products and the efficiency of the process, but is also responsible for the fast aging of the anode [2].

Several mechanisms have been proposed for chlorine evolution at DSA<sup>®</sup> anodes [2, 5, 6]. Often the mechanism proposed relies on electrochemical analysis, i.e. the Tafel slope, potential decay curves and cyclic voltammetry [7-10]; however, electrochemical impedance spectroscopy (EIS) has rarely been reported for this purpose. EIS has been employed in kinetic studies of chlorine evolution on platinum [11-13] but not on DSA<sup>®</sup> electrodes. It has been used to characterize DSA<sup>®</sup> anodes in low concentration chloride solutions [14-21] at low potentials, 1.25 V vs NHE to 1.38 V vs NHE [22, 23], which

corresponds to current densities up to  $10 \text{ mA cm}^{-2}$ . These conditions are far from those used industrially for producing chlorine, where the current densities reach  $400 \text{ mA cm}^{-2}$ .

EIS analysis is only possible if stable impedance spectra can be obtained and these depend on the cell design. Since EIS is so important for studying electrochemical systems, this article describes an electrochemical cell design suitable for operating at high current densities, in order to permit the study of chlorine evolution under typical industrial operating conditions.

The most common configuration of an electrochemical cell consists of three vertically-placed electrodes. Due to its flexibility, reduced cost and easy operation it is one of the most used cell designs in electrochemical experiments [24]. More complex cells have been used for specific purposes [25-30]. An extensive literature survey of electrochemical cell designs equipped with three electrodes is available in Zoski [31] and Kissinger *et al.* [24], which provide general guidelines about cell design. Due to the specificity of each investigation, most authors build their own cells, but do not describe the cell used [11, 14, 15, 21, 32].

Different cell designs have been made in order to accommodate specially-shaped electrodes [26] or to meet restrictions regarding electrode exposure to the electrolyte [33]. For instance, for testing electrodes for which only one face is allowed to contact the electrolyte, the rest is protected by a Teflon holder [23, 34] or by inert components such as epoxy resins [35]. An alternative approach is to machine a hole in one cell wall so that the electrode surface is flushed with the internal cell body wall. In this type of cell, only the front face of the electrode is accessible to electrolyte; it must be ensured that the electrode is sufficiently tightly fitting to prevent infiltration of solution between the electrode and cell body. This type of cell has been used in previous work for studying gas evolution reactions [36]. An additional advantage of this design is the easy electrical connection to the working electrode, on the back face of the DSA<sup>®</sup>. In this way no other metal can contact the electrolyte, which avoids the occurrence of side reactions.

Torcheux *et al.*[33] report a similar cell configuration but with an O-ring placed between the electrode surface and the back of the cell wall. The O-ring seals the electrode

surroundings, although it creates a gap between the electrode surface and the wall surface. In this design, gas bubbles can accumulate over the electrode. The formation of bubbles at gas-evolving electrodes has already been indicated as a critical point in mechanistic studies [37]. The bubbles have sometimes been associated with positive effects due to improvement of mass transfer [38], but more often have been identified as an inconvenience since bubbles create additional ohmic resistance and blockage of the electrode surface [23]. Moreover, the accumulation of gases on the electrode, which can vary as a function of time, makes the current fluctuate and EIS analysis impossible to perform [39, 40].

A horizontal orientation with the electrode facing upwards facilitates bubble rise through the electrolyte solution and avoids bubble coalescence at the electrode surface. The horizontal orientation has been demonstrated to improve the mass transfer of hydrogen and oxygen produced electrochemically [38, 41]. Despite not being the standard approach, a horizontal orientation with the electrode facing upwards was already used by previous authors, such as Ovarfort [42], Bertagna *et al.*[43] Hendricks *et al.*[44] and Wozniak *et al.* [26] for studying other electrode processes. Ovarfort [42] describes the Avesta electrochemical cell for pitting corrosion tests; this cell, suited for low current density experiments, was a landmark in the corrosion field. To our knowledge, studies regarding chlorine mass transfer in this configuration have not yet been carried out.

Using the horizontal orientation, an O-ring can seal the electrode/cell body junction without interfering with gas release, and is also an effective tool to define the electrode area, as reported by Wozniak *et al.* [26]. In order to prevent infiltration, the electrode plus O-ring must be pressed onto the underside of the cell. Some authors accomplish this by tightening screws with bolts or screw directly into the cell body [43-45]. More complex pressing systems were used by Bowler *et al.* [46] and Wozniak *et al.* [26]: while the former used a spring, the latter used two half-turn thumbscrews. In the present work, the effectiveness of the liquid sealing is ensured by a single large Plexiglas® screw thread.

Previous designs were shown not to be reliable to study chlorine evolution on DSA® anodes because they either do not prevent infiltration or do not permit electrochemical

characterization of the electrode. To meet both requirements, a new cell with the electrode placed at the bottom together with mechanical stirring of the electrolyte solution was designed. Mechanical stirring was shown to be the only approach that ensures the homogeneity of the electrolyte solution and creates enough shear strength to remove the evolved gas bubbles and allow reaction over the whole electrode surface. In these conditions, accurate electrochemical characterization was achieved.

Although the electrode configuration used in industrial electrochemical plants is different, the convection and the operating current range of the new cell make it a useful approach to mimic the industrial process and obtain mechanistic information. The synergetic effect of electrode orientation and vertical stirring permit electrochemical impedance measurements at 60 °C using a 5 mol dm<sup>-3</sup> NaCl aqueous solution, even at current densities as high as 150 mA cm<sup>-2</sup>. These values are close to the industrial current range which is around 300 – 400 mA cm<sup>-2</sup> [2].

The good performance of this new cell was verified by recording polarization curves, cyclic voltammetry and electrochemical impedance spectroscopy.

### 3.3 Cell design

The designed electrochemical cell is shown in Figure 3.1 and consists of a 400 ml jacketed cylindrical cell made of Plexiglas® with a Plexiglas® lid. Heated water from a water circulation bath is pumped through the jacket to control the temperature of the electrolyte solution in the cell. A 16 mm diameter hole was drilled through the cell bottom to give access to the working electrode (DSA® anode), which was placed 2 mm below the bottom of the main compartment inside a cylindrical cavity of 20 mm diameter and 5 mm depth. The working electrode is a round plate of 20 mm diameter and 3 mm thickness sealed to the cell with a 16 mm internal diameter and 2 mm thick Viton O-ring. A 20 mm copper collector disk welded to a copper wire was pressed onto the electrode back surface to ensure good electrical connection to the DSA® electrode. The sealing of the electrode with O-ring plus copper disk is ensured by pressing it into the cell body with a single large

Plexiglas® screw. Besides the ability to change the electrode quickly and easily, the adjustable screw allows accommodating electrodes of different thicknesses.

**a**



**b**

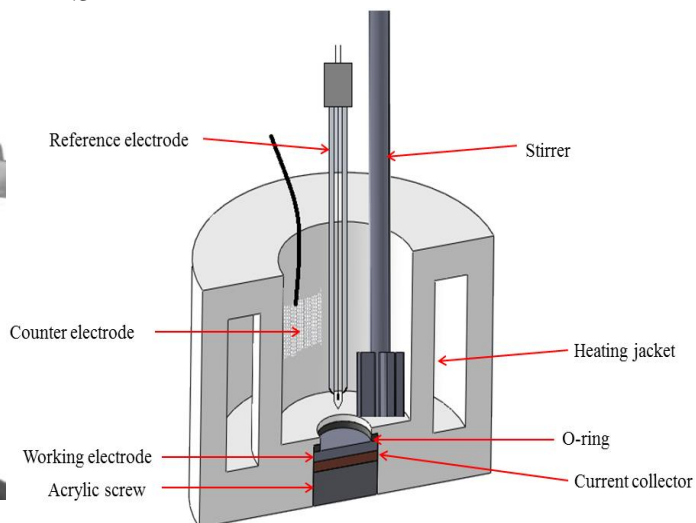


**Figure 3.1 - The new electrochemical cell. a – Photo; b – Schematic cross section.**

Homogenization of the electrolyte and cleaning of the bubbles formed on the electrode surface, in order to guarantee a stable electrochemical behavior, are accomplished using a mechanical stirrer.

The cell lid is 10 mm thick and is drilled in order to accommodate the shaft of the mechanical stirrer, the counter electrode, the reference electrode and a thermometer. An extra hole was made that allows sparging an inert gas in the electrolyte. The reference electrode is placed at the centre of the lid in order to be aligned with the working electrode at the bottom of the cell. The counter electrode, a platinum mesh plus platinum wire connector, is placed vertically at the mid-point between the reference electrode and the cell wall. The counter electrode external connection to the potentiostat was done using a gold-coated crocodile clip in order to be more resistant to chlorine corrosion. A PVC stirrer, which is compatible with the solution of sodium chloride and chlorine, was fabricated to ensure adequate stirring of the cell electrolyte solution. The stirrer position

was carefully chosen to enhance the gas bubble rising with minimum impact on the electrochemical measurements.

The body of the cell includes two side accesses designed to continuously feed electrolyte if desired. The access heights were carefully chosen in order to control the electrolyte level inside the cell.

## **3.4 Experimental**

### **3.4.1 Reagents**

Sodium chloride solutions were prepared from 5 mol dm<sup>-3</sup> NaCl solutions. The initial pH was set to 2 using industrial grade HCl 33 wt. %. Both solutions were supplied by CUF-QI (Portugal). When necessary, the initial solution was diluted using deionised water (Millipore, resistivity  $\geq 18$  M $\Omega$  cm).

### **3.4.2 Electrodes**

The working electrode was part of a DSA<sup>®</sup> anode made of titanium coated with RuO<sub>2</sub>-IrO<sub>2</sub>-TiO<sub>2</sub> supplied by Electrocell. The exposed area was 2.0 cm<sup>2</sup>. A platinum mesh was used as counter electrode. An Ag/AgCl electrode saturated with KCl was used as reference electrode.

### **3.4.3 Electrochemical measurements**

Polarization curves, cyclic voltammetry and electrochemical impedance spectroscopy (EIS) measurements were performed to characterize the cell. Polarization curves and cyclic voltammograms were recorded using a Gamry 600 potentiostat.

Cyclic voltammetry experiments were run at 20 °C, between +0.2 V vs NHE to +1.4 V vs NHE, covering the capacitive / pseudocapacitive region of the electrode as well the beginning of the chlorine / oxygen evolution region. Ten potential cycles were performed at a scan rate of 50 mV s<sup>-1</sup>.

Three replicas of each polarization curve were recorded at 1 mV s<sup>-1</sup> scan rate in the potential range between 1.2 V and 1.6 V vs NHE, at 60 °C and 80 °C. The contribution of

ohmic resistance, obtained from analysis of the impedance spectra, was subtracted from the polarization curves.

EIS measurements were performed using a PC-controlled Solartron 1250 Frequency Analyzer, coupled to a Solartron 1286 Electrochemical Interface controlled by ZPlot 2.4 software. The impedance spectra were obtained in potentiostatic mode with a 10 mV rms amplitude perturbation in the frequency range from 65 kHz to 1 Hz, 10 data points per frequency decade, with Auto-Integration set as Long and a maximum integration time of 100 s. Two replicas of each impedance spectrum were recorded at 1.40 V, 1.45 V, 1.50 V, 1.55 V and 1.60 V vs NHE at 60 °C. These potentials are in the oxygen and chlorine evolution potential region.

The solution in the cell was stirred at 500 rpm during polarization curve recording and EIS measurements. pH measurements were made with a CRISON 2001 micro pH-meter. Experiments were carried out in the temperature range of 20 °C – 80 °C ± 2 °C. The temperature in the cell was controlled using a HUBER CC1 water circulation bath.

## **3.5 Results**

### **3.5.1 Effect of stirring**

A first set of experiments was carried out to assess the performance of the new electrochemical cell for studying chlorine evolution. Without stirring, accumulation and coalescence of bubbles on the anode surface take place. These phenomena are illustrated in Figure 3.2a. Conversely, Figure 3.2b shows an electrode surface free of gas bubbles. This was achieved by using a mechanical stirrer at 500 rpm. The corresponding impedance spectra are shown in Figure 3.3; the plots join consecutive points to illustrate the sequence of acquired data.

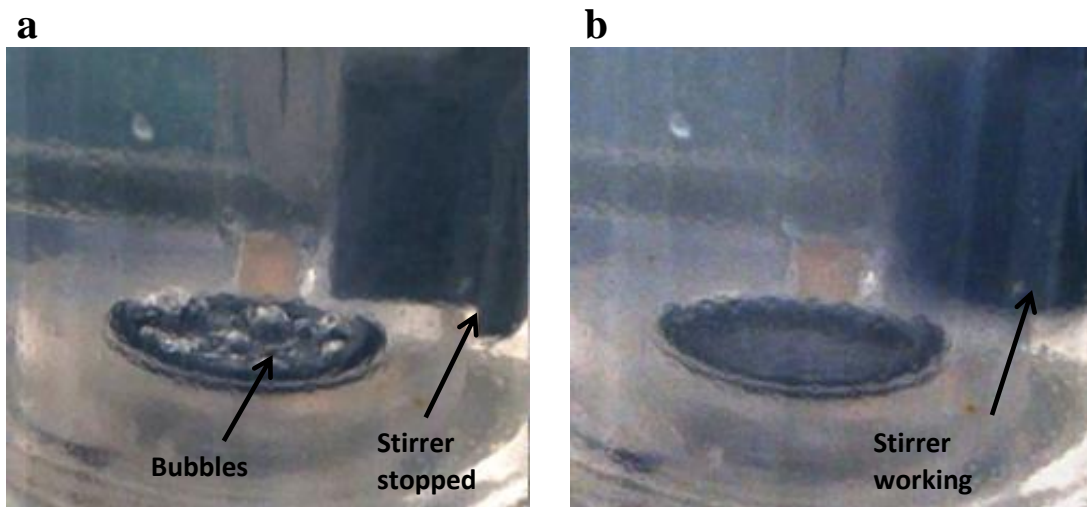


Figure 3.2 - Detail of the anode surface during chlorine evolution at 1.50 V vs NHE in 5 mol dm<sup>-3</sup> NaCl, pH 2,  $T = 60\text{ }^{\circ}\text{C}$ ; a - no stirring; b - electrolyte stirred at 500 rpm. Legend was added to highlight the stirring effect.

Figure 3.3a illustrates the random changes in the impedance values in the spectrum related to the formation and release of bubbles from the electrode, when there is no stirring. A bubble on the electrode surface decreases the available active area for ionic transport and thence the measured interfacial resistance, and the presence of a reaction product adjacent to the electrode makes the oxidation overpotential increase. In the present case, when a bubble is released a marked change in the impedance signal is seen due to the increase in electrode area and consequent lower impedance value; in Figure 3.3a the instants preceding bubble release can be identified. Similar fluctuations are often observed in spectra recorded in the potential range in which the chlorine evolution reaction occurs and are more common at higher current densities. As soon as the stirrer was switched on, the fluctuations in impedance stopped, as illustrated in Figure 3.3b. This spectrum clearly illustrates the benefit of this new cell design.

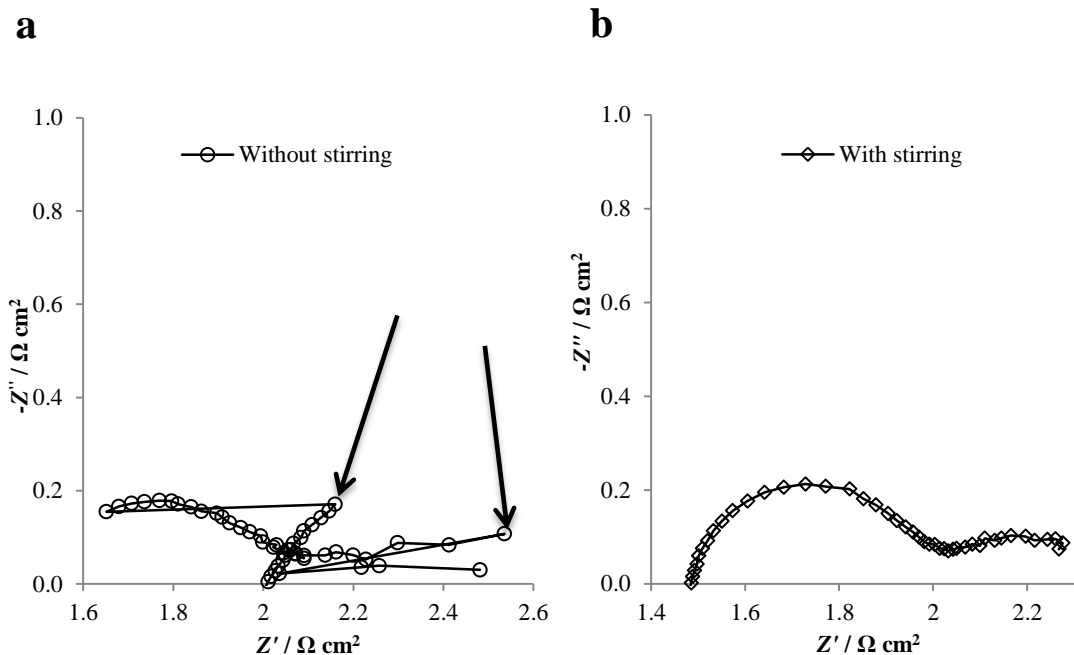
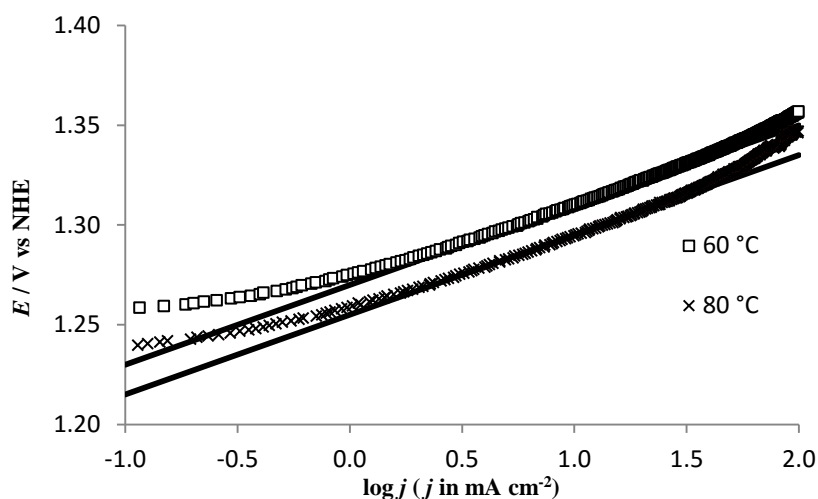


Figure 3.3 - Effect of stirring on complex plane impedance spectra of DSA® anode at 1.50 V vs NHE in 5 mol dm<sup>-3</sup> NaCl, pH 2 at 60 °C. a - no stirring; b - electrolyte stirred at 500 rpm. Arrows identify the points preceding the bubble release.

### 3.5.2 Polarization curves

Polarization curves were recorded at 60 °C and 80 °C as described in the experimental section. The working electrode potential was plotted against the logarithm of the current density. Figure 3.4 shows polarization curves at both temperatures, as well as two reference lines representing the 40 mV decade<sup>-1</sup> slope. The potential range depicted was chosen to include only positive, anodic currents within and close to the Tafel region. The potentials were corrected for ohmic resistance obtained from EIS analysis: 1.56 Ω cm<sup>2</sup> at 60 °C and 1.26 Ω cm<sup>2</sup> at 80 °C. Thus, the potential range presented in Figure 3.4 corresponds to the original potential range (1.2 to 1.6 V vs NHE) corrected for the potential corresponding to the ohmic contribution.



**Figure 3.4 - Polarization curves for DSA® anode in 5 mol dm<sup>-3</sup> NaCl, pH 2 at 60 °C and 80 °C; scan rate 1 mV s<sup>-1</sup> in the positive direction.**

The anodic polarization curves shown in Figure 3.4 agree with previous work by other authors [8, 47]. Three distinct zones are identified in these curves. The first zone is from low potentials up to ca. 1.27 V vs NHE; the second zone is from 1.27 up to 1.34 V vs NHE; the last is from 1.34 vs NHE upwards. The first region corresponds to potentials where both anodic and cathodic reactions occur. In the second zone, cathodic currents become negligible and the potential vs logarithmic current density can be described by the Tafel equation. In the third zone the overpotential no longer follows Tafel behavior; its shape suggests a Volmer-Tafel mechanism with recombination (Tafel) as rate-determining step [13].

The Tafel slopes found in the intermediate region,  $43.1 \pm 0.6$  mV decade<sup>-1</sup> at 60 °C and  $40.8 \pm 0.8$  mV decade<sup>-1</sup> at 80 °C, are similar to those reported in the literature, ca. 40 mV decade<sup>-1</sup> in the temperature range 25-90 °C [7, 23, 48]. These values are in agreement with the Volmer-Heyrovsky mechanism considering electrochemical desorption of chlorine as the rate-limiting step [7, 23, 48]. From this mechanism, the charge transfer coefficients,  $\alpha$ , were found to be 0.54 at 60 °C and 0.71 at 80 °C. These values are between 0.5 and 1.0, which have been reported in the literature as the limiting cases of a symmetric

oxidation-reduction activation barrier and a barrierless or quasibarrierless reaction, respectively [8, 9].

### 3.5.3 Cyclic voltammetry

Figure 3.5a shows cyclic voltammograms obtained at different scan rates in 0.5 mol dm<sup>-3</sup> NaCl. The voltammograms present the typical shape seen in previous reports concerning the study of titanium plates coated with the ternary oxide – IrO<sub>2</sub>-TiO<sub>2</sub>-RuO<sub>2</sub> [20, 21, 49].

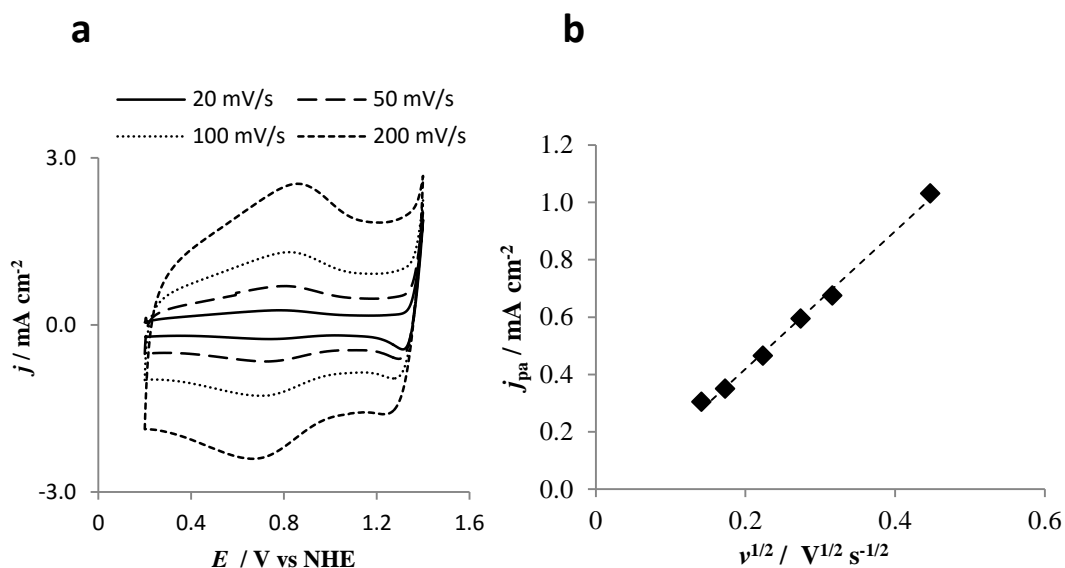
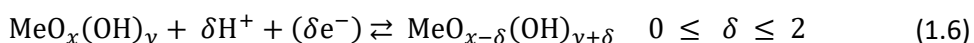


Figure 3.5 a - Cyclic voltammograms of DSA® anode as a function of scan rate in 0.5 mol dm<sup>-3</sup> NaCl, pH 2 at 20 °C. b - Plot of anodic peak current density,  $j_{pa}$ , vs. scan rate.

The current density behaviour observed in the cyclic voltammograms results from the contribution of the capacitive current associated with the double layer, as well as the pseudocapacitance related to redox transitions of the iridium and ruthenium oxides present in the oxide coating [17, 18]. Pseudocapacitive currents are seen in the potential range 0.5 V to 1.1 V vs NHE and are especially noticeable at higher scan rates. The pseudocapacitive behavior arises from the injection/ejection of protons that occurs at the noble metal-electrolyte interface and can be generically described by equation 1.6 .



where Me is the noble metal in the DSA<sup>®</sup> anode, the noble metals being iridium and ruthenium.

At the upper potential limit, around 1.40 V vs NHE, the onset of chlorine evolution is seen in the positive sweep, while in the negative sweep, chloride desorption can be identified by a slight deviation from the baseline. This feature is more noticeable at low scan rates since at higher scan rates the capacitive current densities overlap the desorption currents.

More detailed analysis of Figure 3.5a was done by plotting the anodic peak current density as a function of the square root of the scan rate, Figure 3.5b, which shows the linear dependence of the anodic peak current density on the square root of the scan rate, indicating a diffusion-controlled process [50].

#### 3.5.4 Electrochemical impedance spectroscopy

Figure 3.6a shows complex plane spectra obtained for a DSA<sup>®</sup> anode at different potentials in the range 65 kHz to 0.1 Hz in 5 mol dm<sup>-3</sup> NaCl. The current densities range from 40.3 mA cm<sup>-2</sup> at 1.40 V vs NHE to 140 mA cm<sup>-2</sup> at 1.60 V vs NHE; the ohmic resistance has been subtracted for clarity. The corresponding Bode diagrams are shown in Figure 3.6b.

Figure 3.6a shows a well-defined high-frequency semicircle for each spectrum. A low-frequency semicircle is only well defined at lower potentials. Spectra showing two semicircles have often been obtained for DSA<sup>®</sup> electrodes in sodium chloride solutions [19-21, 32]. These authors attribute the high frequency semicircle to the resistance and capacitance of the coating while the semicircle at lower frequencies is assigned to the capacitance of the double layer,  $C_{dl}$  and the charge transfer resistance,  $R_{ct}$ . In the present work, both semicircles should represent Faradaic processes since the diameter of both semicircles decreases with increase in potential. According to Hoseinieh and co-workers [21] and Ye and co-workers [32], the semicircle related to the coating should be independent of the potential. Therefore, the electrical equivalent circuit (EEC) used in the present work is shown in Figure 3.7.

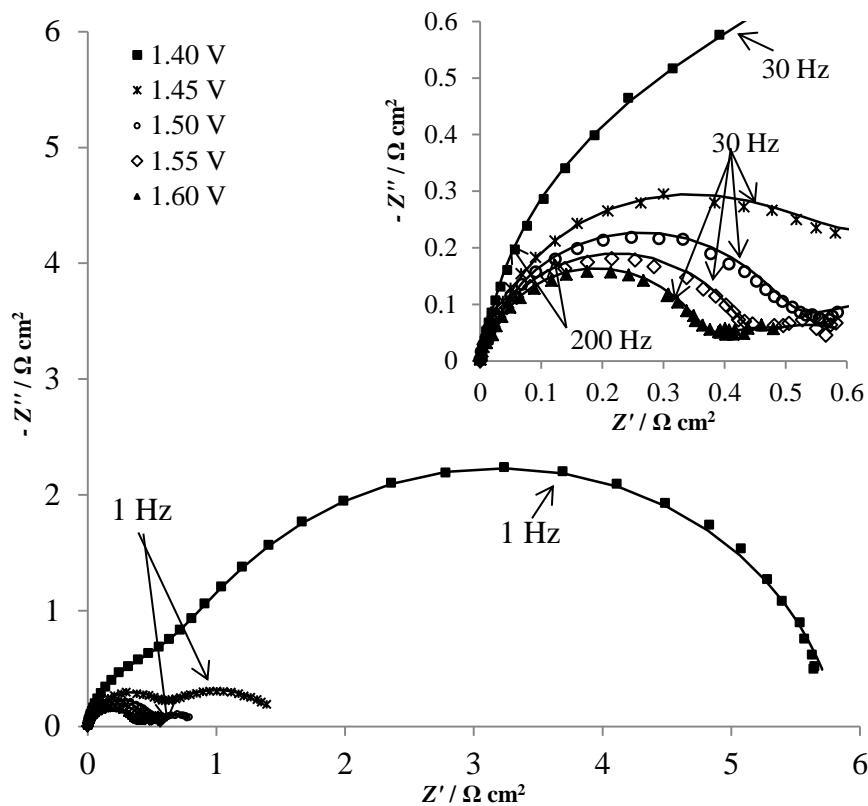
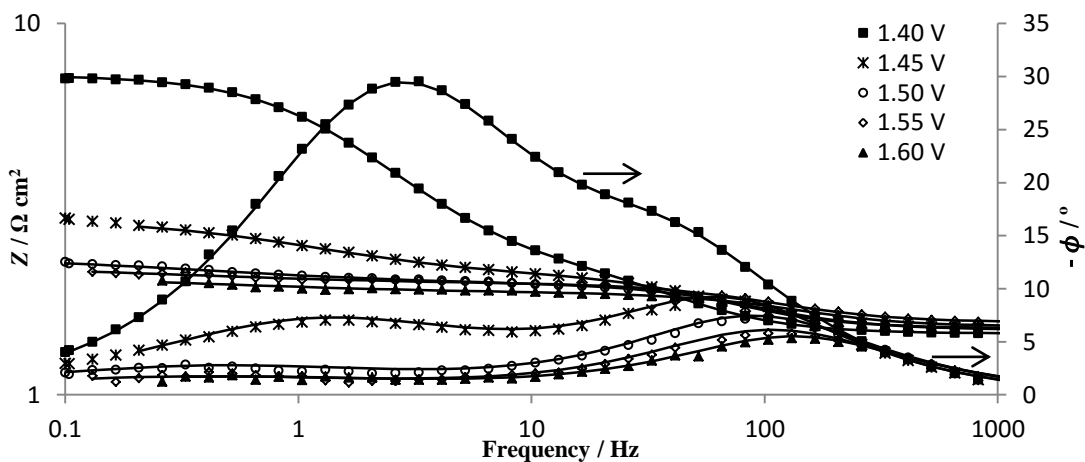
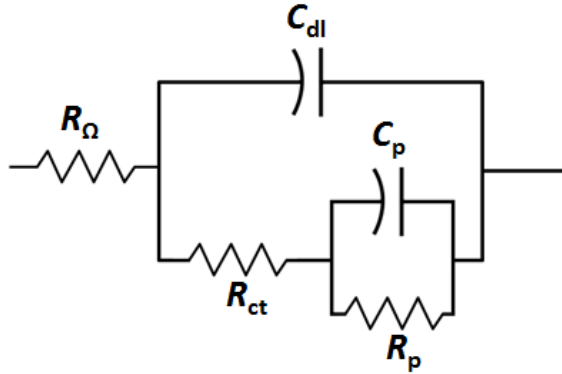
**a****b**

Figure 3.6 a - Complex plane spectra for a DSA® electrode in  $5 \text{ mol dm}^{-3} \text{ NaCl}$ , pH 2 at  $60 \text{ }^\circ\text{C}$  at different potentials. Inset shows the high frequency part of the spectra. Lines show equivalent circuit fitting. b - Bode diagrams of the spectra in Figure 3.6a. Lines show equivalent circuit fitting.

The EEC in Figure 3.7 includes elements to represent the pseudocapacitance,  $C_p$ , and the coupled resistance,  $R_p$ , which are assigned to the adsorption/ desorption of chloride intermediates that precede the chlorine formation;  $R_\Omega$  is the ohmic cell resistance.



**Figure 3.7 - Equivalent electrical circuit used to fit the impedance spectra.**

This EEC in was already used to fit the impedance of the chlorine evolution reaction on platinum electrodes [11, 12]. The charge transfer resistance should be related to chlorine evolution on the DSA<sup>®</sup> anode. Despite the thermodynamic potential for oxygen evolution being 1.23 V vs NHE and for chlorine 1.36 V vs NHE, the coating composition, which is designed for chlorine evolution, makes the oxygen kinetics sluggish. Thus, at the potentials used in the EIS measurements, oxygen evolution should be negligible compared to chlorine evolution [2].

The double layer capacitance and the pseudocapacitance were fitted to constant phase elements (CPE) instead of to ideal capacitors, the necessity arising from the non-uniform nature of both the electrode-solution interface and the coating, and manifested in the depressed semicircles. CPE have often been used to fit the impedance of DSA<sup>®</sup> anodes due to the roughness and porosity of the applied coating [21, 51, 52]. The impedance of the CPE,  $Z_{CPE}$ , is given by Equation 3.2:

$$Z_{CPE} = \frac{1}{Y_0(j\omega)^n} \quad (3.2)$$

where  $j$  is the imaginary number,  $\omega$  is the characteristic frequency in  $\text{rad s}^{-1}$ ,  $Y_0$  is the CPE magnitude and the exponent  $n$  is related to the uniformity of the electrode-solution interface – 1.0 for a completely uniform and homogeneous surface and 0.5 for a porous electrode. The values found for the parameters of the equivalent electrical circuit are shown in Table 3.1 where the subscripts  $dl$  represents the double layer and  $p$  is related to the semicircle at low frequencies.

**Table 3.1 - Fitting parameters and standard deviation (2 repeat spectra) obtained from the electrochemical impedance spectra at different potentials, data from Figure 3.6.**

$E^a$ vs NHE / V	1.40	1.45*	1.50	1.55	1.60
$R_{ct} / \Omega \text{ cm}^2$	$1.16 \pm 0.01$	0.60	$0.49 \pm 0.01$	$0.43 \pm 0.01$	$0.33 \pm 0.02$
$Y_{0,dl} / \text{mF cm}^{-2} \text{ s}^{n-1}$	$5.93 \pm 0.07$	5.55	$5.92 \pm 0.02$	$6.72 \pm 0.03$	$4.79 \pm 0.15$
$n_{dl}$	$0.96 \pm 0.01$	0.96	$0.94 \pm 0.01$	$0.92 \pm 0.01$	$0.96 \pm 0.01$
$R_p / \text{m}\Omega \text{ cm}^2$	$4.62 \pm 0.04$	0.93	$0.38 \pm 0.01$	$0.23 \pm 0.01$	$0.22 \pm 0.03$
$Y_{0,p} / \text{F cm}^{-2} \text{ s}^{n-1}$	$0.028 \pm 0.00$	0.32	$1.59 \pm 0.04$	$2.57 \pm 0.17$	$2.24 \pm 0.34$
$n_p$	$0.88 \pm 0.01$	0.71	$0.62 \pm 0.01$	$0.60 \pm 0.01$	$0.55 \pm 0.01$

\* Only one read.

The parameter values obtained display a low standard deviation (2 repeat spectra) indicating good precision of the impedance spectra. Some noise was, however, observed at low frequencies in the spectra recorded at higher potentials (1.55 V and 1.60 V vs NHE); this noise prevented fitting of the lowest frequency points and led to higher standard deviations in the values of  $Y_{0,p}$ .

The charge transfer resistance,  $R_{ct}$ , decreases with the potential, which is expected since the EIS experiments were performed within the faradaic region of the DSA<sup>®</sup> anode. The low  $R_{ct}$  values are related to the high activity of the DSA<sup>®</sup> anode for chlorine evolution. The double layer capacitance,  $Y_{0,dl}$ , is almost independent of potential in the potential range considered, ranging from  $4.79 \text{ mF cm}^{-2} \text{ s}^{n-1}$  to  $6.72 \text{ mF cm}^{-2} \text{ s}^{n-1}$ , in agreement with other authors [21]. The highest value obtained,  $6.72 \text{ mF cm}^{-2} \text{ s}^{n-1}$  at 1.55 V vs NHE, should

be a consequence of the lower value of the CPE exponent ( $n$ -value) obtained at this potential. The values of the double layer capacitance obtained suggest a macroscopically rough coating since, for smooth and compact electrode surfaces, the expected value would be around  $60 - 80 \mu\text{F cm}^{-2}$  [53]. Values in the  $\text{mF cm}^{-2}$  range have been assigned to the high roughness of the electrode surface and, even more important, to the presence of hydrated molecules in the coating [53]. These features are strongly dependent on the calcination temperature of the electrode coating [53].  $n$ -values smaller than 1.0, can be attributed to the porosity and roughness of the metal oxide coating that leads to a non-uniform current distribution on the electrode [21, 51, 52]. Nevertheless, the values of  $n$  close to 1.0, i.e. 0.92-0.96, show that the microscopic and sub-microscopic roughness of the surface is small. These values are rather different from those reported by Hoseinieh *et al.* [20, 21] who tested coatings with very similar composition to the ternary metal oxide-composition  $\text{IrO}_2\text{-TiO}_2\text{-RuO}_2$  used in this work; these authors found values of  $n$  around 0.60 for new anodes and around 0.92 for used electrodes. However, more dilute sodium chloride solutions ( $0.5 \text{ mol dm}^{-3} \text{ NaCl}$ ) were used.

Regarding the adsorption/desorption of chloride intermediates, represented by the low frequency semicircle, the low frequency resistance,  $R_p$ , decreases exponentially with increasing potential. This variation was reported for different electrochemical systems in which the same EEC as here was used [11, 54, 55] and confirms the faradaic nature of the adsorption processes. In this work, the value of  $C_p$  increased from  $0.028 \text{ F cm}^{-2} \text{ s}^{n-1}$  at 1.40 V vs NHE to  $2.57 \text{ F cm}^{-2} \text{ s}^{n-1}$  at 1.55 V vs NHE, before decreasing to  $2.24 \text{ F cm}^{-2} \text{ s}^{n-1}$  at 1.60 V vs NHE. Since  $C_p$  is proportional to the variation of the free active sites with potential  $d\theta/dE$  [56], the maximum observed in  $C_p$  corresponds to the maximum value of  $d\theta/dE$ . The CPE exponent at low frequencies,  $n_p$ , decreases with the applied potential, from a value of 0.88 at 1.40 V NHE, down to 0.55 at 1.60 V vs NHE. This decrease suggests that at higher potentials and higher current densities, the flux of reactants is not sufficient to compensate the depletion of ions on the surface of the pores of the coating, leading to non-uniformity.

### 3.6 Conclusions

A new electrochemical cell has been designed, fabricated and tested for studying the performance of DSA<sup>®</sup> electrodes during chlorine evolution. The cell is able to accommodate electrodes with only one face contacting the electrolyte. The working electrode was fitted to the bottom of the electrochemical cell with a leak-free O-ring seal. This special configuration together with the cell stirring guarantee fast gas removal from the electrode surface during chlorine evolution, leading to high quality impedance spectra and polarization curves. Polarization curves, cyclic voltammetry and impedance measurements demonstrated the good performance of the electrochemical cell over the faradaic regions of applied potential. EIS measurements were made at different potentials, with current densities up to  $140 \text{ mA cm}^{-2}$ . The EIS and the polarization curves evidence the role of adsorption steps in the chlorine evolution reaction, in agreement with the Volmer-Heyrovsky and Volmer-Tafel mechanisms.

The new cell represents an important development for the study and characterization of DSA<sup>®</sup> electrodes under conditions similar to those used in the chlorine industry.

### 3.7 References

1. Schmittinger, P., *Chlorine: Principles & Industrial Practice*. 2008, Weinheim: Wiley-VCH.
2. O'Brien, T., T.V. Bommaraju, and F. Hine, *Handbook of chlor-alkali technology*. 2005, New York: Springer.
3. Bommaraju, T.V., et al., *Chlorine in Kirk-Othmer Encyclopedia of Chemical Technology, Electronic release*, R.E. Kirk and D.F. Othmer, Editors. 2002, John Wiley & Sons, Inc.: New York.
4. Schmittinger, P., et al., *Chlorine in Ullmann's Encyclopedia of Industrial Chemistry, Electronic release*, B. Elvers, Editor. 2012, Wiley-VCH: Weinheim. p. 531-621.
5. Calvo, E.J., et al., *Electrode Kinetics: Reactions in Comprehensive Chemical Kinetics*, R.G. Compton, Editor. 1987, Elsevier: Amsterdam.
6. Kuhn, A.T. and C.J. Mortimer, *The Kinetics of Chlorine Evolution and Reduction on Titanium-Supported Metal Oxides Especially RuO<sub>2</sub> and IrO<sub>2</sub>*. Journal of The Electrochemical Society, 1973. **120**(2): p. 231-236.
7. Janssen, L.J.J., et al., *Mechanism of the chlorine evolution on a ruthenium oxide/titanium oxide electrode and on a ruthenium electrode*. Electrochimica Acta, 1977. **22**(10): p. 1093-1100.
8. Krishtalik, L.I., *Kinetics and mechanism of anodic chlorine and oxygen evolution reactions on transition metal oxide electrodes*. Electrochimica Acta, 1981. **26**(3): p. 329-337.
9. Santana, M.H.P. and L.A. De Faria, *Oxygen and chlorine evolution on RuO<sub>2</sub> + TiO<sub>2</sub> + CeO<sub>2</sub> + Nb<sub>2</sub>O<sub>5</sub> mixed oxide electrodes*. Electrochimica Acta, 2006. **51**(17): p. 3578-3585.
10. Boggio, R., et al., *Mechanistic study of Cl<sub>2</sub> evolution at Ti-supported Co<sub>3</sub>O<sub>4</sub> anodes*. Journal of Applied Electrochemistry, 1985. **15**(3): p. 335-349.
11. Conway, B.E. and G. Ping, *Evaluation of Cl' adsorption in anodic Cl<sub>2</sub> evolution at Pt by means of impedance and potential-relaxation experiments. Influence of the state of surface oxidation of the Pt*. Journal of the Chemical Society, Faraday Transactions, 1991. **87**(17): p. 2705-2714.
12. Li, F.B., A.R. Hillman, and S.D. Lubetkin, *A new approach to the mechanism of chlorine evolution: Separate examination of the kinetic steps using ac impedance on a rotating thin ring electrode*. Electrochimica Acta, 1992. **37**(15): p. 2715-2723.
13. Conway, B.E. and G. Ping, *Surface electrochemistry of the anodic Cl<sub>2</sub> evolution reaction at Pt. Influence of co-deposition of surface oxide species on adsorption of the Cl' intermediate*. Journal of the Chemical Society, Faraday Transactions, 1990. **86**(6): p. 923-930.
14. Panić, V.V., et al., *The effect of the addition of colloidal iridium oxide into sol-gel obtained titanium and ruthenium oxide coatings on titanium on their electrochemical properties*. Physical Chemistry Chemical Physics, 2010. **12**(27): p. 7521-7528.

15. Zhou, X.L., et al., *Electrocatalytic activity and stability of Ti/IrO<sub>2</sub> + MnO<sub>2</sub> anode in 0.5 M NaCl solution*. Journal of Solid State Electrochemistry, 2010. **14**(7): p. 1213-1219.
16. Alves, V.A., L.A. da Silva, and J.F.C. Boodts, *Surface characterisation of IrO<sub>2</sub>/TiO<sub>2</sub>/CeO<sub>2</sub> oxide electrodes and Faradaic impedance investigation of the oxygen evolution reaction from alkaline solution*. Electrochimica Acta, 1998. **44**(8-9): p. 1525-1534.
17. Malpass, G.R.P., R.S. Neves, and A.J. Motheo, *A comparative study of commercial and laboratory-made Ti/Ru<sub>0.3</sub>Ti<sub>0.7</sub>O<sub>2</sub> DSA® electrodes: "In situ" and "ex situ" surface characterisation and organic oxidation activity*. Electrochimica Acta, 2006. **52**(3): p. 936-944.
18. Panić, V.V., et al., *Differences in the electrochemical behavior of ruthenium and iridium oxide in electrocatalytic coatings of activated titanium anodes prepared by the sol-gel procedure*. Journal of the Serbian Chemical Society, 2010. **75**(10): p. 1413-1420.
19. Xu, L.K. and J.D. Scantlebury, *A study on the deactivation of an IrO<sub>2</sub>-Ta<sub>2</sub>O<sub>5</sub> coated titanium anode*. Corrosion Science, 2003. **45**(12): p. 2729-2740.
20. Hoseinie, S.M. and F. Ashrafizadeh, *Influence of electrolyte composition on deactivation mechanism of a Ti/Ru<sub>0.25</sub>Ir<sub>0.25</sub>Ti<sub>0.5</sub>O<sub>2</sub> electrode*. Ionics, 2013. **19**(1): p. 113-125.
21. Hoseinie, S.M., F. Ashrafizadeh, and M.H. Maddahi, *A Comparative Investigation of the Corrosion Behavior of RuO<sub>2</sub>-IrO<sub>2</sub>-TiO<sub>2</sub> Coated Titanium Anodes in Chloride Solutions*. Journal of The Electrochemical Society, 2010. **157**(4): p. E50-E56.
22. Denton, D.A., J.A. Harrison, and R.I. Knowles, *Chlorine evolution and reduction on RuO<sub>2</sub>/TiO<sub>2</sub> electrodes*. Electrochimica Acta, 1979. **24**(5): p. 521-527.
23. Harrison, J.A., D.L. Caldwell, and R.E. White, *Electrocatalysis and the chlorine evolution reaction - II. Comparison of anode materials*. Electrochimica Acta, 1984. **29**(2): p. 203-209.
24. Kissinger, P. and W.R. Heineman, *Laboratory Techniques in Electroanalytical Chemistry, Second Edition, Revised and Expanded*. 1996, New York: Taylor & Francis.
25. Watanabe, N., J. Morais, and M.C.M. Alves, *Design of an electrochemical cell for in situ XAS studies*. Journal of Electron Spectroscopy and Related Phenomena, 2007. **156-158**(0): p. 164-167.
26. Wozniak, N.R., et al., *An electrochemical cell for the efficient turn around of wafer working electrodes*. Review of Scientific Instruments, 2010. **81**(3): p. -.
27. Tymoczko, J., W. Schuhmann, and A.S. Bandarenka, *A versatile electrochemical cell for the preparation and characterisation of model electrocatalytic systems*. Physical Chemistry Chemical Physics, 2013. **15**(31): p. 12998-13004.
28. Mu, X.H. and F.A. Schultz, *Electrochemical cell design and experimental procedures for measuring electrode reaction kinetics at low and variable temperatures*. Electroanalysis, 1990. **2**(5): p. 353-357.

29. Cahan, B.D., Z. Nagy, and M.A. Genshaw, *Cell Design for Potentiostatic Measuring System*. Journal of The Electrochemical Society, 1972. **119**(1): p. 64-69.
30. Raju, T. and C.A. Basha, *Electrochemical cell design and development for mediated electrochemical oxidation-Ce(III)/Ce(IV) system*. Chemical Engineering Journal, 2005. **114**(1-3): p. 55-65.
31. Zoski, C.G., *Handbook of Electrochemistry*. 2007, Amsterdam: Elsevier.
32. Ye, Z.G., H.M. Meng, and D.B. Sun, *Electrochemical impedance spectroscopic (EIS) investigation of the oxygen evolution reaction mechanism of Ti/IrO<sub>2</sub> + MnO<sub>2</sub> electrodes in 0.5 m H<sub>2</sub>SO<sub>4</sub> solution*. Journal of Electroanalytical Chemistry, 2008. **621**(1): p. 49-54.
33. Torcheux, L., A. Mayeux, and M. Chemla, *Electrochemical Coupling Effects on the Corrosion of Silicon Samples in HF Solutions*. Journal of The Electrochemical Society, 1995. **142**(6): p. 2037-2046.
34. McCafferty, E., *Introduction to Corrosion Science*. 2010, New York: Springer.
35. Ghahremaninezhad, A., E. Asselin, and D.G. Dixon, *Cathodic Reactions on Oxidized Chalcopyrite Electrode in Electrometallurgy 2012*, M. Free and M. Moats, Editors. 2012, John Wiley & Sons, Inc. p. 199-206.
36. Matsushima, H., T. Iida, and Y. Fukunaka, *Observation of bubble layer formed on hydrogen and oxygen gas-evolving electrode in a magnetic field*. Journal of Solid State Electrochemistry, 2012. **16**(2): p. 617-623.
37. Trasatti, S., *Electrocatalysis in the anodic evolution of oxygen and chlorine*. Electrochimica Acta, 1984. **29**(11): p. 1503-1512.
38. Janssen, L.J.J., *Mass transfer at gas evolving electrodes*. Electrochimica Acta, 1978. **23**(2): p. 81-86.
39. Klink, S., et al., *The importance of cell geometry for electrochemical impedance spectroscopy in three-electrode lithium ion battery test cells*. Electrochemistry Communications, 2012. **22**(0): p. 120-123.
40. Offer, G.J., et al., *Using electrochemical impedance spectroscopy to compensate for errors when measuring polarisation curves during three-electrode measurements of solid oxide fuel cell electrodes*. Electrochimica Acta, 2008. **53**(26): p. 7614-7621.
41. Fouad, M.G. and G.H. Sedahmed, *Mass transfer at horizontal gas-evolving electrodes*. Electrochimica Acta, 1973. **18**(1): p. 55-58.
42. Ovarfort, R., *New electrochemical cell for pitting corrosion testing*. Corrosion Science, 1988. **28**(2): p. 135-140.
43. Bertagna, V., F. Rouelle, and M. Chemla, *An improved electrochemical cell for the characterization of silicon/electrolyte interfaces*. Journal of Applied Electrochemistry, 1997. **27**(10): p. 1179-1183.
44. Hendricks, S.A., Y.T. Kim, and A.J. Bard, *Imaging of the In Situ Deposition of Lead on Highly Oriented Pyrolytic Graphite by Scanning Tunneling and Atomic Force Microscopies*. Journal of The Electrochemical Society, 1992. **139**(10): p. 2818-2824.
45. Yaniv, D.R. and P.S. Jung, *A novel design of a constant volume electrochemical cell for atomic force microscopy measurements*. Electroanalysis, 1995. **7**(3): p. 260-263.

46. Bowler, R., et al., *Electrochemical Cell for Surface Analysis*. Analytical Chemistry, 2005. **77**(6): p. 1916-1919.
47. Consonni, V., et al., *Mechanism of chlorine evolution on oxide anodes - Study of pH effects*. Journal of Electroanalytical Chemistry and Interfacial Electrochemistry, 1987. **228**(1-2): p. 393-406.
48. Tilak, B.V., et al., *Capacitive and kinetic characteristics of Ru-Ti oxide electrodes: influence of variation in the Ru content*. Canadian Journal of Chemistry, 1997. **75**(11): p. 1773-1782.
49. Fathollahi, F., et al., *Comparison of morphology, stability and electrocatalytic properties of  $Ru_{0.3}Ti_{0.7}O_2$  and  $Ru_{0.3}Ti_{0.4}Ir_{0.3}O_2$  coated titanium anodes*. Russian Journal of Electrochemistry, 2011. **47**(11): p. 1281-1286.
50. Brett, C.M.A. and A.M. Oliveira-Brett, *Electrochemistry: Principles, Methods, and Applications*. 1993, Oxford: Oxford University Press.
51. Alves, V.A., L.A.d. Silva, and J.F.C. Boodts, *Electrochemical impedance spectroscopic study of dimensionally stable anode corrosion*. Journal of Applied Electrochemistry, 1998. **28**(9): p. 899-905.
52. Ribeiro, J. and A.R. de Andrade, *Investigation of the electrical properties, charging process, and passivation of  $RuO_2-Ta_2O_5$  oxide films*. Journal of Electroanalytical Chemistry, 2006. **592**(2): p. 153-162.
53. Lassali, T.A.F., J.F.C. Boodts, and L.O.S. Bulhões, *Charging processes and electrocatalytic properties of  $IrO_2/TiO_2/SnO_2$  oxide films investigated by in situ AC impedance measurements*. Electrochimica Acta, 1999. **44**(24): p. 4203-4216.
54. Krstajić, N.V., S. Burojević, and L.M. Vračar, *The determination of kinetics parameters of the hydrogen evolution on Pd-Ni alloys by ac impedance*. International Journal of Hydrogen Energy, 2000. **25**(7): p. 635-641.
55. Krstajić, N., et al., *On the kinetics of the hydrogen evolution reaction on nickel in alkaline solution: Part I. The mechanism*. Journal of Electroanalytical Chemistry, 2001. **512**(1-2): p. 16-26.
56. Bai, L., D.A. Harrington, and B.E. Conway, *Behavior of overpotential deposited species in faradaic reactions. 2. AC impedance measurements on  $H_2$  evolution kinetics at activated and unactivated Pt cathodes*. Electrochimica Acta, 1987. **32**(12): p. 1713-1731.

## **4 Kinetic analysis of chlorine evolution on TiO<sub>2</sub>-RuO<sub>2</sub>-IrO<sub>2</sub> DSA<sup>®</sup> anode by EIS and anodic polarisation curves**

### **4.1 Abstract**

The mechanism of chlorine evolution on DSA<sup>®</sup> anodes was studied in a 1 mol dm<sup>-3</sup> NaCl solution at pH = 2 and 293 K. Rate constants were determined using a non-linear least square fitting method that combines data from anodic polarisation curves and electrochemical impedance spectroscopy (EIS). The adsorbed intermediate chlorine species is detected by EIS in the low frequency region of the impedance spectra. An Armstrong-based electrical equivalent circuit was used to fit the impedance spectra, which includes a pseudocapacitance related to the adsorption phenomena.

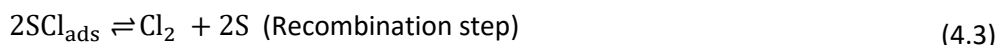
In the potential range investigated 1.36 V vs NHE to 1.60 V vs NHE, the coverage of chlorine compounds was between 0.03 and 0.30. In the absence of mass transport limitations, a Volmer-Heyrovsky-Tafel mechanism with a rate-determining Tafel step described the evolution of chlorine on DSA<sup>®</sup> anodes. The Volmer step is mostly followed by the Tafel step, although the Heyrovsky step cannot be neglected.

## 4.2 Introduction

Chlorine is among the ten most produced chemicals in the world [1], ca. 95% of it being produced by the electrochemical route [1]. In the electrochemical cell, chlorine is produced by chloride oxidation at the anode, the chloride coming from concentrated sodium chloride solution feed. The anodes used in the process, dimensionally stable anodes (DSA<sup>®</sup>), are composed of different transition metal oxides applied on a titanium substrate. In the case of DSA<sup>®</sup> for the chlorine industry, the most used metal oxides are RuO<sub>2</sub>, IrO<sub>2</sub> and TiO<sub>2</sub> [1, 2]. Ruthenium oxide is the electroactive catalyst while titanium dioxide is the valve metal. Iridium oxide, added many years after the introduction to the market of DSA<sup>®</sup> electrodes, was shown to increase the stability and service lifetime of DSA<sup>®</sup> electrodes during the chlorine and oxygen evolution reactions [1-5]. Industrial electrodes are coated by thermal decomposition [1, 2], although other methods such as sol-gel [3, 6] or alkoxide ink have been investigated [7].

DSA<sup>®</sup> anodes were first reported by Beer in 1965 [8], three years before their industrial application. However, the first article describing the fundamental properties of DSA<sup>®</sup> electrodes was published only in 1971 [9]; this sequence of events is related to the industrial origin of DSA<sup>®</sup> electrodes [2]. Fundamental research on DSA<sup>®</sup> electrodes became a hot topic in the 1970's and 1980's. During this period, a number of articles addressing the mechanism of chlorine evolution on DSA<sup>®</sup> electrodes were published [10-17]. In 1987, Trasatti summarised the most relevant aspects of the kinetic analysis of chlorine evolution on DSA<sup>®</sup> electrodes, including a detailed review of the main mechanisms for the chlorine evolution reaction on this type of anode [18].

The first relevant mechanism proposed for the chlorine evolution reaction (CIER), by chloride oxidation, is the so-called Volmer-Heyrovsky-Tafel (VHT) mechanism that resembles the typical mechanistic approach to describe the cathodic evolution of hydrogen. It proposes the co-existence of two alternative steps, an electrochemical desorption (Heyrovsky) or a recombination (Tafel) step, which follow the discharge (Volmer) step, Equation 4.1 to 4.3.

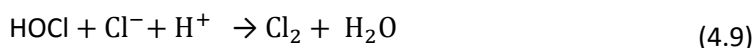
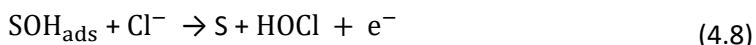
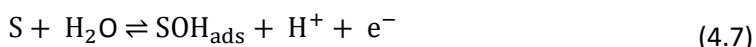


where S is the substrate on which the intermediates adsorb.

Another mechanism commonly employed to describe the CIER was proposed by Krishtalik and Erenburg in 1975 [18]. This mechanism is represented by Equations 4.4 to 4.6 and includes a positively-charged adsorbed chlorine intermediate ( $\text{SCl}_{\text{ads}}^+$ ) the nature of which is not completely understood [18]:



Later, the same author authors proposed a new mechanism to include the effect of pH, Equations 4.7 to 4.9.



and predicts the participation of water, Equation 4.7.

Other mechanisms which are simplifications or modifications of the VHT and Erenburg-Krishtalik mechanisms, were subsequently deduced and are found in the literature. Panić and co-workers in 1999 [19] proposed the Volmer-Heyrovsky mechanism to describe the CIER at a DSA<sup>®</sup> anode with titanium as substrate coated with a RuO<sub>2</sub>-TiO<sub>2</sub> binary oxide. Later, in 2002, Ferro and Battisti proposed the same mechanism for the CIER at a diamond anode coated with RuO<sub>2</sub> [20].

In 2001 Fernández and co-workers investigated the CIER mechanism based on analysis of the polarisation resistance [21]. These authors proposed a Volmer-Krishtalik-Tafel mechanism to explain the chlorine evolution on a Ti/RuO<sub>2</sub> DSA<sup>®</sup> electrode. Different conclusions were reached by Santana and co-workers who found that the Erenburg-

Krishtalik mechanism (Equations 4.4 to 4.6) successfully described chlorine evolution on a DSA<sup>®</sup> electrode coated with RuO<sub>2</sub>-TiO<sub>2</sub>-CeO<sub>2</sub>-Nb<sub>2</sub>O<sub>5</sub> [22].

The extended range of published mechanisms for the same reaction and for the same or similar electrodes illustrates how much progress is needed for the full understanding of ClER. Most studies relied essentially on analysis of the polarisation curves, occasionally complemented with potential-relaxation experiments.

Although EIS is recognised to be a powerful technique, its application to study the kinetics of the chlorine evolution on DSA<sup>®</sup> electrodes has been limited. In 1979, electrochemical impedance spectroscopy was used by Denton and co-workers [14] in the kinetic study of ClER in HCl and KCl at titanium substrates coated with a binary oxide mixture, RuO<sub>2</sub>-TiO<sub>2</sub>. However, the experiments were carried out in the capacitive region of the electrode and only the dependence of the capacitance on applied potential was analysed; a brief mention of charge transfer resistance was made, although no quantitative data were provided. Four years later Harrison and co-workers [13, 23] went further and used impedance data to obtain the kinetic constants of the ClER in 5 mol dm<sup>-3</sup> NaCl solution at titanium substrates coated with TiO<sub>2</sub>-RuO<sub>2</sub>. However, the mechanism considered for the ClER, involving the simultaneous transfer of two electrons, is unlikely.

EIS has been used to study the stability and activity of different coatings during the evolution of chlorine [4, 24, 25] and oxygen [26-28], as well as to study alternative coating methods [3, 6, 7]. In most of the reports, the impedance spectra were analysed exclusively in terms of the values of the electrical equivalent circuit elements.

Apart from the ClER, the calculation of cathodic rate constants from impedance data was carried out by Bai, Harrington and Conway who, in 1987, postulated the Volmer-Heyrovsky-Tafel mechanism [29, 30] for the cathodic evolution of hydrogen. In [29] these authors developed theory to establish relations between the elements of the electrical equivalent circuit and the rate equations. The authors used an adaptation of Armstrong's circuit [31], that includes elements to describe adsorption phenomena on the electrode, in order to fit the faradaic impedance spectra. In the second article, [30], experimental data were employed to calculate the parameters of the mechanistic reaction model for

hydrogen evolution on platinum cathodes and to validate the theoretical model proposed in their previous article. A similar approach was used by Conway and Ping [32] in 1991 and by Li and co-workers in 1992 [33] for the anodic evolution of chlorine on platinum electrodes. Between 1997 and 2001, Krastajić and co-workers published a series of four articles concerning cathodic hydrogen evolution on electrodes of different compositions [34-37]. The authors used data from the characteristic polarisation curve together with the impedance spectra to calculate the parameters of the proposed mechanistic reaction model.

Later, in 2004, Hu and co-workers proposed a mechanism for the evolution of oxygen on a DSA<sup>®</sup> electrode [38], deducing the characteristic curve and the impedance response of the system. The proposed mechanism, which included the effect of adsorption/desorption of intermediate species, was validated by experimental results. These authors concluded that simultaneously using the characteristic curve and the impedance spectra, a more comprehensive kinetic model could be obtained.

More recently, Harrington [39] and Harrington and Driessche [40] predicted the electrochemical impedance response as a function of the mechanism and of the rate-determining step. They compared the elements of the electrical equivalent circuit used to adjust the impedance spectra, chosen so as to have a physical meaning, with the characteristic curve parameters.

This work models the anodic evolution of chlorine on a DSA<sup>®</sup> anode using the Volmer-Heyrovsky-Tafel mechanism. The kinetic parameters were calculated by simultaneously fitting the experimental data of the characteristic curve and the impedance spectra to the proposed mechanistic model by minimizing the sum-squared residues. Good agreement between the model and experimental data was obtained, thus shedding new light on the mechanism of chlorine evolution on DSA<sup>®</sup> electrodes.

## 4.3 Experimental

### Electrodes

A 2.0 cm<sup>2</sup> DSA<sup>®</sup> commercial anode made of RuO<sub>2</sub>-IrO<sub>2</sub>-TiO<sub>2</sub> coated titanium from De Nora was used. A platinum mesh was used as counter electrode and an Ag/AgCl electrode saturated with KCl as reference electrode.

Exploratory experiments showed the need for preconditioning the working electrode to obtain reproducible characteristic curves and impedance spectra, as suggested elsewhere [32, 33]. The pre-treatment of the anode included two steps: (i) 10 potential cycles from 0.0 V vs NHE to 1.2 V vs NHE at 50 mV s<sup>-1</sup> and (ii) 300 s polarisation at 0.5 V vs NHE.

### Reagents

Sodium chloride solutions were prepared from high purity 5 mol dm<sup>-3</sup> NaCl solutions. The initial pH was set to 2 using industrial grade HCl 33 wt. %. Both solutions were supplied by CUF-QI (Portugal). When necessary, the initial solution was diluted using deionised ultrapure water (Millipore, resistivity ≥ 18 MΩ cm).

### Electrochemical cell

The electrochemical cell used for the accelerated ageing test and for the characterisation of the anode is described in Chapter 3.

### Electrochemical characterisation

The electrochemical measurements were performed at 20 °C using an IM6ex Zahner Electrochemical station. Cyclic voltammetry experiments were run between 0.0 V vs NHE to +1.2 V vs NHE, covering the capacitive / pseudocapacitive region of the electrode. Ten potential cycles were performed at a scan rate of 50 mV s<sup>-1</sup>. The polarization curves were obtained at 1 mV s<sup>-1</sup> in the potential range between +1.2 V and +1.75 V vs NHE. The

contribution of ohmic resistance,  $R_{\Omega}$ , obtained by EIS analysis, was subtracted from the polarization curves.

The impedance spectra were obtained in potentiostatic mode with a 10 mV rms amplitude perturbation in the frequency range 65 kHz to 100 mHz. At higher frequencies 10 data points per decade, each one integrated 10 cycles were recorded; below 66 Hz, the impedance was measured at 5 data points per decade, each one integrating the 5 cycles. Impedance spectra were recorded in the range 1.34 V to 1.60 V vs NHE; these potentials are in the chlorine evolution potential region. The spectra were fitted to electrical equivalent circuits using Zview<sup>®</sup> 3.1c (Scribner, USA). Kinetic constants were calculated by a non-linear least squares method, which minimizes the residuals of the polarization curves and EIS simultaneously.

The cell was stirred at 500 rpm during polarization curve recording and EIS measurements. The pH of the electrolyte solution was measured using a WTW Microprocessor pH-Meter pH 3000. The temperature was controlled using a HUBER CC1 water bath.

#### **4.4 Calculations**

Information from polarisation curves and EIS is used simultaneously to compute the kinetic constants and the symmetry factors. The methodology used is based on the approach followed by Krstajić and co-authors [34-37] with the assumptions:

- i) There are no side reactions;
- ii) There are no diffusional limitations;
- iii) The adsorption of chlorine intermediate species follows a Langmuir isotherm;

Assuming the Volmer-Heyrovsky-Tafel (VHT) mechanism for chlorine evolution on a DSA<sup>®</sup> anode, the reaction rates,  $v$ , for the three steps are<sup>1</sup>:

$$v_1 = k_1(1 - \theta) \exp\left(\frac{\beta F \eta}{RT}\right) - k_{-1} \theta \exp\left[\frac{-(1 - \beta F \eta)}{RT}\right] \quad (4.10)$$

$$v_2 = k_2 \theta \exp\left(\frac{\gamma F \eta}{RT}\right) - k_{-2}(1 - \theta) \exp\left[\frac{-(1 - \gamma F \eta)}{RT}\right] \quad (4.11)$$

$$v_3 = k_3 \theta^2 - k_{-3}(1 - \theta)^2 \quad (4.12)$$

where  $F$  is the Faraday constant,  $\beta$  is the symmetry factor of the Volmer step and  $\gamma$  is the symmetry factor of the Heyrovsky step,  $R$  is the gas constant,  $T$  is the absolute temperature, and is  $\theta$  the surface fraction of occupied sites. The rate constants,  $k$ , include the concentration of  $\text{Cl}^-$  and  $\text{Cl}_2$ .

The charge balance at constant current density ( $r_0$ ) and the mass balance of adsorbed species ( $r_1$ ) are:

$$r_0 = \frac{j}{F} = (v_1 + v_2) \quad (4.13)$$

$$r_1 = \left(\frac{q}{F}\right) \left(\frac{\partial \theta}{\partial t}\right) = v_1 - v_2 - 2v_3 \quad (4.14)$$

where  $j$  is the total current density and  $q$  is the charge of the fully completed monolayer.

At steady-state,  $r_1 = 0$ , and Equation 4.15 can be solved to obtain the fraction of sites adsorbing chlorine intermediates:

$$\theta = \frac{-(k_1 + k_{-1} + k_2) + \sqrt{(k_1 + k_{-1} + k_2)^2 + 8k_1 k_3}}{4k_3} \quad (4.15)$$

The pseudocapacitance,  $C_\phi$ , which is related to the adsorption of charged species,  $q$ , is calculated by equation 4.16 [41]:

---

<sup>1</sup> Subscripts 1, 2 and 3 refer to the Volmer, Heyrovsky and Tafel steps, respectively. The minus operator designates the backward kinetic constant. Exploratory tests showed the insignificant contribution of the backward reaction of the Heyrovsky and Volmer steps.

$$C_{\phi} = q \frac{d\theta}{dE} \quad (4.16)$$

The correspondence between the elements of the electrical equivalent circuit and the polarisation curve is given by Equations 4.17 to 4.21 [29, 30, 32]:

$$\frac{1}{R_{ct}} = F \left[ \left( \frac{\partial v_1}{\partial \eta} \right)_{\theta} + \left( \frac{\partial v_2}{\partial \eta} \right)_{\theta} \right] \quad (4.17)$$

$$\frac{1}{R_0} = \left( \frac{F^2 \tau}{q} \right) \left[ \left( \frac{\partial v_1}{\partial \theta} \right)_{\eta} + \left( \frac{\partial v_2}{\partial \theta} \right)_{\eta} \right] \times \left[ \left( \frac{\partial v_1}{\partial \eta} \right)_{\theta} - \left( \frac{\partial v_2}{\partial \eta} \right)_{\theta} \right] \quad (4.18)$$

$$R_P = - \frac{R_{ct}^2}{R_0 + R_{ct}} \quad (4.19)$$

$$\frac{1}{\tau} = \left( \frac{F}{q_0} \right) \left[ 2 \left( \frac{\partial v_3}{\partial \theta} \right)_{\eta} + \left( \frac{\partial v_2}{\partial \theta} \right)_{\eta} - \left( \frac{\partial v_1}{\partial \theta} \right)_{\eta} \right] \quad (4.20)$$

$$C_P = - \frac{R_0 \tau}{R_{ct}^2} \quad (4.21)$$

Here,  $R_{ct}$  is the charge transfer resistance,  $C_p$  and  $R_p$  are the capacitance and resistance related to the adsorption/ desorption of chlorine intermediates;  $R_0$  is an auxiliary variable and  $\tau$  is the relaxation time parameter associated with the adsorption of intermediates as defined by Armstrong and Henderson [31].

The derivatives in Equations 4.17 to 4.21 are given by equations 4.22 to 4.26:

$$\left( \frac{\partial v_1}{\partial \eta} \right)_{\theta} = \left( \frac{\beta F}{RT} \right) [k_1(1 - \theta) + k_{-1}\theta] \quad (4.22)$$

$$\left( \frac{\partial v_2}{\partial \eta} \right)_{\theta} = \left( \frac{\beta F}{RT} \right) k_2 \theta \quad (4.23)$$

$$\left( \frac{\partial v_1}{\partial \theta} \right)_{\eta} = -k_1 - k_{-1} \quad (4.24)$$

$$\left( \frac{\partial v_2}{\partial \theta} \right)_{\eta} = k_2 \quad (4.25)$$

$$\left( \frac{\partial v_3}{\partial \theta} \right)_{\eta} = 2k_3 \theta \quad (4.26)$$

Equation 4.27 is the objective function used to calculate the variables involved by simultaneously minimizing the sum of the residuals of data from polarization curves and EIS.

$$S = \sum_{i=1}^n \left\{ \frac{j_{i,exp} - j_{i,mod}}{j_{i,exp}} \right\}^2 + \sum_{j=1}^m \left\{ \left( \frac{R_{ct,EEC} - R_{ct,mod}}{R_{ct,EEC}} \right)^2 + \left( \frac{R_{p,EEC} - R_{p,mod}}{R_{p,EEC}} \right)^2 \right\} \quad (4.27)$$

The decision variables are the kinetic constants,  $k_1$ ,  $k_{-1}$ ,  $k_2$ ,  $k_3$  and the symmetry factors of the Volmer step,  $\beta$ , and of the Heyrovsky step,  $\gamma$ . The subscript *exp* refers to the experimental data from polarisation curves, *EEC* refers to the values obtained from the fitting to the Electrical Equivalent Circuit (EEC) and the subscript *mod* represents the values obtained from the model. The symbol  $n$  is the number of experimental points considered for the polarisation curves and  $m$  represents the number of different potentials at which the impedance of the system was recorded.

## 4.5 Results and Discussion

### Electrochemical impedance spectroscopy

The impedance of the DSA<sup>®</sup> anode was obtained at different potentials within the range of potentials set for the polarization curve. Figure 4.1 shows impedance spectra in the complex plane recorded during the CIER on DSA<sup>®</sup> in 1 mol dm<sup>-3</sup> NaCl solution. The ohmic resistance has been removed for improving readability. The corresponding Bode diagrams are shown in Figure 4.2. The complex plane spectra show two semicircles at all potentials investigated, significantly overlapping at 1.36 V. While the semicircle at higher frequencies is well defined over all the potential range investigated, the semicircle at lower frequencies tends to disappear.

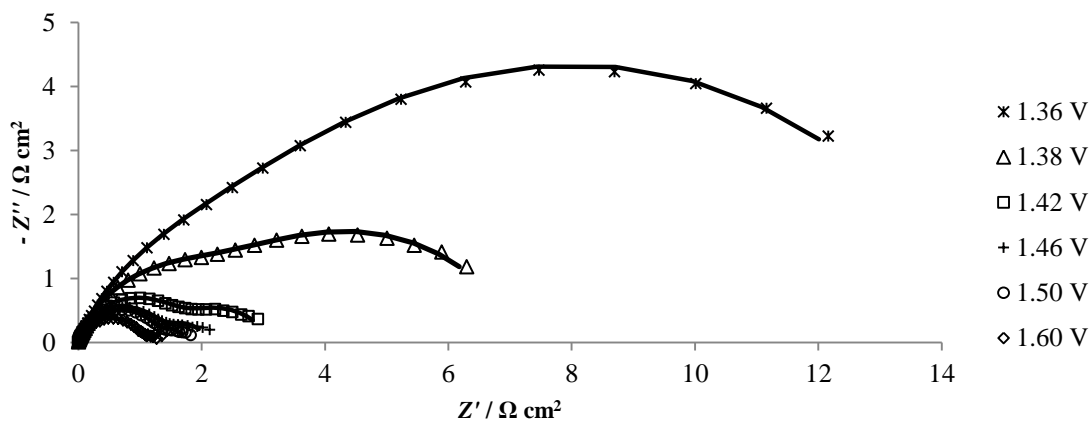
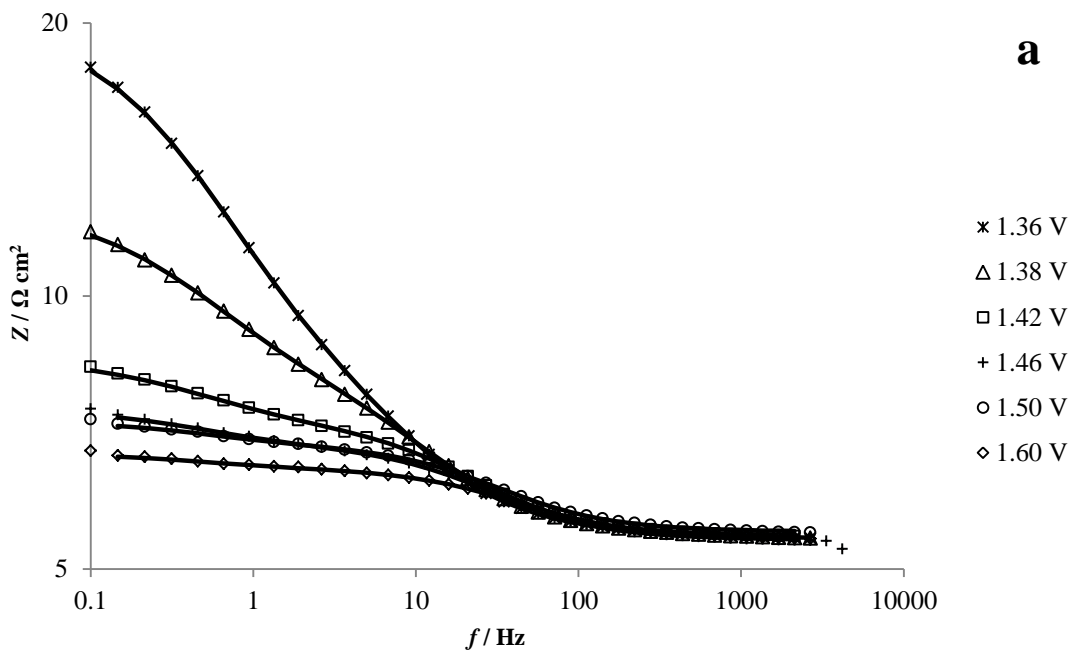


Figure 4.1 - Complex plane spectra for DSA® in  $1 \text{ mol dm}^{-3}$  NaCl, pH 2 at  $20 \text{ }^\circ\text{C}$  at different potentials (V vs NHE). The dots are the experimental data and the lines correspond to fitting to the proposed equivalent circuit model.



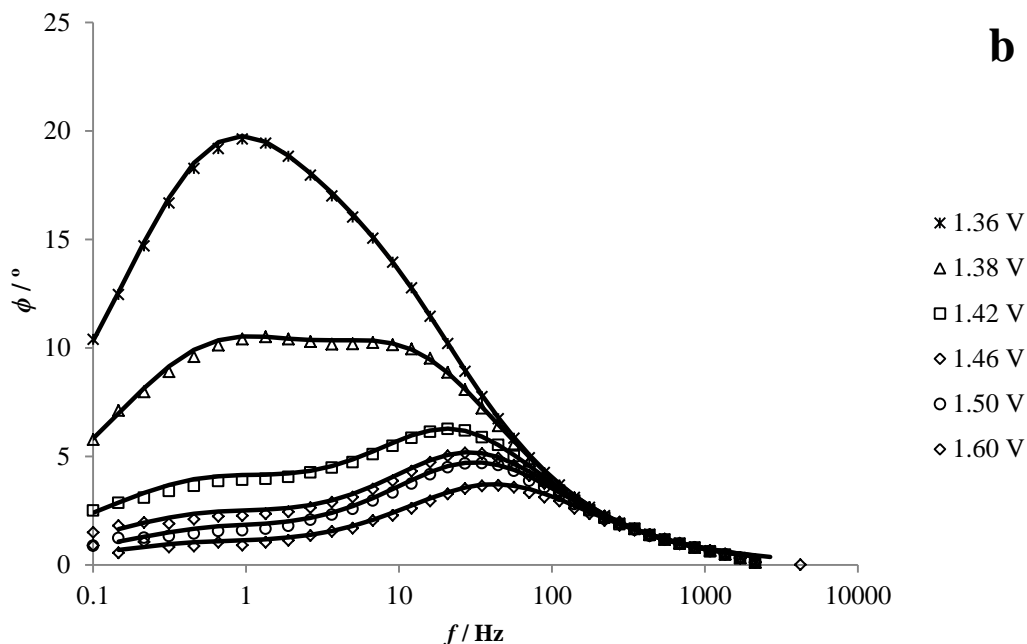


Figure 4.2 - Bode diagrams for DSA<sup>®</sup> in 1·mol dm<sup>-3</sup> NaCl, pH 2 at 20 °C at the same potentials as Figure 4.1. The dots are the experimental data and the lines correspond to fitting to the proposed equivalent circuit model. a) shows log (Z) vs log (f) and b) shows phase angle vs log (f)

The electrical equivalent circuits (EEC) used in the literature to fit the impedance spectra of DSA<sup>®</sup> anodes exhibiting two semicircles are shown in Figure 4.3.

The most commonly used model is EEC 1 [4, 24, 42-44]. This circuit comprises two RC parallel elements in series, one corresponding to the impedance of the coating ( $R_f$  and  $C_f$ ) and the other to the parallel contribution of the double layer capacitance ( $C_{dl}$ ) and charge transfer resistance ( $R_{ct}$ ) at the coating-solution interface. According to previous studies in which the effect of potential on the impedance was investigated [4, 45], the diameter of the semicircle at higher frequencies, assigned to the impedance of the film, was shown to be almost unaffected by the potential. In the present work, the diameter of both semicircles was shown to be dependent on the potential which suggests the semicircle at high frequencies is not related to the impedance of the coating. Since EEC 1, EEC 2 [46] and EEC 3 [38] include elements to describe impedance of the coating, none of these three EEC can be used to fit the impedance of the spectra obtained. The

electrode under study is coated with an oxide film, so that the inexistence of a semicircle related to the impedance of the coating suggests either a negligible contribution of the coating to the overall impedance or the overlapping of more than one phenomenon.

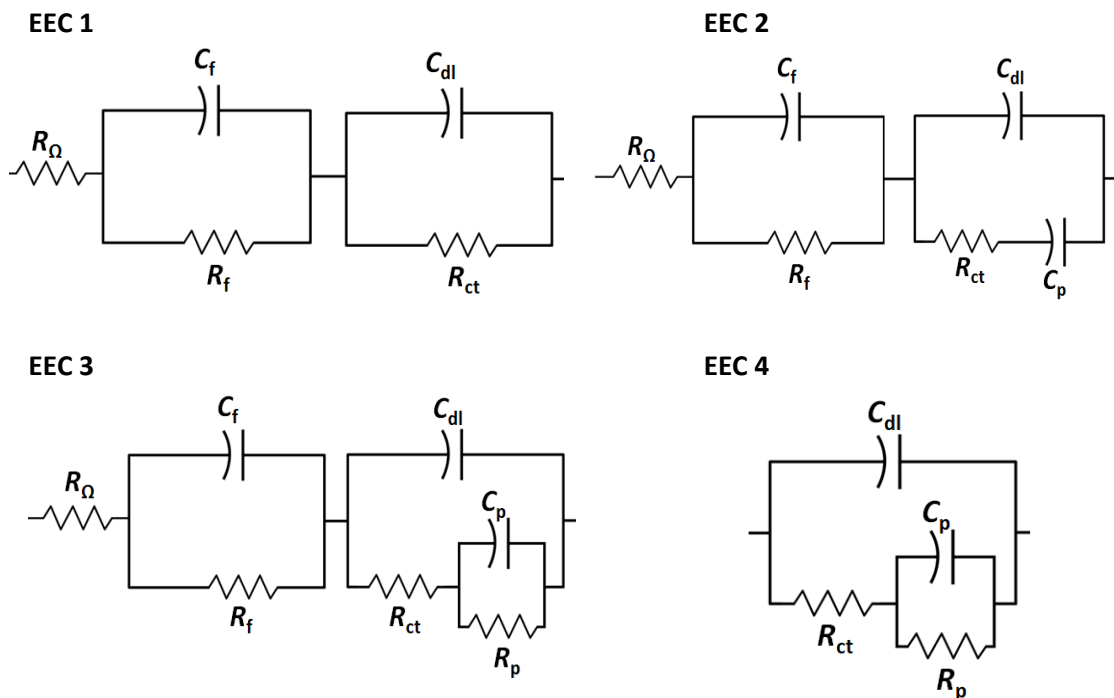


Figure 4.3 - Electrical equivalent circuits used to fit the impedance spectra of DSA<sup>®</sup> anodes

Since the impedance spectra of the DSA<sup>®</sup> anode does not show the impedance of the coating, the semicircle at higher frequencies can be assigned to the coating-solution interface represented by the double layer capacitance ( $C_{dl}$ ) and charge transfer resistance of the CIER ( $R_{ct}$ ) as has been mentioned in studies concerning the CIER on platinum anodes [32, 33]. The most likely process associated with the low frequency semicircle should be the adsorption/desorption of chlorine intermediates, as assigned by Li and co-workers [33], and Conway and Ping [32] for the CIER on reduced platinum electrodes.

Model EEC 4 has been widely employed to describe the impedance of electrochemical reactions with adsorbed intermediates and [29, 30, 32-37]. It is based on the equivalent circuit proposed by Armstrong [31] in parallel with the double layer

capacitance. EEC 4 leads to good fits of the impedance spectra (see Figure 4.1 and Figure 4.2); here  $R_p$  and  $C_p$  refer to the resistance and pseudocapacitance related to the adsorption/desorption of intermediates. Table 4.1 gives the parameters of model EEC 4 that best fit the impedance spectra at different potentials. The overpotential,  $\eta$ , was calculated by Equation 4.28.

$$\eta = E - E_{eq} \quad (4.28)$$

where  $E_{eq}$  is the equilibrium potential was determined experimentally and is 1.355 V.

The capacitors were replaced by constant phase elements (CPE) to describe the depression of the semicircles:  $Y_0$  is the magnitude of the CPE,  $n_1$  and  $n_2$  are the exponents of the double layer CPE and pseudocapacitance CPE, respectively, according to:

$$Z_{CPE} = \frac{1}{Y_0(j\omega)^n} \quad (4.29)$$

where  $j$  is the imaginary number and  $\omega$  is the characteristic frequency in  $\text{rad s}^{-1}$ .

The depression of the semicircles of the impedance spectra of DSA<sup>®</sup> anodes has often been often assigned to the roughness and high porosity of this type of electrodes [3, 4, 27].

**Table 4.1 - Parameters of EEC 4 obtained fitting the impedance spectra at different potentials**

$E$ vs NHE / V	$\eta$ / V	$R_{ct}/\Omega \text{ cm}^2$	$Y_{0,dl}/$ $\text{mF cm}^{-2} \text{ s}^{n-1}$	$n_1$	$R_p/\Omega \text{ cm}^2$	$Y_{0,p}/$ $\text{mF cm}^{-2} \text{ s}^{n-1}$	$n_2$
1.36	0.005	4.37	13.1	0.80	10.2	42	0.70
1.38	0.018	3.08	13.0	0.80	4.11	115	0.71
1.40	0.025	1.82	13.5	0.81	2.49	199	0.70
1.42	0.034	1.64	11.8	0.82	1.49	329	0.71
1.44	0.042	1.57	11.4	0.81	0.84	464	0.78
1.46	0.048	1.41	11.2	0.81	0.79	640	0.74
1.50	0.061	1.35	11.5	0.80	0.47	960	0.80
1.52	0.067	1.30	11.5	0.80	0.32	1040	0.85
1.54	0.073	1.26	12.4	0.79	0.33	1565	0.85
1.56	0.078	1.24	12.5	0.79	0.29	1365	0.88
1.58	0.083	1.12	12.7	0.78	0.27	1373	0.92
1.60	0.088	1.07	12.6	0.79	0.23	1895	0.84

The charge transfer resistance,  $R_{ct}$ , decreases as the potential increases, which is expected since the EIS experiments were carried out within the kinetically controlled region of potential. The small values of charge transfer resistance confirm the high catalytic activity of the DSA<sup>®</sup> for chlorine evolution. The low frequency resistance,  $R_p$ , decreases exponentially with increase in overpotential, in agreement with previous work [10, 30, 32, 34]. This behaviour could be expected since, according to the mechanism proposed, the adsorption/desorption phenomena are favoured by higher potentials.

The magnitude of the double layer CPE, from 11.2 to 13.5 mF cm<sup>-2</sup> s<sup>n-1</sup> is almost independent of the potential, and is in the same range as reported by other authors [4, 14, 27, 28, 46]. These values are much larger than the values expected for the double layer capacitance of compact and smooth electrode surfaces, which would be around 60 – 80 μF cm<sup>-2</sup> [47]. The values found for the exponent of both CPE,  $n_1$  and  $n_2$ , between 0.70 and 0.92 are in agreement with the literature [4, 24, 28, 38]. The deviation from an ideal capacitor ( $n = 1$ ) results from the non-uniform current distribution at the electrode due to the heterogeneity of the oxide coating.

Conversely to the double layer capacitance,  $Y_{0,p}$  is very sensitive to the overpotential. The values increase with increasing potential, although  $Y_{0,p}$  is expected to attain a maximum since equation 4.21 is quadratic [41].

Figure 4.4 shows simulations of the values of capacitance as a function of overpotential using the VHT model. As seen, a maximum value of the pseudocapacitance  $C_p$  occurs at around 0.120 V. At this potential, the dependence of the coverage on the potential is maximum. The values obtained from the fitting of the experimental data to EEC 4 (square dots in Figure 4.4) are fairly well adjusted by the VHT model, when the charge corresponding to full coverage,  $q_0$ , is set to 65 mC cm<sup>-2</sup>.

Parameter  $\tau$  is the time constant related to adsorption/desorption of the intermediates [29, 31]. Figure 4.4 shows that  $\tau$  peaks at around 40 mV overpotential. This behavior is similar to that exhibited by  $C_\phi$ , which peaks at ca. 50 mV. Concerning  $C_p$ , the shape of the curve is similar to that obtained for  $\tau$ , but it peaks at ca. 120 mV. Despite representing similar physical quantities,  $C_p$  and  $C_\phi$  do not have exactly the same meaning

[29, 30, 32]. According to Harrington and Conway [29], while  $C_\phi$  is the steady-state pseudocapacitance related exclusively to the coverage of the electrode (see Equation 4.16),  $C_p$ , which is the capacitance coupled with the resistance,  $R_p$ , is related to the adsorption phenomena, although its value does not have a direct physical meaning [29]. The chlorine coverage fraction,  $\theta$ , seems to converge to a plateau slightly above a value of 0.4.

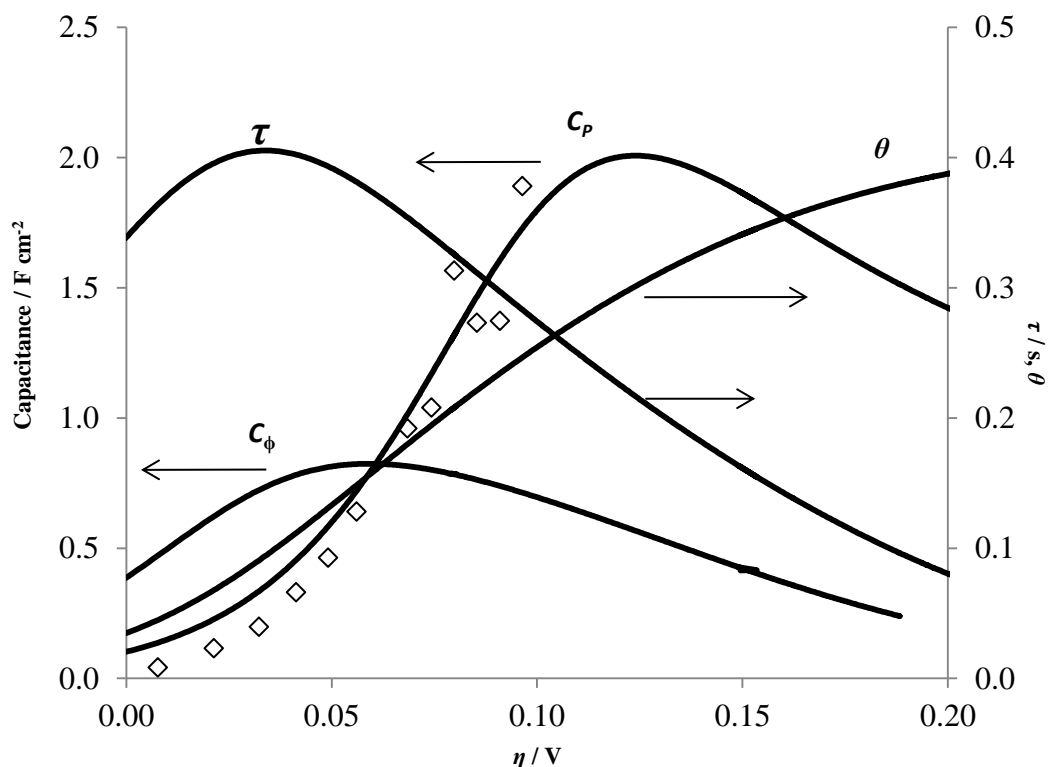
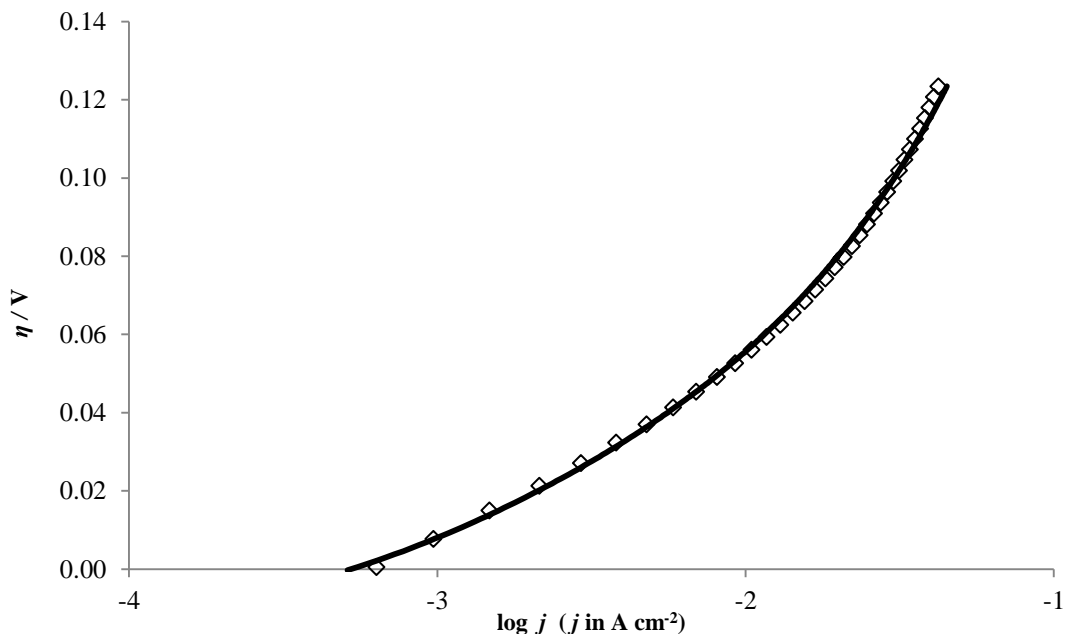


Figure 4.4 - Simulated curves  $\theta$  vs  $\eta$ ,  $C_\phi$  vs  $\eta$ ,  $\tau$  vs  $\eta$  and  $C_p$  vs  $\eta$  calculated from Equations 4.15, 4.16, 4.20 and 4.21, respectively. Dots represent the  $C_p$  vs  $\eta$  obtained from fitting the impedance spectra to EEC 4 model.

### Polarisation curves

The anodic polarisation curve obtained for the evolution of chlorine on the DSA<sup>®</sup>, as well as that corresponding to the developed kinetic model, is shown in Figure 4.5. The profile obtained is typical for recombination-controlled reactions [32, 48] and is similar to the curves obtained by Kuhn and Mortimer [49] and Gu [48], who studied RuO<sub>2</sub>-coated

titanium electrodes in similar electrolyte conditions ( $1 \text{ mol} \cdot \text{dm}^{-3} \text{ NaCl}$ ,  $20 \text{ }^\circ\text{C}$ ). The curved shape of the polarisation curve cannot be assigned to the ohmic drop since the ohmic contribution was subtracted. Experiments at different stirrer speeds did not lead to noticeable differences in the shape of the polarisation curve, and so mass-transfer limitations seem to be negligible.



**Figure 4.5 - Anodic polarisation curve obtained on DSA<sup>®</sup> anode in  $1 \text{ mol dm}^{-3} \text{ NaCl}$  at  $20 \text{ }^\circ\text{C}$ . Symbols represent the experimental values and the continuous line the kinetic model**

The fitting model uses the kinetic constants and symmetry factors that minimise Equation 4.27, based on the EIS characterization and polarization data. The values of the parameters obtained are shown in Table 4.2;  $k_2$  and  $k_3$  were found to be negligible, showing that the backward reactions of the Heyrovsky and Tafel steps (Equations 4.2 and 4.3) are irrelevant. The values of the rate constants of the second and third step ( $k_2 = 9.1 \times 10^{-8} \text{ mol cm}^{-2} \text{ s}^{-1}$  and  $k_3 = 1.2 \times 10^{-6} \text{ mol cm}^{-2} \text{ s}^{-1}$ ) suggest the co-existence of both Heyrovsky and Tafel steps during the CIER on DSA<sup>®</sup> within the overpotential range 0 mV to 100 mV. However, the contribution of the Tafel step is dominant since  $k_3 \approx 10 k_2$ . The values found

for the forward and backward rate constants of the initial, Volmer step ( $k_1 = 6.5 \times 10^{-8} \text{ mol cm}^{-2} \text{ s}^{-1}$  and  $k_{-1} = 1.6 \times 10^{-6} \text{ mol cm}^{-2} \text{ s}^{-1}$ ) support the equilibrium hypothesis for the first step of the mechanism with equilibrium constant,  $K_1 = 3.8 \times 10^{-2}$ . The symmetry factor of the Volmer step,  $\beta = 0.55$ , shows the almost perfect symmetry of the charge transfer in this step. The symmetry factor for the Heyrovsky step,  $\gamma = 0.31$ , shows that the perfect symmetry factor, i.e.  $\gamma = 0.50$ , normally assumed [30, 32] does not apply here. Based on our work, it can be concluded that the CIER on DSA<sup>®</sup> anodes is well described by the VHT mechanism with the Tafel step as the rate-determining step. Conversely to what was found by Gu [48], in the present study, the contribution of the Heyrovsky step cannot be neglected.

**Table 4.2 – Values of the rate constants and symmetry factors calculated for the individual steps for the CIER on a DSA<sup>®</sup>**

$k_1 / \text{mol cm}^{-2} \text{ s}^{-1}$	$k_{-1} / \text{mol cm}^{-2} \text{ s}^{-1}$	$k_2 / \text{mol cm}^{-2} \text{ s}^{-1}$	$k_3 / \text{mol cm}^{-2} \text{ s}^{-1}$	$\beta$	$\gamma$
$6.5 \times 10^{-8}$	$1.6 \times 10^{-6}$	$9.1 \times 10^{-8}$	$1.2 \times 10^{-6}$	0.55	0.31

### Mechanistic model validation

Figure 4.6 and Figure 4.7 show the resistance values obtained from the EEC vs the value calculated from mechanistic model.

Despite some differences between the values determined from the mechanistic model and the EEC, the proposed kinetic model reasonably describes both charge transfer resistance and low frequency resistance. The major difference between the model and the data obtained from the EEC is seen for the charge transfer resistance at lower potentials. At these potentials, the two semicircles of the spectra are not completely resolved, leading to large differences during the fitting to the EEC.

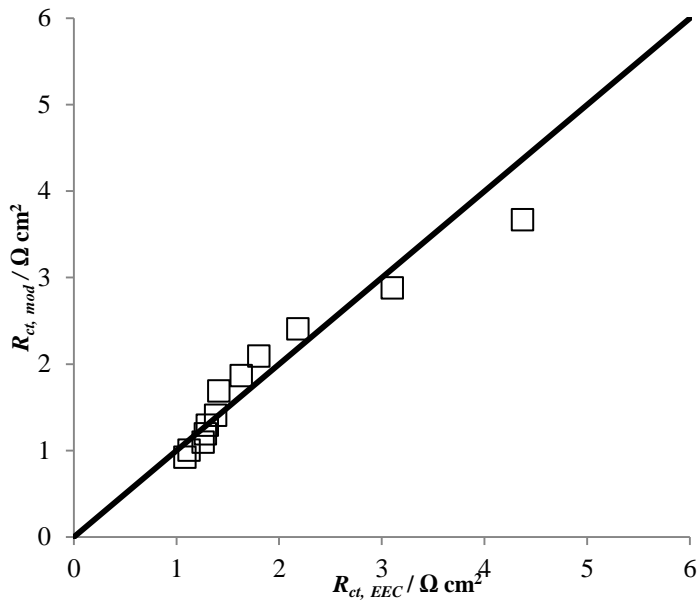


Figure 4.6 – Charge transfer resistance obtained from the kinetic model vs charge transfer resistance obtained from the EEC model.

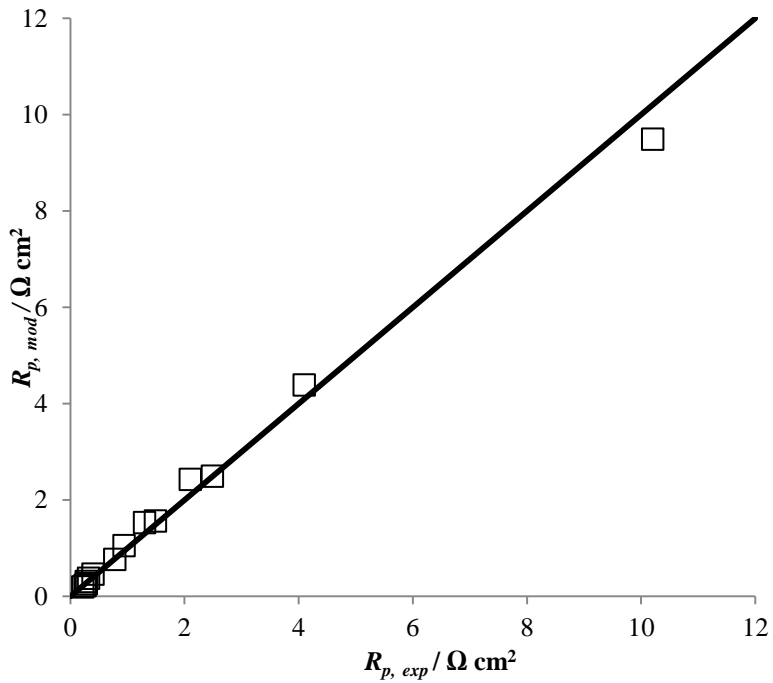


Figure 4.7 – Resistance associated with adsorption estimated from the kinetic model vs low frequency resistance obtained from the EEC model.

## 4.6 Conclusions

The combination of polarisation curves and EIS has been successfully employed to investigate the kinetics of the chlorine evolution reaction on DSA<sup>®</sup> anodes. EIS was shown to provide an important contribution to the study of the kinetics of the ClER since the shape of the impedance spectra seems to confirm the existence of chlorine intermediates, which are not detectable by polarisation curves. In order to include adsorption phenomena, impedance spectra were fitted to an electrical equivalent circuit based on Armstrong's equivalent circuit. A relation between the circuit elements and the kinetic parameters was validated for the system under study.

Our findings support, in the absence of mass transport limitations, a Volmer-Heyrovsky-Tafel mechanism with the Tafel step as rate-determining step to describe the evolution of chlorine on DSA<sup>®</sup> anodes.

## 4.7 References

1. O'Brien, T.F., T.V. Bommaraju, and F. Hine, *Handbook of chlor-alkali technology*. 2005, New York: Springer.
2. Trasatti, S., *Electrocatalysis: understanding the success of DSA (R)*. *Electrochimica Acta*, 2000. **45**(15-16): p. 2377-2385.
3. Panić, V.V., et al., *The effect of the addition of colloidal iridium oxide into sol-gel obtained titanium and ruthenium oxide coatings on titanium on their electrochemical properties*. *Physical Chemistry Chemical Physics*, 2010. **12**(27): p. 7521-7528.
4. Hoseinie, S.M., F. Ashrafizadeh, and M.H. Maddahi, *A Comparative Investigation of the Corrosion Behavior of RuO<sub>2</sub>-IrO<sub>2</sub>-TiO<sub>2</sub> Coated Titanium Anodes in Chloride Solutions*. *Journal of the Electrochemical Society*, 2010. **157**(4): p. E50-E56.
5. Kötz, R. and S. Stucki, *Stabilization of RuO<sub>2</sub> by IrO<sub>2</sub> for anodic oxygen evolution in acid media*. *Electrochimica Acta*, 1986. **31**(10): p. 1311-1316.
6. Panić, V.V., et al., *On the deactivation mechanism of RuO<sub>2</sub>-TiO<sub>2</sub>/Ti anodes prepared by the sol-gel procedure*. *Journal of Electroanalytical Chemistry*, 2005. **579**(1): p. 67-76.
7. Panić, V.V., et al., *Capacitive properties of RuO<sub>2</sub>-coated titanium electrodes prepared by the alkoxide ink procedure*. *Journal of Electroanalytical Chemistry*, 2007. **609**(2): p. 120-128.
8. Beer, H.B., Patent GB 1147442, (1965).
9. Trasatti, S. and G. Buzzanca, *Ruthenium dioxide: A new interesting electrode material. Solid state structure and electrochemical behaviour*. *Journal of Electroanalytical Chemistry and Interfacial Electrochemistry*, 1971. **29**(2): p. A1-A5.
10. Janssen, L.J.J., et al., *Mechanism of the chlorine evolution on a ruthenium oxide/titanium oxide electrode and on a ruthenium electrode*. *Electrochimica Acta*, 1977. **22**(10): p. 1093-1100.
11. Tilak, B.V., *Kinetics of chlorine evolution - comparative study*. *Journal of the Electrochemical Society*, 1979. **126**(8): p. 1343-1348.
12. Krishtalik, L.I., *Kinetics and mechanism of anodic chlorine and oxygen evolution reactions on transition-metal oxide electrodes*. *Electrochimica Acta*, 1981. **26**(3): p. 329-337.
13. Harrison, J.A., D.L. Caldwell, and R.E. White, *Electrocatalysis and the chlorine evolution reaction*. *Electrochimica Acta*, 1983. **28**(11): p. 1561-1568.
14. Denton, D.A., J.A. Harrison, and R.I. Knowles, *Chlorine evolution and reduction on RuO<sub>2</sub>/TiO<sub>2</sub> electrodes*. *Electrochimica Acta*, 1979. **24**(5): p. 521-527.
15. Consonni, V., et al., *Mechanism of chlorine evolution on oxide anodes - Study of pH effects*. *Journal of Electroanalytical Chemistry and Interfacial Electrochemistry*, 1987. **228**(1-2): p. 393-406.
16. Arikado, T., C. Iwakura, and H. Tamura, *Some oxide catalysts for anodic evolution of chlorine - reaction-mechanism and catalytic activity*. *Electrochimica Acta*, 1978. **23**(1): p. 9-15.

17. Faita, G. and G. Fiori, *Anodic discharge of chloride ions on oxide electrodes*. Journal of Applied Electrochemistry, 1972. **2**(1): p. 31-35.
18. Trasatti, S., *Progress in the understanding of the mechanism of chlorine evolution at oxide electrodes*. Electrochimica Acta, 1987. **32**(3): p. 369-382.
19. Panić, V.V., et al., *RuO<sub>2</sub>-TiO<sub>2</sub> coated titanium anodes obtained by the sol-gel procedure and their electrochemical behaviour in the chlorine evolution reaction*. Colloids and Surfaces A: Physicochemical and Engineering Aspects, 1999. **157**(1-3): p. 269-274.
20. Ferro, S. and A. De Battisti, *Electrocatalysis and Chlorine Evolution Reaction at Ruthenium Dioxide Deposited on Conductive Diamond*. The Journal of Physical Chemistry B, 2002. **106**(9): p. 2249-2254.
21. Fernández, J.L., M.R. Gennero de Chialvo, and A.C. Chialvo, *Kinetic study of the chlorine electrode reaction on Ti/RuO<sub>2</sub> through the polarisation resistance: Part III: proposal of a reaction mechanism*. Electrochimica Acta, 2002. **47**(7): p. 1145-1152.
22. Santana, M.H.P. and L.A. De Faria, *Oxygen and chlorine evolution on RuO<sub>2</sub> + TiO<sub>2</sub> + CeO<sub>2</sub> + Nb<sub>2</sub>O<sub>5</sub> mixed oxide electrodes*. Electrochimica Acta, 2006. **51**(17): p. 3578-3585.
23. Harrison, J.A., D.L. Caldwell, and R.E. White, *Electrocatalysis and the chlorine evolution reaction - II. Comparison of anode materials*. Electrochimica Acta, 1984. **29**(2): p. 203-209.
24. Hoseinieh, S.M. and F. Ashrafizadeh, *Influence of electrolyte composition on deactivation mechanism of a Ti/Ru<sub>0.25</sub>Ir<sub>0.25</sub>Ti<sub>0.5</sub>O<sub>2</sub> electrode*. Ionics, 2013. **19**(1): p. 113-125.
25. Zhou, X.L., et al., *Electrocatalytic activity and stability of Ti/IrO<sub>2</sub> + MnO<sub>2</sub> anode in 0.5 M NaCl solution*. Journal of Solid State Electrochemistry, 2010. **14**(7): p. 1213-1219.
26. Alves, V.A., L.A.d. Silva, and J.F.C. Boodts, *Surface characterisation of IrO<sub>2</sub>/TiO<sub>2</sub>/CeO<sub>2</sub> oxide electrodes and Faradaic impedance investigation of the oxygen evolution reaction from alkaline solution*. Electrochimica Acta, 1998. **44**(8-9): p. 1525-1534.
27. Alves, V.A., L.A.d. Silva, and J.F.C. Boodts, *Electrochemical impedance spectroscopic study of dimensionally stable anode corrosion*. Journal of Applied Electrochemistry, 1998. **28**(9): p. 899-905.
28. Xu, L.K. and J.D. Scantlebury, *A study on the deactivation of an IrO<sub>2</sub>-Ta<sub>2</sub>O<sub>5</sub> coated titanium anode*. Corrosion Science, 2003. **45**(12): p. 2729-2740.
29. Harrington, D.A. and B.E. Conway, *AC impedance of faradaic reactions involving electroadsorbed intermediates. 1. kinetic-theory*. Electrochimica Acta, 1987. **32**(12): p. 1703-1712.
30. Bai, L., D.A. Harrington, and B.E. Conway, *Behavior of overpotential deposited species in faradaic reactions. 2. AC impedance measurements on H<sub>2</sub> evolution kinetics at activated and unactivated Pt cathodes*. Electrochimica Acta, 1987. **32**(12): p. 1713-1731.

31. Armstrong, R.D. and M. Henderson, *Impedance plane display of a reaction with an adsorbed intermediate*. Journal of Electroanalytical Chemistry and Interfacial Electrochemistry, 1972. **39**(1): p. 81-90.
32. Conway, B.E. and P. Gu, *Evaluation of Cl adsorption in anodic Cl<sub>2</sub> evolution at Pt by means of impedance and potential-relaxation experiments. Influence of the state of surface oxidation of the Pt*. Journal of the Chemical Society-Faraday Transactions, 1991. **87**(17): p. 2705-2714.
33. Li, F.B., A.R. Hillman, and S.D. Lubetkin, *A new approach to the mechanism of chlorine evolution: Separate examination of the kinetic steps using ac impedance on a rotating thin ring electrode*. Electrochimica Acta, 1992. **37**(15): p. 2715-2723.
34. Jakšić, J.M., M.V. Vojnović, and N.V. Krstajić, *Kinetic analysis of hydrogen evolution at Ni-Mo alloy electrodes*. Electrochimica Acta, 2000. **45**(25-26): p. 4151-4158.
35. Krstajić, N., et al., *On the kinetics of the hydrogen evolution reaction on nickel in alkaline solution: Part I. The mechanism*. Journal of Electroanalytical Chemistry, 2001. **512**(1-2): p. 16-26.
36. Krstajić, N.V., S. Burojević, and L.M. Vračar, *The determination of kinetics parameters of the hydrogen evolution on Pd-Ni alloys by ac impedance*. International Journal of Hydrogen Energy, 2000. **25**(7): p. 635-641.
37. Krstajić, N.V., et al., *The determination of kinetics parameters of the hydrogen evolution on Ti - Ni alloys by ac impedance*. Electrochimica Acta, 1997. **42**(2): p. 323-330.
38. Hu, J.M., J.Q. Zhang, and C.N. Cao, *Oxygen evolution reaction on IrO<sub>2</sub>-based DSA® type electrodes: kinetics analysis of Tafel lines and EIS*. International Journal of Hydrogen Energy, 2004. **29**(8): p. 791-797.
39. Harrington, D.A., *The rate-determining step in electrochemical impedance spectroscopy*. Journal of Electroanalytical Chemistry, 2015. **737**: p. 30-36.
40. Harrington, D.A. and P. van den Driessche, *Mechanism and equivalent circuits in electrochemical impedance spectroscopy*. Electrochimica Acta, 2011. **56**(23): p. 8005-8013.
41. Gileadi, E. and B.E. Conway, *Kinetic Theory of Adsorption of Intermediates in Electrochemical Catalysis*. The Journal of Chemical Physics, 1963. **39**(12): p. 3420-3430.
42. Silva, L.M.d., L.A.d. Faria, and J.F.C. Boodts, *Electrochemical impedance spectroscopic (EIS) investigation of the deactivation mechanism, surface and electrocatalytic properties of Ti/RuO<sub>2</sub>(x)+Co<sub>3</sub>O<sub>4</sub>(1-x) electrodes*. Journal of Electroanalytical Chemistry, 2002. **532**(1-2): p. 141-150.
43. Lassali, T.A.F., J.F.C. Boodts, and L.O.S. Bulhões, *Faradaic impedance investigation of the deactivation mechanism of Ir-based ceramic oxides containing TiO<sub>2</sub> and SnO<sub>2</sub>*. Journal of Applied Electrochemistry, 2000. **30**(5): p. 625-634.
44. Silva, L.A.d., et al., *Oxygen evolution in acid solution on IrO<sub>2</sub> + TiO<sub>2</sub> ceramic films. A study by impedance, voltammetry and SEM*. Electrochimica Acta, 1997. **42**(2): p. 271-281.

45. Ye, Z.-G., H.-M. Meng, and D.-B. Sun, *Electrochemical impedance spectroscopic (EIS) investigation of the oxygen evolution reaction mechanism of Ti/IrO<sub>2</sub> + MnO<sub>2</sub> electrodes in 0.5 M H<sub>2</sub>SO<sub>4</sub> solution*. Journal of Electroanalytical Chemistry, 2008. **621**(1): p. 49-54.
46. Ribeiro, J. and A.R. de Andrade, *Investigation of the electrical properties, charging process, and passivation of RuO<sub>2</sub>-Ta<sub>2</sub>O<sub>5</sub> oxide films*. Journal of Electroanalytical Chemistry, 2006. **592**(2): p. 153-162.
47. Lassali, T.A.F., J.F.C. Boodts, and L.O.S. Bulhões, *Charging processes and electrocatalytic properties of IrO<sub>2</sub>/TiO<sub>2</sub>/SnO<sub>2</sub> oxide films investigated by in situ AC impedance measurements*. Electrochimica Acta, 1999. **44**(24): p. 4203-4216.
48. Gu, P., *Behavior of the adsorbed Cl<sup>-</sup> intermediate in electrocatalysis of anodic Cl<sub>2</sub> evolution at oxide film surfaces at Pt and Ru*. 1990, University of Ottawa: Ottawa.
49. Kuhn, A.T. and C.J. Mortimer, *The Kinetics of Chlorine Evolution and Reduction on Titanium-Supported Metal Oxides Especially RuO<sub>2</sub> and IrO<sub>2</sub>*. Journal of The Electrochemical Society, 1973. **120**(2): p. 231-236.

## **5 On the deactivation mechanisms of a TiO<sub>2</sub>-RuO<sub>2</sub>-IrO<sub>2</sub> coated DSA® anode during chlorine evolution reaction**

### **5.1 Abstract**

The mechanisms of deactivation of TiO<sub>2</sub>-RuO<sub>2</sub>-IrO<sub>2</sub> coated DSA® anode during chlorine evolution reaction were studied. An aging experiment was carried out in 5 mol dm<sup>-3</sup> NaCl solution, pH = 2 and at 353 K during more than 4600 h. The history of the anode performance was followed by cyclic voltammetry, electrochemical impedance spectroscopy and surface characterization techniques (scanning electron microscopy, energy dispersive X-Ray and X-Ray photoelectron spectroscopy). The results obtained suggest the existence of three deactivation mechanisms – coating erosion, selective dissolution of ruthenium and iridium from the coating and the growth of a TiO<sub>2</sub> passive layer at the coating-substrate interface. The growth of a TiO<sub>2</sub> layer was identified as the main deactivation mechanism and was attributed to the oxidation of the titanium substrate due to the penetration of the electrolyte into the pores of the DSA® anode. The appearance of a semicircle at high frequency in the impedance spectra marked the beginning of the loss of anode activity and shows the relevance of EIS for the study of this type of anodes.

## 5.2 Introduction

Since the first patent filled by Beer in 1967 [1] dimensionally stable anodes (DSA<sup>®</sup>) became considered the most used electrodes for chlorine anodic evolution in chlor-alkali cells [2, 3]. The DSA<sup>®</sup> electrode consists of titanium substrates coated by a mixture of oxides with at least one of the oxides containing a noble metal (platinum, ruthenium, palladium, osmium, rhodium or iridium) and other metals from the group of titanium, tantalum, zirconium, niobium [1]. The original coating composition for the chlorine evolution reaction was a mixture of RuO<sub>2</sub> and TiO<sub>2</sub> [2, 4-6], which is applied on a titanium substrate by the thermal decomposition method [2, 4]. Nowadays, the composition and preparation of the electrodes used in industrial cells still remains essentially the same. The main improvement has been the addition of IrO<sub>2</sub> to the coating for reducing the dissolution of ruthenium species and extending the service life of the anode [2, 4, 7, 8].

The excellent electrocatalytic properties combined with high stability make DSA<sup>®</sup> anodes, even more than 45 years after its invention, the state of art of anodes for the chlor-alkali industry. DSA<sup>®</sup> anodes were considered one of the most important landmarks in the electrochemistry field [2, 3]. Its application in the industrial production of chlorine is undisputable, and the use of DSA<sup>®</sup> anodes in other fields like oxygen production [9-11] or wastewater treatment [12-14] has been a subject of increasing interest. Regarding the chlorine evolution reaction, the research conducted in the field of DSA<sup>®</sup> anodes has been focussed towards either introducing small changes in the coating composition [15-17] or testing new techniques for the preparation of the electrodes [5, 6, 18-20].

Although the service life of these electrodes is believed to be around 8 to 10 years [4, 21] their replacement or recoating is an expensive operation since noble metals are employed. Hence, the lifetime of the DSA<sup>®</sup> anodes is a relevant topic that has been addressed in a number of reports in recent years [3, 5-8, 22-36]. These reports cover the development of techniques to evaluate anode performance as well as the investigation of new coating compositions to improve the stability and extend the lifetime of the DSA<sup>®</sup> anodes. Having the extension of the lifetime of the anodes as a goal, the identification of the deactivation mechanisms of the anode is of critical relevance. In most of the previous

studies, different mechanisms to explain the deactivation of the DSA<sup>®</sup> anodes have been proposed [3, 5-8, 18, 24, 29, 30, 32-35]. The loss of activity of DSA<sup>®</sup> anodes is attributed to three phenomena: the erosion of the coating, the dissolution of the noble metals and the formation of a passive TiO<sub>2</sub> layer in between the interface substrate-coating. Nevertheless, the combination of more than one of the previous phenomena has been often reported [23]. The experiments have been carried out under different operation conditions (electrolyte, current density and temperature) with in-house-prepared anodes, made following synthesis methods and with dissimilar compositions. Therefore, a large range of failure times, from about 20 min [23] to 1700 h [37] are reported. These times are considerably lower than what is expected for industrial anodes during normal operation conditions. Taking into account the long life of the DSA<sup>®</sup> anodes, the study of the deactivation phenomena would be unfeasible in a reasonable time period if the electrochemical cell is operated under nominal industrial conditions. Accelerated life tests (ALT) have been developed to increase the rate of the deactivation to attain a significant loss of activity in a reasonable period of time [31, 38]. This accelerated deactivation is achieved by exposing the electrodes to harsh operation conditions. The typical approach consists in increasing the current density up to 2 A cm<sup>-2</sup> [3] or by using electrolytes that increase the deactivation rate of the coating, such as low concentration sodium chloride solution [5, 7, 8] or strong acids like H<sub>2</sub>SO<sub>4</sub> [29, 31] or HClO<sub>4</sub> [5, 30].

Bearing in mind that these tests aim to mimic and to intensify the phenomena occurring during the normal operation of the electrode, they should ensure that the manipulation of the operation variables does not add a new degradation pathway. Hence, if it is intended to evaluate the performance of DSA<sup>®</sup> anodes for the chlorine evolution reaction, the ALT should be carried out in sodium chloride solutions [38]. Indeed, different authors have pointed out that the choice of the electrolyte is critical to the degradation mechanism [31, 36, 38]. In a recent article published by Hoseinieh and co-workers [7], it has been reported that for identical DSA<sup>®</sup> anodes coated with RuO<sub>2</sub>-IrO<sub>2</sub>-TiO<sub>2</sub> the ageing phenomena are dependent on the electrolyte used. While in NaCl solutions the main deactivation processed was assigned to the growth of an insulating TiO<sub>2</sub> layer at the

coating-substrate interface, for the anode tested in  $\text{H}_2\text{SO}_4$ , the passivation of the electrode resulted from the dissolution of ruthenium and iridium.

Even for the diluted sodium chloride solution used in previous work [5-8], the low chloride content reduces the chlorine / oxygen ratio [5] which could promote deactivation related to oxygen that would not be present in the industrial anodes. To overcome this limitation, in this work the deactivation of a commercial DSA<sup>®</sup> anode ( $\text{RuO}_2\text{-IrO}_2\text{-TiO}_2$  coated titanium) was investigated during ALT in  $5 \text{ mol dm}^{-3}$  NaCl solution. The electrode state was evaluated regularly by electrochemical characterisation techniques (cyclic voltammetry (CV), polarization curves and electrochemical impedance spectroscopy (EIS)), scanning electron microscopy (SEM) and elemental analysis techniques (energy-dispersive X-Ray analysis (EDS) and X-Ray photoelectron Spectroscopy (XPS)). The results obtained from these analytical techniques allowed proposing a mechanism to describe the deactivation mechanism of DSA<sup>®</sup> anodes in highly concentrated sodium chloride solution. The results of the current study are relevant for the prediction of the ageing time of industrial DSA<sup>®</sup> anodes used for chlorine production.

## 5.3 Experimental

### Electrodes

A  $2.0 \text{ cm}^2$  DSA<sup>®</sup> commercial anode made of  $\text{RuO}_2\text{-IrO}_2\text{-TiO}_2$  coated titanium from De Nora was used as working electrode and a platinum mesh was used as counter electrode; an Ag/AgCl electrode saturated with KCl was used as reference electrode. Exploratory experiments showed the need for preconditioning the working electrode to obtain reproducible characteristic curves and impedance spectra, as suggested elsewhere [39, 40]. The pre-treatment of the anode included two steps: (i) 10 potential cycles from 0.0 V vs NHE to +1.2 V vs NHE at  $50 \text{ mV}\cdot\text{s}^{-1}$  and (ii) 300 s polarisation at +0.5 V vs NHE.

## Reagents

Sodium chloride solutions were prepared from a high purity stock 5 mol dm<sup>-3</sup> solution of NaCl. The initial pH was set to 2 using industrial grade HCl 33 wt. %. Both solutions were supplied by CUF-QI (Portugal).

## Electrochemical cell

The electrochemical cell used for the accelerated ageing test and for the characterisation of the anode is described in Chapter 3.

## Characterisation techniques

The accelerated ageing test was carried out between 70 °C and 80 °C in potentiostatic mode and the power source was a Zahner PP 210. The potential was set to be 7 V vs the counter electrode over the first 1850 h of the test. From this time onwards, the potential applied was 8 V vs the counter electrode. The electrochemical measurements were performed at 20 °C using an IM6ex Zahner Electrochemical station. Before characterising the electrode the ageing test was interrupted, the cell and the electrode were rinsed with water. Cyclic voltammetry experiments were run between 0.0 V vs NHE to +1.2 V vs NHE, covering the capacitive / pseudocapacitive region of the electrode. Ten potential cycles were performed at a scan rate of 50 mV s<sup>-1</sup>. The impedance spectra were obtained in potentiostatic mode with a 10 mV rms amplitude perturbation in the frequency range 65 kHz to 100 mHz. At higher frequencies 10 data points per decade, each one integrating 10 cycles, were recorded; below 66 Hz, the impedance was measured at 5 data points per decade, each one integrating the 5 cycles. Impedance spectra were recorded in the capacitive region of the electrode, 0.5 V vs NHE, and in the chlorine evolution potential region, 1.4 V vs NHE; The spectra were fitted to electrical equivalent circuits using Zview<sup>®</sup> 3.1c (Scribner, USA). The cell was stirred at 500 rpm during EIS measurements. The pH of the electrolyte solution was measured using a WTW Microprocessor pH-Meter pH 3000. The temperature was controlled using a HUBER CC1 water circulation bath.

SEM and EDS analysis were carried out with a electronic microscope model Hitachi SU-70 and XPS analysis was carried out with a Kratos Axis Ultra has equipment. The atomic compositions reported in this work result from the average value from four 0.4 mm<sup>2</sup> areas for the EDS and two 0.12 mm<sup>2</sup> areas for XPS.

## 5.4 Discussion and results

### Accelerated ageing test

Figure 5.1 shows the current density history at the DSA<sup>®</sup> anode during the ageing test in 5 mol dm<sup>-3</sup> NaCl, in potentiostatic mode. This experiment can be divided in three stages. Over the first stage, up to 2950 h, the current was roughly constant, although a current density step, from ca. 1.6 A cm<sup>-2</sup> to ca. 2.0 A cm<sup>-2</sup> occurred at 1850 h due to the potential increase from 7 V to 8 V vs the counter electrode. Between 2950 h and 3250 h, the current decreased suddenly to 1.2 A cm<sup>-2</sup>. This behaviour may suggest reduction of the electrode activity; however, during the interruption for characterisation at 3250 h it was found that the DSA<sup>®</sup> anode was partially coated with precipitated sodium chloride. After resuming the experiment, the current density was again ca. 2 A cm<sup>-2</sup>. In the last stage, from 3300 h up to the end of the test at 4600 h, the current decreased from 2.0 A cm<sup>-2</sup> to 1.0 A cm<sup>-2</sup>. From 3300 h to 3900 h the current density decrease was essentially linear, whilst from 3900 h to 4450 h, the current density remained at ca. 1.16 A cm<sup>-2</sup>, decreasing again to ca. 1.0 A cm<sup>-2</sup> at 4600 h.

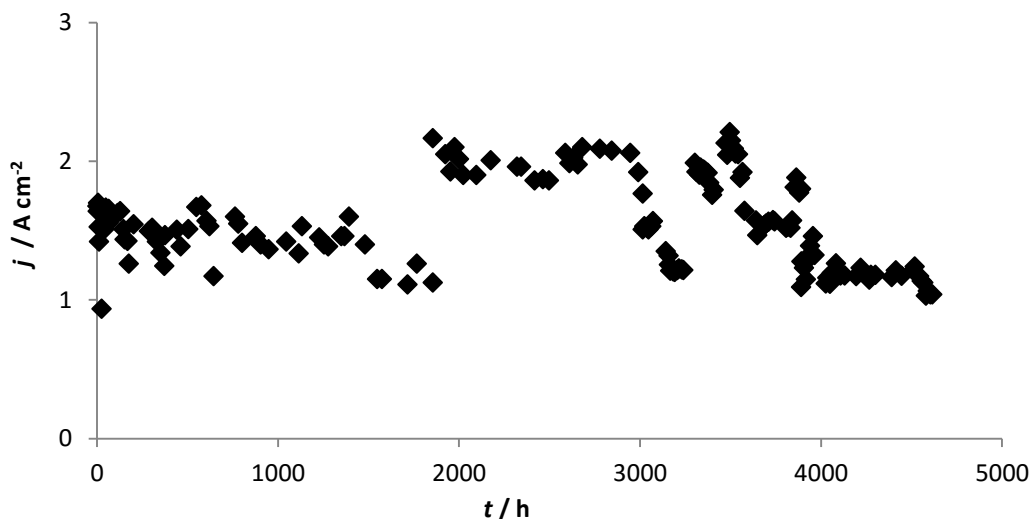


Figure 5.1 – Current density history during the accelerated ageing test of DSA® anode in 5 mol dm<sup>-3</sup> NaCl

### Cyclic Voltammetry

Figure 5.2 shows representative cyclic voltammograms recorded over the ageing period of time of the DSA® anode. From 216 h on, the cyclic voltammograms exhibit faradaic currents in the potential range 0.4 V to 1.0 V vs NHE associated with the pseudocapacitive processes occurring in the coating. Instead of a single current peak, a broad band is seen due to the existence of several metallic transitions of the iridium and ruthenium. This is the characteristic shape of the voltammograms of DSA® anodes [5, 7, 30]. However, the voltammograms recorded during the first 216 h are significantly different and do not exhibit faradaic currents. These voltammograms present a featureless shape typical of capacitive systems. A similar voltammetric profile was reported by Jovanović and co-workers for RuO<sub>2</sub>-TiO<sub>2</sub> DSA® anodes in which the coating was deposited in layers and the outer layer was rich in TiO<sub>2</sub> [41]. This could suggest that during the initial hours of the ageing test, the TiO<sub>2</sub> is probably in excess or more concentrated in the outer layers of the coating, masking the iridium and ruthenium reactions. Although the DSA® anode under study is a commercial sample and no details about the preparation methods are supplied, this type of anode is typically prepared by thermal decomposition methods [4, 5]. According to different studies in which the DSA® anodes were prepared by thermal

decomposition methods [7, 29], the coating is deposited by contacting the titanium substrate with a mixture of precursors of the different oxides to be applied. Since titanium dioxide ( $4.23 \text{ g cm}^{-3}$ ) [42] is less dense than ruthenium oxide ( $6.97 \text{ g cm}^{-3}$ ) [42], and iridium oxide ( $11.7 \text{ g cm}^{-3}$ ) [42], it is expected that titanium dioxide accumulates at the outer surface of the coating.

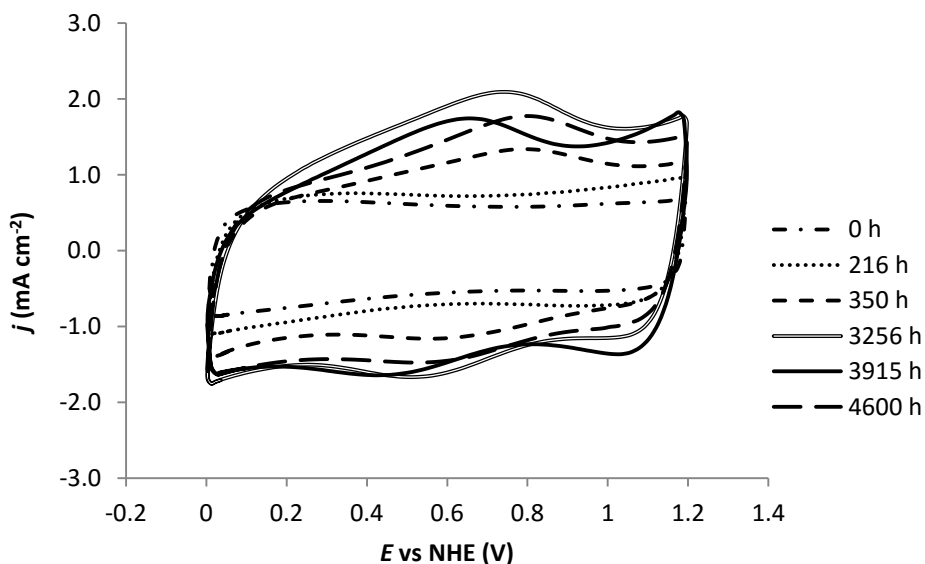


Figure 5.2 -Cyclic voltammograms obtained at different ageing times of DSA® anode in  $0.5 \text{ mol dm}^{-3} \text{ NaCl}$ ,  $\nu = 50 \text{ mV s}^{-1}$ ,  $20 \text{ }^\circ\text{C}$

Figure 5.3 shows the anodic voltammetric charge history during the aging experiment. The anodic voltammetric charge was calculated by integrating the anodic current density. During the initial 463 h, the anodic voltammetric charge exhibited a steady increase, suggesting a highly active electrode. The increase in the anode activity should be related to the penetration of the electrolyte in the pores and the contact with the iridium and ruthenium electroactive metals in the inner region of the electrode. Since the electroactive area is higher, larger current densities are seen. Over the initial 463 h, the anodic charge increases linearly from  $15 \text{ mC cm}^{-2}$  to  $25 \text{ mC cm}^{-2}$ , before increasing slightly until  $28 \text{ mC cm}^{-2}$ , reached at 3015 h. At 3256 h and 3586 h, significantly larger

voltammetric charges are recorded, respectively 35 and 38  $\text{mC cm}^{-2}$ . At this time, all the electroactive area of the coating was probably exposed to the electrolyte and the maximum anodic voltammetric charge was obtained. At 3915 h, the voltammetric charge was reduced to values around 29  $\text{mC cm}^{-2}$  and from, this point on, the voltammetry charge profile shows a decreasing trend, reaching 26  $\text{mC cm}^{-2}$  at 4600 h. These results follow the same trend as the current density (Figure 5.1), suggesting reduction of the activity of the DSA<sup>®</sup> anode after ca. 3586 h.

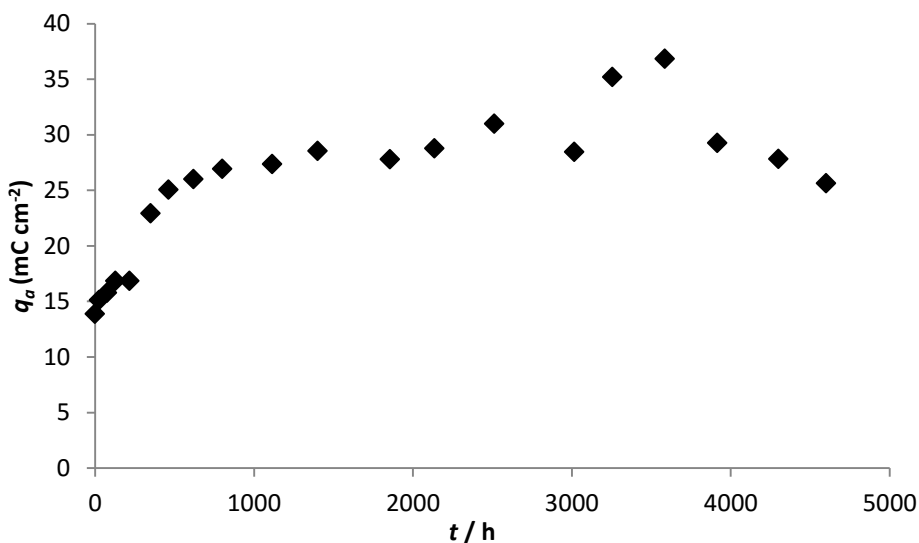
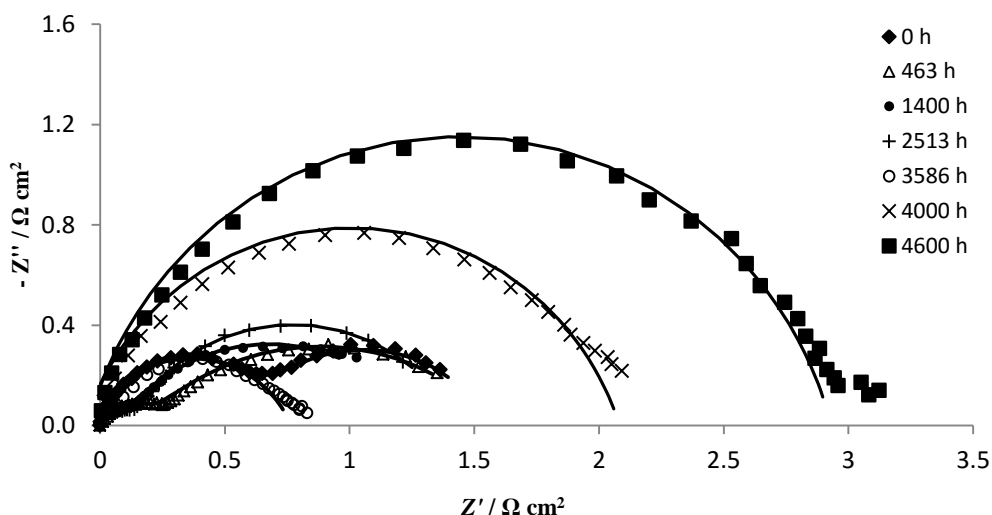


Figure 5.3 – Anodic voltammetric charge of the DSA<sup>®</sup> anode over the time,  $\nu = 50 \text{ mV s}^{-1}$ .

### Electrochemical impedance spectroscopy

The electrochemical impedance spectroscopy of the DSA<sup>®</sup> was evaluated using a 5.0  $\text{mol dm}^{-3}$  NaCl aqueous solution at 0.5 V and 1.4 V vs NHE. Figure 5.4 shows the impedance spectra in the complex plane recorded during the ageing test of the DSA<sup>®</sup> anode. The spectra recorded during the first 2523 h exhibited two semicircles, while at longer ageing times only one larger semicircle at higher frequencies can be seen. These findings are the opposite to those found in several articles addressing the electrochemical activity of DSA<sup>®</sup> over the ageing test. Articles published in recent years [3, 5, 7, 8, 24, 29, 30] show that, at

the beginning of the test, only one well-defined semicircle is visible and that a second semicircle arises at higher frequencies as the ageing test progresses. The semicircle at higher frequencies has been assigned to the oxide properties, while the semicircle at lower frequencies has been attributed to the double layer capacitance,  $C_{dl}$ , and charge transfer resistance,  $R_{ct}$ . However, our previous study (Chapter 4) shows that the semicircles of the impedance spectra for this DSA<sup>®</sup> anode did not correspond to the phenomena reported in the literature. According to our previous findings, the impedance spectra obtained for fresh anodes show a semicircle at higher frequencies (ca. 100 Hz) related to the double layer capacitance and charge transfer resistance. In addition, a semicircle at lower frequencies is observed and is assigned to a pseudocapacitance originated by the adsorption and desorption of chloride intermediates during the chlorine evolution reaction.



**Figure 5.4 - Complex plane spectra for DSA<sup>®</sup> anode in 5 mol dm<sup>-3</sup> NaCl, pH 2 at 20 °C at 1.4 V vs NHE, recorded at different times of the ageing test. The dots are the experimental data and the lines correspond to fitting to the proposed electrical equivalent circuit model.**

To evidence the role of the pseudocapacitance of the electrode, the electrical equivalent circuit (EEC) used to fit the impedance of spectra obtained over the first 3000 h of ageing is the one presented in Figure 5.5 a in which  $C_p$  is the pseudocapacitance and  $R_p$

is the associated resistance. Spectra recorded after 3000 h show a well-resolved semicircle at higher frequencies (1000 to 10000 Hz). Since this frequency range does not match with the range corresponding to the semicircles obtained during the first stage (up to 3000 h), the physical phenomenon described by this semicircle between 3000 h and the end of test, 4600 h, should not be related to chlorine evolution. These last spectra exhibit noise in the low frequency region that made the fitting in this region unfeasible. The EEC used to fit the impedance of these spectra is the simplified Randles Circuit shown in Figure 5.5 b in which  $C_{dl}$  and  $R_{ct}$  are respectively the capacitance and the resistance related to processes at higher frequencies in spectra recorded after 3000 h of testing. CPE were used instead of ideal capacitors to describe the porous nature of DSA<sup>®</sup> anodes [7].

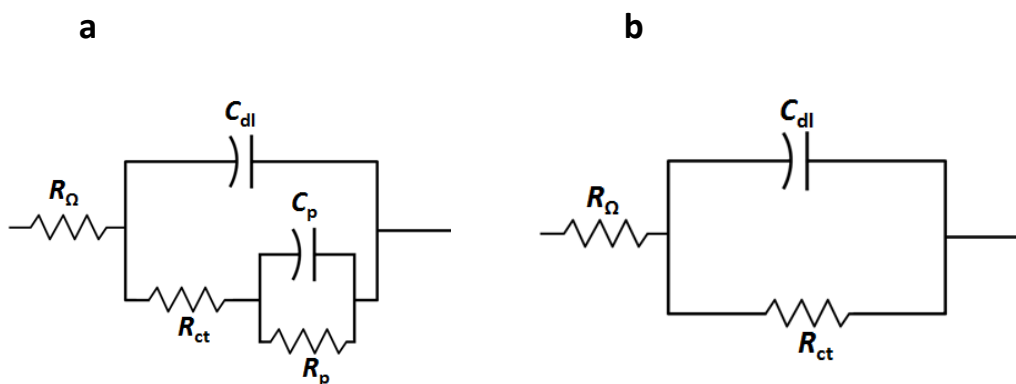


**Figure 5.5 - EEC used to fit the impedance of the DSA<sup>®</sup> recorded at 1.4 V vs NHE at different stages of the ageing test. a – EEC used to fit the spectra recorded over the first 3000 h of the test; b – EEC used to fit the impedance spectra recorded from 3586 h onwards**

The differences in the phenomena detected by impedance obtained before and after 3000 h are clearly visible in Figure 5.6, which displays the spectra from Figure 5.4 as the phase angle vs. frequency. Two spectra, at 76 h and 128 h, were added to make clearer the trend of the phase angle at intermediate frequencies (ca. 100 Hz). The phase angle of this semicircle is  $-3.9^\circ$  at the beginning of the tests, decreasing its absolute value up to  $-2.2^\circ$  at 463 h. The first time the phase angle at frequencies higher than 1000 Hz was identified was at 3586 h, with a value of  $-3.2^\circ$ . The following impedance measurements showed an

increase in the absolute value of the phase angle, being  $-8.4^\circ$  at 4000 h and  $-13.0^\circ$  at 4600 h. The increasing of the phase angle and the growing of the semicircle diameter at frequencies around 10 000 Hz for longer ageing times, have been reported and are assigned to deactivation of the DSA<sup>®</sup> anode [3, 5, 30, 31, 43, 44]. Most of these studies relate this phenomenon at higher frequencies to the formation of a passive  $\text{TiO}_2$  layer between substrate and coating due to substrate oxidation [5, 8, 30, 44], although others attribute the semicircle at high frequencies to the selective loss of electroactive species (ruthenium or/and iridium) [45].

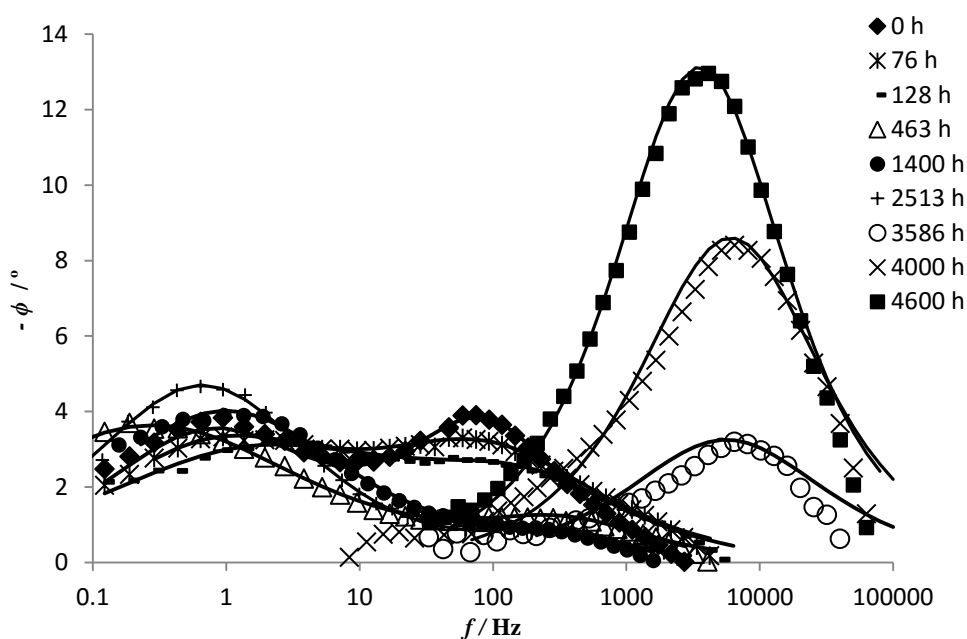
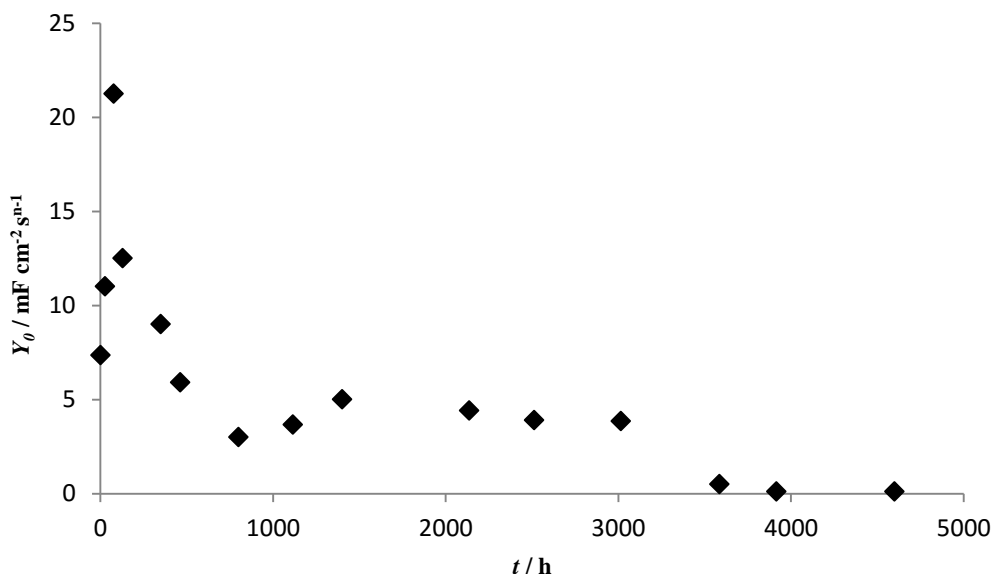


Figure 5.6 - Phase angle obtained from spectra in Figure 5.4.

The magnitude of the constant phase element (CPE),  $Y_0$ , used to fit the high frequency impedance is plotted in Figure 5.7 as a function of time. A CPE was used instead an ideal capacitor to describe the non-uniform current density on the DSA<sup>®</sup> due to the roughness and porous nature of this type of electrodes [3, 7]. For the first 3000 h,  $Y_0$  represents the double layer capacitance in parallel with  $R_{ct}$  (EEC in Figure 5.5 a). From 3000 h onwards,  $Y_0$  is the capacitance at higher frequencies (10000 Hz) assigned to anode deactivation phenomena (EEC in Figure 5.5 b). In the spectra recorded from 3000 h

onwards, the semicircles related to chlorine evolution were probably overlapped by the much more prominent semicircle attributed to deactivation of the anode.



**Figure 5.7 - Evolution of the magnitude of the high frequency CPE with the ageing time of DSA® anode in 5 mol dm<sup>-3</sup> NaCl**

At the beginning of the ageing test, the magnitude of the CPE was  $7.4 \text{ mF cm}^{-2} \text{ s}^{n-1}$ . The following measurements, at 26 h and 76 h, show an increase in the CPE value up to  $21 \text{ mF cm}^{-2} \text{ s}^{n-1}$ . However, this last value could be overestimated since the CPE exponent,  $n$ , obtained at 76 h, 0.67, is significantly lower than that obtained beforehand, i.e. 0.87 and 0.79 at 0 h and 26 h, respectively. At 128 h the fitted CPE exponent was 0.74 and the CPE magnitude was  $12.5 \text{ mF cm}^{-2} \text{ s}^{n-1}$ , which are closer to those obtained at 26h. At this time the CPE exponent was 0.79 and the CPE was  $11.0 \text{ mF cm}^{-2} \text{ s}^{n-1}$ . Even though analysis of the CPE magnitude and exponent cannot be performed independently, the history of the CPE magnitude suggests that the anode undergoes an activation process in the initial phase of the test that is likely to be related to the penetration and access of the electrolyte into the inner parts of the DSA® anode. The activation stage is followed by a reduction of the CPE magnitude, reaching a value of  $3.1 \text{ mF cm}^{-2} \text{ s}^{n-1}$  at 800 h. This decrease suggests a reduction of the electrode active area as a consequence of the ageing of the DSA® anode [3, 5, 8, 29-

31]. From 800 h onwards, the magnitude of the CPE seems to attain a plateau at ca.  $4 \text{ mF cm}^{-2} \text{ s}^{n-1}$  up to 3000 h. Xu and Scantlebury [3] reported a similar trend in their work and, based on work published by Krýsa and co-workers [46], assign this levelling out of the CPE magnitude to the reduction of the rate of iridium dissolution. According to Krýsa and co-workers [46], the iridium dissolution rate is maximum at the beginning of the ageing test and then stabilizes at values up to two orders of magnitude lower. The reduction of the dissolution rate should be the cause of the stabilization of  $Y_0$ . From 800 h to 3000 h, the exponent of the CPE was 1, which means that the double layer capacitance resembles an ideal capacitor. For longer times, the high frequency capacitance is no longer assigned to the double layer capacitance but to the deactivation process that leads to the reduction of the coating activity. The low CPE values found, from  $0.5 \text{ mF cm}^{-2} \text{ s}^{n-1}$  at 3586 h to  $0.1 \text{ mF cm}^{-2} \text{ s}^{n-1}$  at 4600 h, confirm that the electrochemical state of the electrode changed significantly, which is probably related to deactivation processes. The abrupt decrease of the capacitance values indicates the formation of a passive  $\text{TiO}_2$  layer as the most likely cause of the deactivation of the DSA<sup>®</sup> [3, 29].

Figure 5.8 shows the high frequency resistance history ( $R_{ct}$  for the first 3000 h – EEC in Figure 5.5 a; for longer ageing times – ECC in Figure 5.5 b). Globally, the resistance history goes in the opposite direction to capacitance. From the beginning of the test up to 350 h, the resistance decreases due to electrolyte penetration in the pores of the anode. This corroborates the anodic voltammetric charge results which show an abrupt increase of the DSA<sup>®</sup> anode activity. From 350 h to 3000 h, the resistance stabilizes, in agreement with the results for the capacitance and anodic voltammetric charge evolution. The increasing trend from 3000 h onwards suggests that the reduction of the anode activity is probably due to the formation of the interfacial  $\text{TiO}_2$  passive layer. This increase in the resistance should be the cause of the trend of current density reduction observed in the potentiostatic test (Figure 5.1).

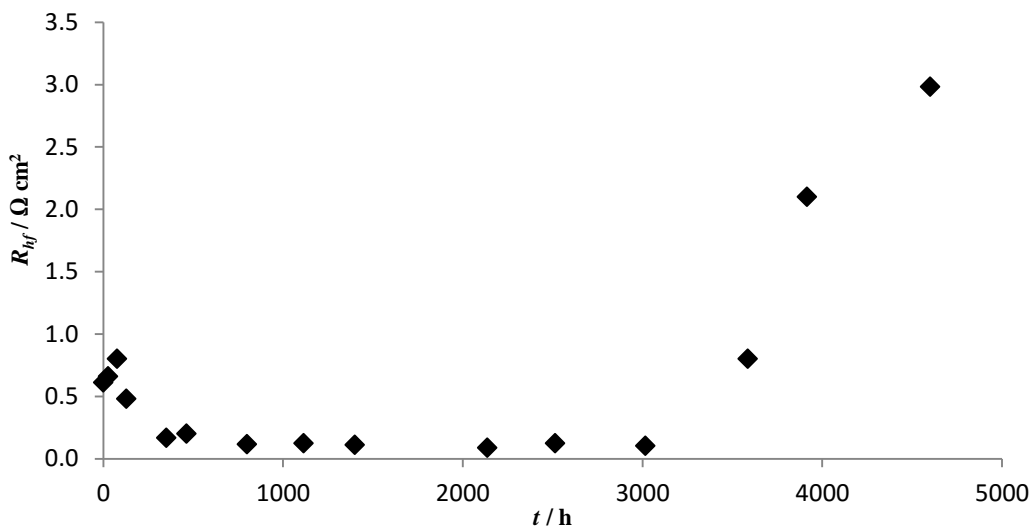
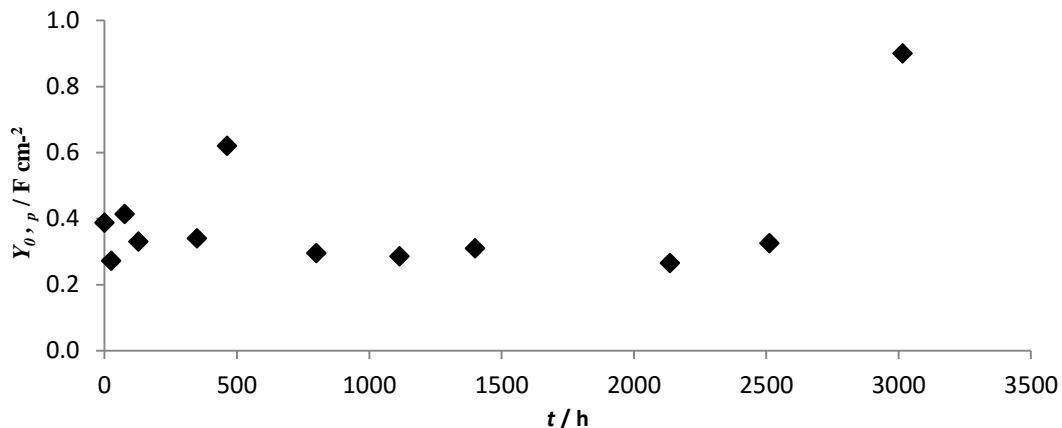


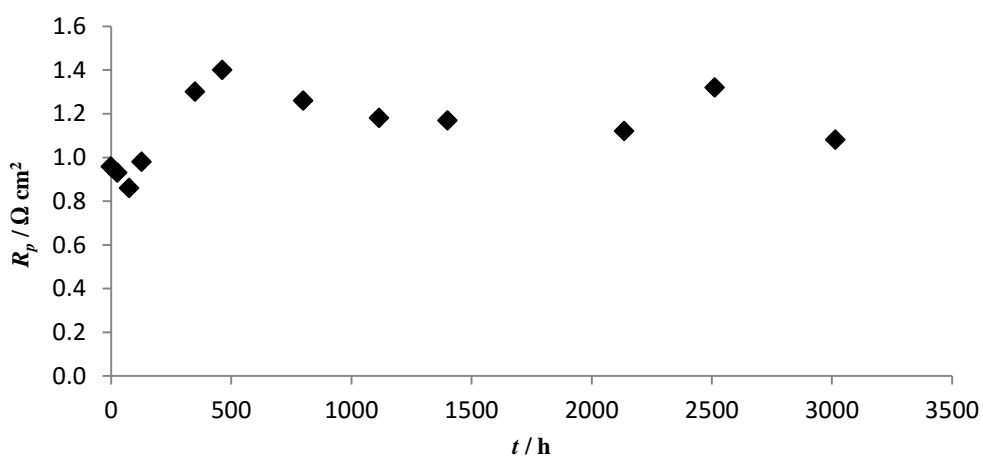
Figure 5.8 – Evolution of the high frequency resistance with the time of ageing test of DSA® anode in 5 mol dm<sup>-3</sup> NaCl solution

Figure 5.9 and Figure 5.10 show the low frequency capacitance, pseudocapacitance, ( $Y_{0,p}$ ) and resistance,  $R_p$ , histories obtained from the impedance spectra of the DSA® in 5 mol dm<sup>-3</sup> NaCl aqueous solutions (Figure 5.4). These parameters are related to the adsorption/ desorption of chloride intermediates and were only determined over the first 3000 h since from this time onwards the EEC used to fit the impedance of the electrode did not include these elements. The values obtained for the pseudocapacitance are constant over the whole range except for times 463 h and 3000 h which should be classified as outliers. The values of the CPE exponents obtained were in the range 0.55 – 0.75. Exponent values closer to 0.5 suggest significant surface non-uniformities with diffusional limitations of the species involved in the adsorption/desorption processes.



**Figure 5.9 – Evolution of the magnitude of the CPE used to describe the pseudocapacitance of the DSA<sup>®</sup> anode with the ageing time in 5 mol dm<sup>-3</sup> NaCl**

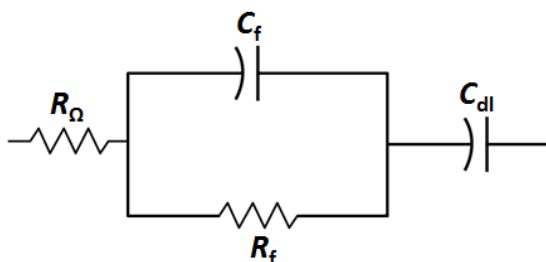
The low frequency resistance history, shown in Figure 5.10, was constant over the initial 128 h at ca. 0.9  $\Omega \text{ cm}^2$ , which is followed by an abrupt increase up to 1.4  $\Omega \text{ cm}^2$  at 463 h. This peak precedes a final period of slight and steadily decreasing of the resistance values up to reaching 1.1  $\Omega \text{ cm}^2$  at 3000 h. This result, as well the pseudocapacitance history, suggests that during the first 3000 h there is an excess of active sites, that despite its reduction in number (as suggested by the reduction of the double layer capacitance) does not hinder the adsorption of the chloride intermediates.



**Figure 5.10 - Evolution of the low frequency resistance of the DSA<sup>®</sup> anode with the ageing time in 5 mol dm<sup>-3</sup> NaCl**

In addition to the impedance measurements in the CIER, at 1.4 V vs NHE, the impedance was measured in the capacitive region of the DSA<sup>®</sup> anode at 0.5 V vs NHE. The information from these measurements can provide relevant data to complement the results obtained in the CIER region and contribute to identifying the main deactivation phenomena occurring on the DSA<sup>®</sup> anode under study. Figure 5.12 shows the complex plane spectra obtained for the DSA<sup>®</sup> anode in the capacitive region of the electrode – at 0.5 V vs NHE. Conversely to the spectra in the CIER (Figure 5.4), the spectra at 0.5 V vs NHE show a characteristic capacitive profile rather than a resistive behaviour. This spectral shape has been reported in several reports using EIS in the capacitive region of DSA<sup>®</sup> anodes [5, 7, 44, 47]. The spectra recorded at the final phase of the ageing test exhibit significant differences with respect to the spectra recorded at short ageing times. The main difference is the semicircle shape in the high frequency region of the spectra at longer times. This process is made clearer in Figure 5.13 that magnifies the high frequency region of the complex plane spectra in Figure 5.12. This semicircle is similar to the one observed at 1.4 V vs NHE for the same ageing times. This cross-information allows confirming that the impact of the deactivation process is observed in both the capacitive and faradaic regions of the DSA<sup>®</sup> anode. The spectra in the first part of the test were fitted using the EEC in Figure 5.11a. This circuit was used previously [35, 48] and includes elements to describe the double layer capacitance,  $C_{dl}$ , at lower frequencies and the impedance of the coating, represented by a parallel combination of the film pseudocapacitance,  $C_f$ , with the film resistance,  $R_f$ . For the case of spectra obtained at the end of the ageing test, the EEC that best fits the impedance spectra is shown in Figure 5.11b. This EEC is based on the EEC in Figure 5.11a, to which was added an additional RC to describe the impedance of the high frequency semicircle. The subscript  $TiO_2$  refers to the deactivation process due to the formation of the  $TiO_2$  passive layer.

a



b

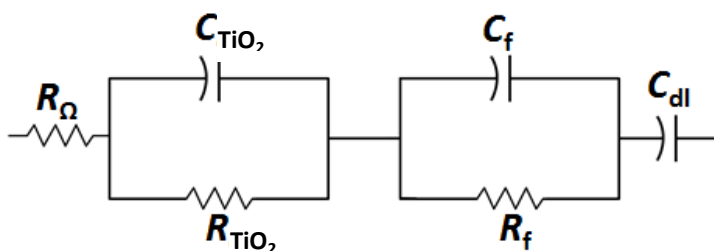


Figure 5.11 - EEC used to fit the impedance of the DSA<sup>®</sup> recorded at 0.5 V vs NHE at different stages of the ageing test. a – EEC used to fit the spectra recorded over the first 3000 h of the test; b – EEC used to fit the impedance spectra recorded from 3586 h onwards

Since the diameter of the high frequency semicircles is similar at 1.4 V vs NHE and 0.5 V vs NHE, one can conclude that it is not a faradaic process. The appearance of a semicircle at high frequencies, with the same diameter independent of the potential, in aged DSA<sup>®</sup> anodes has been already observed by Panić and co-authors [5] and Hoseinieh and co-authors [7]. However, this semicircle is not assigned directly to a specific deactivation mechanism and is associated with either the formation of a passive TiO<sub>2</sub> interlayer or the dissolution of the active species, depending on the operating conditions. At low frequencies, there is also a difference between the two sets of spectra. The spectra recorded during the initial phase of the test (0 h and 26 h) present a shape similar to an ideal capacitor with the exponent value around 0.95, whereas the spectra at the final phase of the test (3586 h and 4600 h) the value of the exponent is about to 0.89. These

values suggest that at greater ageing times, the electrolyte has already penetrated into the pores of the coating resulting in to a more non-uniform current distribution.

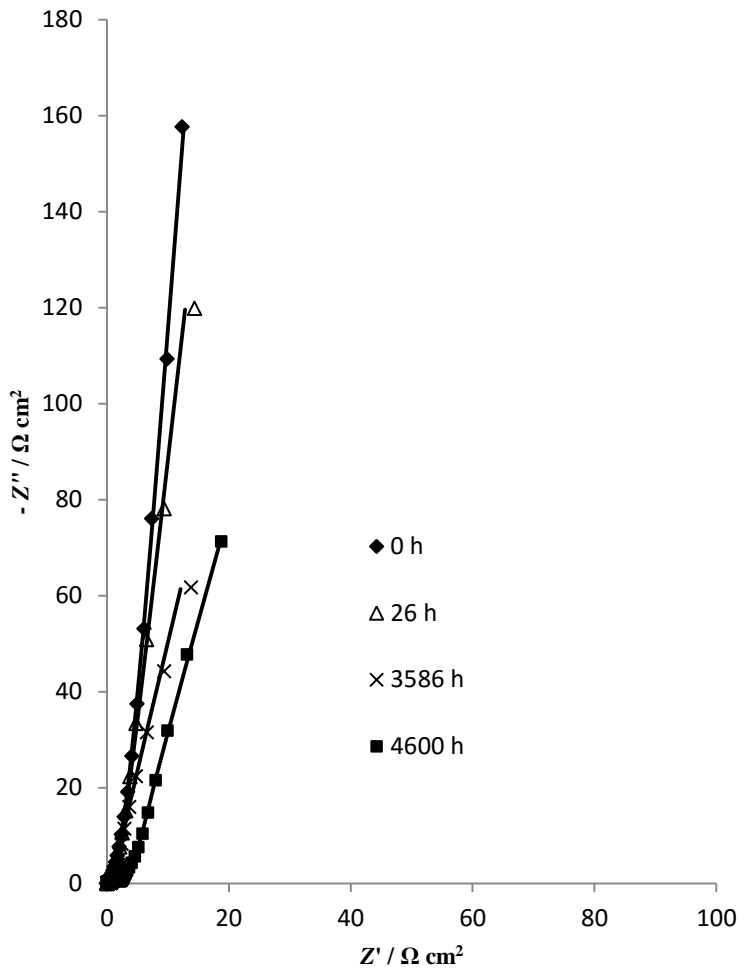


Figure 5.12 - Complex plane spectra for DSA® anode in 5 mol dm<sup>-3</sup> NaCl, pH 2 at 20 °C at 0.5 V vs NHE, recorded at different times during the ageing test. The dots are the experimental data and the lines correspond to fitting to the proposed electrical equivalent circuit model.

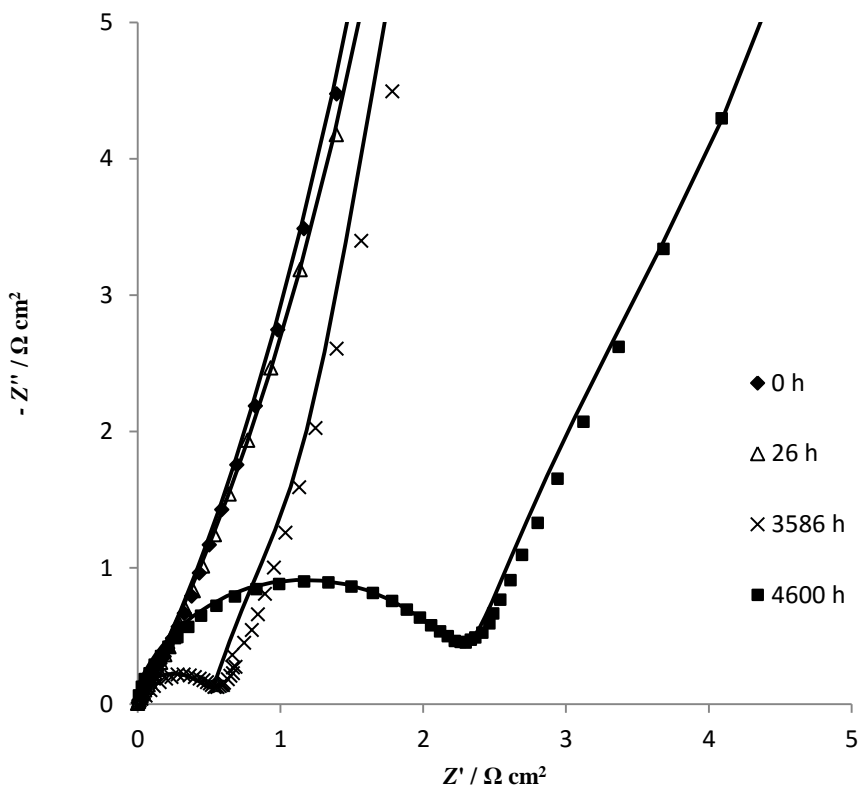


Figure 5.13 – Detail of high frequency region of the spectra in Figure 5.12

The parameters determined by the fitting of the spectra to the EEC are displayed in Table 5.1; since the ideal capacitors were replaced by CPE,  $Y_0$  is the magnitude of the CPE and  $n$  is the exponent. Subscripts  $f$ ,  $dl$  and  $d$  refer to film, double layer and deactivation, respectively.

The reduction of  $R_f$  from  $3.9 \Omega \text{ cm}^{-2}$  at the beginning of the test to  $0.43 \Omega \text{ cm}^{-2}$  at 3586 h suggests an increase in the global activity of the anode due to the penetration of electrolyte into the pores. This effect overcomes any deactivation processes that may simultaneously occur. Since the inner surface of the coating is fully available to the electrolyte, the electrode achieves its maximum activity, at close to 3586 h. From this time onwards, the film resistance increases due to deactivation of the anode, probably caused

by the dissolution of ruthenium and iridium oxides. These events are closely related to the evolution of the magnitude and exponent of the film CPE.

**Table 5.1 - Parameters of the EEC used to fit the impedance of the spectra obtained at different times**

	<b>0 h</b>	<b>26 h</b>	<b>3586 h</b>	<b>4600 h</b>
$R_f / \Omega \text{ cm}^{-2}$	3.9	2.5	0.43	2.0
$Y_{0,f} / \text{mF cm}^{-2} \text{ s}^{n-1}$	69.5	68.5	70.0	46.5
$n_f$	0.58	0.61	0.77	0.76
$Y_{0,dl} / \text{mF cm}^{-2} \text{ s}^{n-1}$	9.9	12.9	24.2	20.9
$n_{dl}$	0.96	0.94	0.89	0.88
$R_{\text{TiO}_2} / \Omega \text{ cm}^{-2}$			0.53	2.3
$Y_{0,\text{TiO}_2} / \text{mF cm}^{-2} \text{ s}^{n-1}$			0.18	0.16
$n_{\text{TiO}_2}$			0.89	0.84

Initially, the loss of activity is compensated by the increase in the available active area, which means that the CPE magnitude,  $Y_{0,f}$ , is almost unchanged. From 3586 h on, when the electrode has reached its maximum active surface area, the deactivation processes become noticeable leading to a reduction of the value of  $Y_{0,f}$ . The increase in the exponent of the film CPE from 0.60 to about 0.76 indicates that the surface non-uniformities due to electrode porosity are less pronounced as the test goes to the end. The increasing trend on the exponent of the film CPE could be an indication of more accessible inner layers of the coating due to pore widening over the initial phase of the test. The exponent reaches its maximum at ca. 3586 h, then becoming constant. This is in agreement with the findings reported by Panić [5].

The increase of the magnitude of the double layer capacitance,  $Y_{0,dl}$ , should also be related to penetration of the electrolyte into the coating pores until the maximum available area has been reached, which corresponds to the maximum value of the double layer capacitance. From 3586 h, the magnitude of the double layer capacitance starts to

decrease since the reduction of the electroactive sites with time is no longer compensated and masked by the increase in the active area.

The increase in  $R_{\text{TiO}_2}$  from  $0.53 \Omega \text{ cm}^{-2}$  at 3586 h to  $2.3 \Omega \text{ cm}^{-2}$  at 4600 h is an indication of the performance loss of the electrode. This is in agreement with the reduction of  $Y_{0,\text{TiO}_2}$  from  $0.18 \text{ mF cm}^{-2} \text{ s}^{-n-1}$  to  $0.16 \text{ mF cm}^{-2} \text{ s}^{-n-1}$  during the same period of time. This semicircle is probably related to oxidation of the titanium substrate. The deactivation mechanism of the anode should be a result of dissolution and mechanical losses of the active metal oxides (ruthenium and iridium oxides) and the formation of a passive  $\text{TiO}_2$  at the substrate-coating interface. Dissolution of the active metal oxides should occur right from the beginning of the test, although it was not detectable, probably because the simultaneous increase of active area. When the deeper regions of the coating are reached, the maximum active surface area is achieved; the electrolyte contacts the substrate leading to its oxidation. This oxidation began at around 3586 h and should be the main cause of the electrode performance loss.

## Surface characterization

The DSA<sup>®</sup> anode was periodically analysed by different surface characterisation techniques – scanning electron microscopy (SEM) coupled to energy dispersive spectroscopy (EDS) and X-Ray electron spectroscopy (XPS). These techniques provide information about the topography, morphology and elemental composition of the electrode.

### Scanning electron microscopy

Figure 5.14 shows SEM images taken at different times of the ageing test. Figure 5.14a shows a fresh sample of DSA<sup>®</sup> anode; the surface seems to comprise rough – typical mud-crack structure – and smooth regions. After 1855 h of ageing, an additional surface feature arises – Figure 5.14b, in which some parts of the coating seem to be removed. This coating detachment appears, however, to be superficial and only representing a small fraction of the total surface area. Significantly, severe damage is seen in Figure 5.14c and

Figure 5.14d, taken at 3015 h and 4600 h of ageing, respectively. The detached areas are not only a significant fraction of the total area but go deeper into the electrode surface. These images suggest that electrode erosion should have an active role in the deactivation of the DSA<sup>®</sup> anode. Contrary to dissolution of the active metal oxides, the erosion is not a selective process, contributing to the depletion of all active oxides; this way, the relative composition of the metal oxides in the coating should not vary significantly.

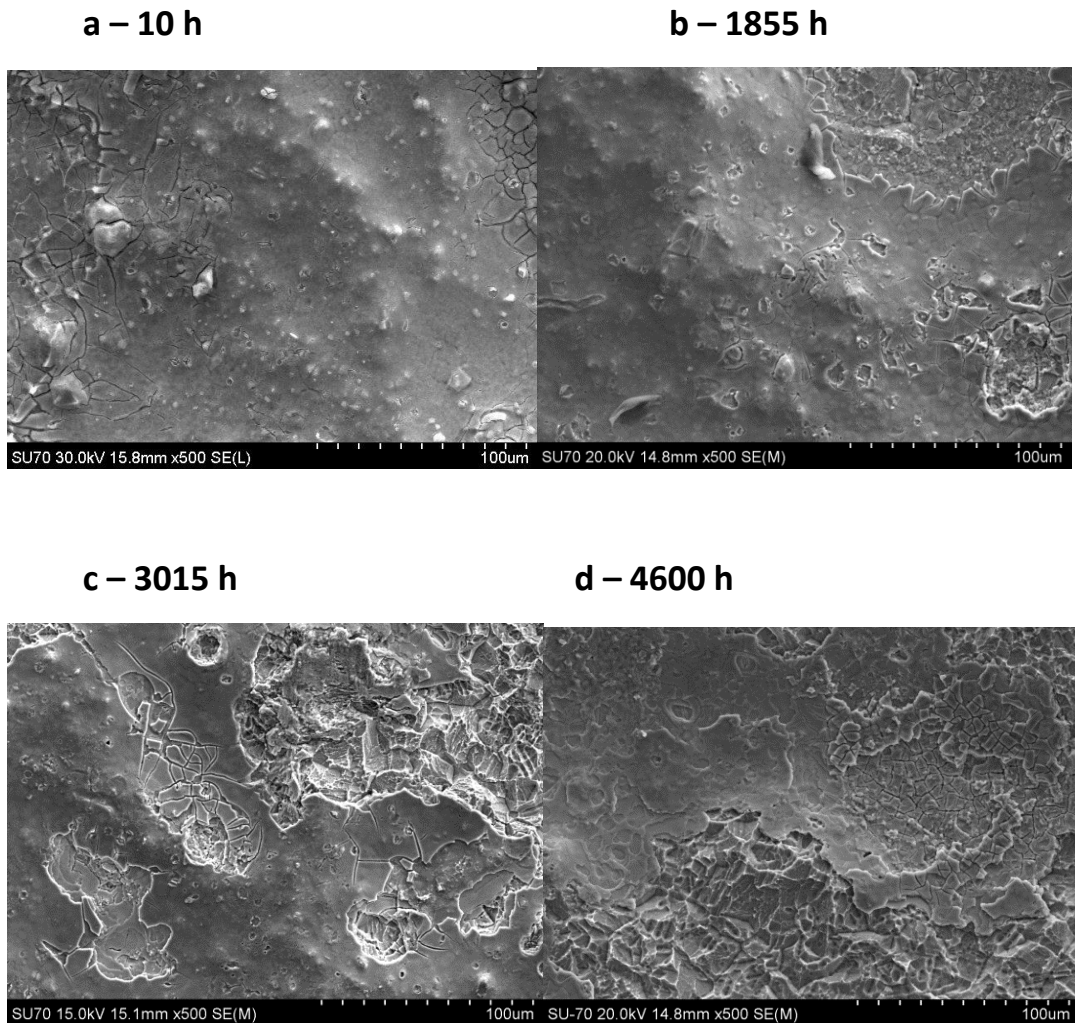


**Figure 5.14 – SEM images of DSA<sup>®</sup> anode taken at different times during the ageing test.**

### Energy Dispersive Spectroscopy

EDS measurements were performed coupled to SEM analyses. EDS provides semi-quantitative analysis of the top micrometric layers of the electrode. Figure 5.15 exhibits EDS mapping obtained before and at the end of the ageing test (4600 h). The elements under study, titanium, ruthenium and iridium are identified with red, green and blue colours respectively.

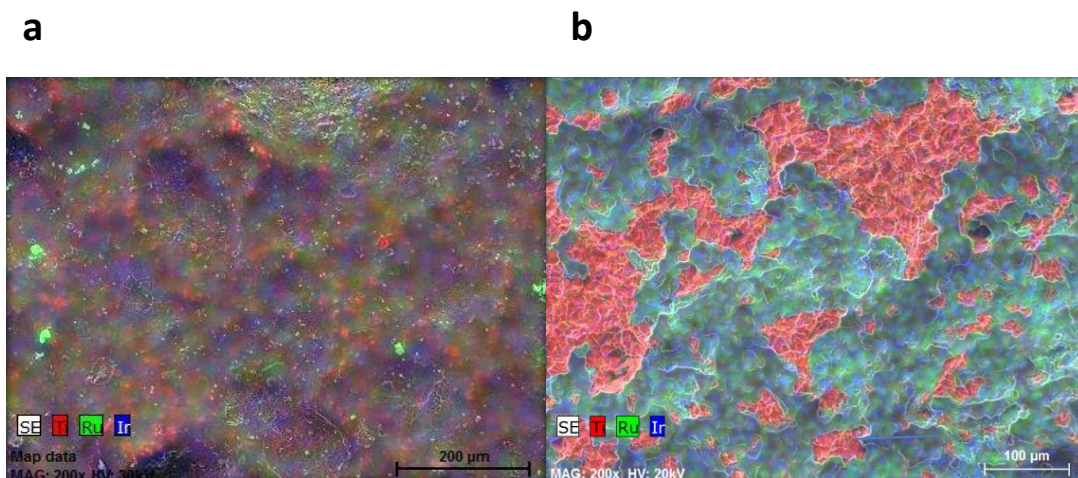


Figure 5.15 – X-Ray mapping image obtained by EDS. a – new anode; b – used anode (4600 h)

In Figure 5.15 a, the three elements are spread all over the image which is expected since the coating is made of oxides of these elements; the electrode substrate is completely covered with the coating. After 4600 h of test, two different types of surface composition are seen. While some areas of the image present a profile similar to the fresh anode, other areas exhibit a different pattern and only titanium is detected by EDS; this suggests that the coating was detached from the DSA<sup>®</sup> anode leading to exposure of the titanium substrate.

Based on EDS mapping, the relative composition of the three metals presented in the coating was determined at different times during the ageing test. The results obtained by EDS for the DSA<sup>®</sup> anode composition over the ageing test are shown in Table 5.2.

**Table 5.2 – Relative atomic composition of the DSA® anode surface composition obtained by EDS.**

Atomic fraction / %	Ageing time / h				
	0	463	1855	3015	4600
<b>Titanium</b>	79.3	84.5	85.7	91.0	93.7
<b>Ruthenium</b>	9.0	9.4	8.9	4.4	3.2
<b>Iridium</b>	11.7	6.1	5.4	4.6	3.0

Two general trends are observed from Table 5.2. On the one hand, the titanium fraction increases with time. On the other hand, the relative fraction of ruthenium and iridium decrease. Since titanium is present in the substrate and coating, this can be caused by two different deactivation processes: a) by the selective dissolution of ruthenium and iridium as soluble oxides and b) by erosion of the coating, removing ruthenium, iridium and titanium oxides simultaneously. Since the fresh coating thickness is in the same range as the EDS penetration depth (ca. 1-2  $\mu\text{m}$ ), the progressive erosion and detachment of the top layer should lead to a stronger titanium signal from the substrate. Over the first 1855 h of the test, the ruthenium composition is almost constant which indicates a low dissolution rate; however, from 1855 h to 3015 h the ruthenium fraction decreases by almost 50 %. This profile contrasts with the iridium profile that during the initial 463 h decreases by 39 %, stabilising afterwards. The variation of the ruthenium/iridium ratio over time suggests that selective dissolution of the metal oxides could also be a cause for DSA® deactivation. After 4600 h, the ruthenium fraction represents 35 % of the initial value and the iridium fraction is 26 % of the initial value, which represent a molar fraction 6.2 % of active metals. This value is very close to the value found by Hoseinieh and co-authors [8], who reported a total fraction of active metals (ruthenium and iridium fractions) of 6.8 %, and stated that this value is sufficient to keep the DSA® active. Hence, the main deactivation mechanism was assigned to the growth of a  $\text{TiO}_2$  layer. Based on the EDS results and on the information from impedance, the most likely cause for the deactivation of anode under study is the formation of  $\text{TiO}_2$  at the substrate-coating interface.

### X-Ray photoelectron spectroscopy

In addition to EDS, the surface composition of the DSA® anode was analysed by XPS. While EDS provides information up to a micrometre thickness, XPS provides a more superficial analysis up to a depth of 10 nm. The results obtained by XPS during the ageing test are shown in Table 5.3.

**Table 5.3 - Relative atomic composition of the DSA® anode surface composition obtained by XPS.**

Atomic fraction / %	Ageing time / h			
	0	1855	3015	4600
<b>Titanium</b>	86.2	91.5	97.0	95.2
<b>Ruthenium</b>	5.9	3.5	1.0	2.2
<b>Iridium</b>	7.9	5.0	2.0	2.6

For the first 3015 h, the results obtained by XPS corroborate the data obtained by EDS. The ruthenium and iridium atomic fractions decrease, while the titanium mass fraction increases. Contrary to the trend found in EDS analysis, the XPS results show a linear reduction of both ruthenium and iridium atomic fractions, while the titanium atomic fraction increases linearly with time. At 3015 h, the iridium atomic fraction is 17 % and the ruthenium atomic fraction is 25 % of their initial values. These are faster decreases than what was observed by EDS and support a loss of activity via detachment of the coating rather than selective dissolution of the metals. The results at 4600h show, however, an inversion in the trend of the atomic fraction of the three elements evaluated i.e. an increase of the ruthenium and iridium and a decrease of the titanium mass fractions in relation to 3015 h. This can be attributed to a decrease of the iridium and ruthenium dissolution rate due to lower metal content in the sample or can be caused by the reduced number of sampling regions. As shown in Figure 5.15, at the end of the test, a significant area of the substrate is still covered with coating. Since only two regions were evaluated, the results could be biased and not be representative of the full electrode surface.

## 5.5 Conclusions

The ageing experiment carried out over 4600 h at high current densities confirms the stability of the DSA<sup>®</sup> anode used during the chlorine evolution reaction. The first signs of electrode degradation were detected by electrochemical measurements after 3586 h. At this ageing time, the potentiostatic and cyclic voltammetry analyses suggested a slight reduction of the electrode activity, while EIS analysis shows a significant change in the spectra. Based on EIS analysis, three anode deactivation mechanisms were proposed – the selective dissolution of ruthenium and iridium, coating erosion and the formation of a passive TiO<sub>2</sub> coating-substrate interlayer. EDS and XPS demonstrate the loss of iridium and ruthenium over the ageing test, although the main process of DSA<sup>®</sup> anode deactivation was assigned to the formation of a passive TiO<sub>2</sub> interlayer. This is supported by the appearance of a high frequency semicircle in impedance spectra after 3586 h of ageing, that coincides with the beginning of a decrease of the current density.

## 5.6 References

1. Beer, H.B., Patent GB 1147442, (1965).
2. Trasatti, S., *Electrocatalysis: understanding the success of DSA<sup>®</sup>*. *Electrochimica Acta*, 2000. **45**(15-16): p. 2377-2385.
3. Xu, L.K. and J.D. Scantlebury, *A study on the deactivation of an IrO<sub>2</sub>-Ta<sub>2</sub>O<sub>5</sub> coated titanium anode*. *Corrosion Science*, 2003. **45**(12): p. 2729-2740.
4. O'Brien, T.F., T.V. Bommaraju, and F. Hine, *Handbook of chlor-alkali technology*. 2005, New York: Springer.
5. Panić, V.V., et al., *On the deactivation mechanism of RuO<sub>2</sub>-TiO<sub>2</sub>/Ti anodes prepared by the sol-gel procedure*. *Journal of Electroanalytical Chemistry*, 2005. **579**(1): p. 67-76.
6. Panić, V.V., et al., *The influence of the aging time of RuO<sub>2</sub> sol on the electrochemical properties of the activated titanium anodes obtained by sol-gel procedure in Trends in Advanced Materials and Processes*, D.P. Uskokovic, et al., Editors. 2000, Trans Tech Publications Ltd: Zurich-Uetikon. p. 117-122.
7. Hoseinieh, S.M. and F. Ashrafizadeh, *Influence of electrolyte composition on deactivation mechanism of a Ti/Ru<sub>0.25</sub>Ir<sub>0.25</sub>Ti<sub>0.5</sub>O<sub>2</sub> electrode*. *Ionics*, 2013. **19**(1): p. 113-125.
8. Hoseinieh, S.M., F. Ashrafizadeh, and M.H. Maddahi, *A Comparative Investigation of the Corrosion Behavior of RuO<sub>2</sub>-IrO<sub>2</sub>-TiO<sub>2</sub> Coated Titanium Anodes in Chloride Solutions*. *Journal of the Electrochemical Society*, 2010. **157**(4): p. E50-E56.
9. Godwin, I. and M.E.G. Lyons, *Dimensionally Stable Anodes (DSA<sup>®</sup>) for Electrochemical Water Splitting: Redox Properties, OER Kinetics and Mechanism at RuO<sub>2</sub>/NiO Modified Electrodes in Aqueous Base*. *ECS Transactions*, 2013. **53**(23): p. 21-31.
10. Naslund, L.A., et al., *The Role of TiO<sub>2</sub> Doping on RuO<sub>2</sub>-Coated Electrodes for the Water Oxidation Reaction*. *Journal of Physical Chemistry C*, 2013. **117**(12): p. 6126-6135.
11. Hu, J.M., J.Q. Zhang, and C.N. Cao, *Oxygen evolution reaction on IrO<sub>2</sub>-based DSA<sup>®</sup> type electrodes: kinetics analysis of Tafel lines and EIS*. *International Journal of Hydrogen Energy*, 2004. **29**(8): p. 791-797.
12. Wu, W.Y., Z.H. Huang, and T.T. Lim, *Recent development of mixed metal oxide anodes for electrochemical oxidation of organic pollutants in water*. *Applied Catalysis a-General*, 2014. **480**: p. 58-78.
13. Chatzisyneon, E., et al., *Electrochemical treatment of textile dyes and dyehouse effluents*. *Journal of Hazardous Materials*, 2006. **137**(2): p. 998-1007.
14. Comninellis, C. and A. Nerini, *Anodic-oxidation of phenol in the presence of NaCl for waste-water treatment*. *Journal of Applied Electrochemistry*, 1995. **25**(1): p. 23-28.
15. Terezo, A.J. and E.C. Pereira, *Preparation and characterization of Ti/RuO<sub>2</sub>-Nb<sub>2</sub>O<sub>5</sub> electrodes obtained by polymeric precursor method*. *Electrochimica Acta*, 1999. **44**(25): p. 4507-4513.

16. Cao, H., et al., *Novel Sb-doped ruthenium oxide electrode with ordered nanotube structure and its electrocatalytic activity toward chlorine evolution*. *Electrochimica Acta*, 2013. **91**: p. 234-239.
17. Santana, M.H.P. and L.A. De Faria, *Oxygen and chlorine evolution on RuO<sub>2</sub> + TiO<sub>2</sub> + CeO<sub>2</sub> + Nb<sub>2</sub>O<sub>5</sub> mixed oxide electrodes*. *Electrochimica Acta*, 2006. **51**(17): p. 3578-3585.
18. Profeti, D., T.A.F. Lassali, and P. Olivi, *Preparation of Ir<sub>0.3</sub>Sn<sub>(0.7-x)</sub>Ti<sub>x</sub>O<sub>2</sub> electrodes by the polymeric precursor method: Characterization and lifetime study*. *Journal of Applied Electrochemistry*, 2006. **36**(8): p. 883-888.
19. Panić, V.V., et al., *Capacitive properties of RuO<sub>2</sub>-coated titanium electrodes prepared by the alkoxide ink procedure*. *Journal of Electroanalytical Chemistry*, 2007. **609**(2): p. 120-128.
20. Panić, V.V., et al., *The effect of the addition of colloidal iridium oxide into sol-gel obtained titanium and ruthenium oxide coatings on titanium on their electrochemical properties*. *Physical Chemistry Chemical Physics*, 2010. **12**(27): p. 7521-7528.
21. Schmittinger, P., et al., *Chlorine in Ullmann's Encyclopedia of Industrial Chemistry, Electronic release*, B. Elvers, Editor. 2012, Wiley-VCH: Weinheim. p. 531-621.
22. Yi, Z., et al., *Effect of IrO<sub>2</sub> loading on RuO<sub>2</sub>-IrO<sub>2</sub>-TiO<sub>2</sub> anodes: A study of microstructure and working life for the chlorine evolution reaction*. *Ceramics International*, 2007. **33**(6): p. 1087-1091.
23. Silva, L.M.d., L.A.d. Faria, and J.F.C. Boodts, *Electrochemical impedance spectroscopic (EIS) investigation of the deactivation mechanism, surface and electrocatalytic properties of Ti/RuO<sub>2</sub>(x)+Co<sub>3</sub>O<sub>4</sub>(1-x) electrodes*. *Journal of Electroanalytical Chemistry*, 2002. **532**(1-2): p. 141-150.
24. Lassali, T.A.F., J.F.C. Boodts, and L.O.S. Bulhões, *Faradaic impedance investigation of the deactivation mechanism of Ir-based ceramic oxides containing TiO<sub>2</sub> and SnO<sub>2</sub>*. *Journal of Applied Electrochemistry*, 2000. **30**(5): p. 625-634.
25. Cardarelli, F., et al., *Preparation of oxygen evolving electrodes with long service life under extreme conditions*. *Journal of Applied Electrochemistry*, 1998. **28**(3): p. 245-250.
26. Panić, V.V. and B.Ž. Nikolić, *Sol-gel prepared active ternary oxide coating on titanium in cathodic protection*. *Journal of the Serbian Chemical Society*, 2007. **72**(12): p. 1393-1402.
27. Fathollahi, F., et al., *Comparison of morphology, stability and electrocatalytic properties of Ru<sub>0.3</sub>Ti<sub>0.7</sub>O<sub>2</sub> and Ru<sub>0.3</sub>Ti<sub>0.4</sub>Ir<sub>0.3</sub>O<sub>2</sub> coated titanium anodes*. *Russian Journal of Electrochemistry*, 2011. **47**(11): p. 1281-1286.
28. Chen, S., et al., *Ti/RuO<sub>2</sub>-Sb<sub>2</sub>O<sub>5</sub>-SnO<sub>2</sub> electrodes for chlorine evolution from seawater*. *Chemical Engineering Journal*, 2011. **172**(1): p. 47-51.
29. Hu, J.M., et al., *Degradation mechanism of long service life Ti/IrO<sub>2</sub>-Ta<sub>2</sub>O<sub>5</sub> oxide anodes in sulphuric acid*. *Corrosion Science*, 2002. **44**(8): p. 1655-1668.

30. Alves, V.A., L.A.d. Silva, and J.F.C. Boodts, *Electrochemical impedance spectroscopic study of dimensionally stable anode corrosion*. Journal of Applied Electrochemistry, 1998. **28**(9): p. 899-905.
31. Pilla, A.S., et al., *Evaluation of anode deactivation in chlor-alkali cells*. Journal of Applied Electrochemistry, 1997. **27**(11): p. 1283-1289.
32. Martelli, G.N., R. Ornelas, and G. Faita, *Deactivation mechanisms of oxygen evolving anodes at high current densities*. Electrochimica Acta, 1994. **39**(11–12): p. 1551-1558.
33. Loučka, T., *The reason for the loss of activity of titanium anodes coated with a layer of RuO<sub>2</sub> and TiO<sub>2</sub>*. Journal of Applied Electrochemistry, 1977. **7**(3): p. 211-214.
34. Loucka, T., *The reasons for the loss of activity of titanium-ruthenium dioxide anodes in sulphuric acid media*. Journal of Applied Electrochemistry, 1981. **11**(2): p. 143-144.
35. Alves, V.A., L.A.d. Silva, and J.F.C. Boodts, *Surface characterisation of IrO<sub>2</sub>/TiO<sub>2</sub>/CeO<sub>2</sub> oxide electrodes and Faradaic impedance investigation of the oxygen evolution reaction from alkaline solution*. Electrochimica Acta, 1998. **44**(8-9): p. 1525-1534.
36. Hine, F., et al., *Electrochemical behavior of the oxide-coated metal anodes*. Journal of the Electrochemical Society, 1979. **126**(9): p. 1439-1445.
37. Vercesi, G.P., et al., *Characterization of dsa-type oxygen evolving electrodes. Choice of base metal*. Thermochemica Acta, 1991. **176**: p. 31-47.
38. Comninellis, C. and G.P. Vercesi, *Characterization of DSA-type oxygen evolving electrodes: choice of a coating*. Journal of Applied Electrochemistry, 1991. **21**(4): p. 335-345.
39. Li, F.-B., A. Robert Hillman, and S.D. Lubetkin, *A new approach to the mechanism of chlorine evolution: Separate examination of the kinetic steps using ac impedance on a rotating thin ring electrode*. Electrochimica Acta, 1992. **37**(15): p. 2715-2723.
40. Conway, B.E. and P. Gu, *Evaluation of Cl adsorption in anodic Cl<sub>2</sub> evolution at Pt by means of impedance and potential-relaxation experiments. Influence of the state of surface oxidation of the Pt*. Journal of the Chemical Society-Faraday Transactions, 1991. **87**(17): p. 2705-2714.
41. Jovanović, V.M., et al., *The roles of the ruthenium concentration profile, the stabilizing component and the substrate on the stability of oxide coatings*. Journal of Electroanalytical Chemistry, 1992. **339**(1): p. 147-165.
42. N/A, *Knovel Sampler*. Knovel.
43. Bommaraju, T.V., C.P. Chen, and V.I. Birss, *Deactivation of Thermally Formed RuO<sub>2</sub> + TiO<sub>2</sub> Coatings During Chlorine Evolution: Mechanisms and Reactivation Measures in Modern Chlor-Alkali Technology*. 2007, Blackwell Science Ltd. p. 57-81.
44. Ribeiro, J. and A.R. de Andrade, *Investigation of the electrical properties, charging process, and passivation of RuO<sub>2</sub>-Ta<sub>2</sub>O<sub>5</sub> oxide films*. Journal of Electroanalytical Chemistry, 2006. **592**(2): p. 153-162.

45. Tilak, B.V., et al., *Deactivation of thermally formed Ru/Ti oxide electrodes - An AC impedance characterization study*. Journal of the Electrochemical Society, 2001. **148**(9): p. D112-D120.
46. Krysa, J., et al., *Effect of coating thickness and surface treatment of titanium on the properties of IrO<sub>2</sub>-Ta<sub>2</sub>O<sub>5</sub> anodes*. Journal of Applied Electrochemistry, 1996. **26**(10): p. 999-1005.
47. Lassali, T.A.F., J.F.C. Boodts, and L.O.S. Bulhões, *Charging processes and electrocatalytic properties of IrO<sub>2</sub>/TiO<sub>2</sub>/SnO<sub>2</sub> oxide films investigated by in situ AC impedance measurements*. Electrochimica Acta, 1999. **44**(24): p. 4203-4216.
48. Malpass, G.R.P., R.S. Neves, and A.J. Motheo, *A comparative study of commercial and laboratory-made Ti/Ru<sub>0.3</sub>Ti<sub>0.7</sub>O<sub>2</sub> DSA<sup>®</sup> electrodes: "In situ" and "ex situ" surface characterisation and organic oxidation activity*. Electrochimica Acta, 2006. **52**(3): p. 936-944.



## 6 Conclusions and future work

The DSA<sup>®</sup> anode is a critical element of chlor-alkali cells since it is coated with the oxides of expensive noble metals such as iridium oxide and ruthenium oxide. The extension of its lifetime is thus of great relevance for chlorine producers, although the energy consumption and the risk of abrupt failure of an anode whilst under operation make the producers act prudently. Anodes are, therefore, replaced mostly according to the recommendations of the suppliers.

The research described in this thesis concerned the electrochemical characterisation, particularly by electrochemical impedance spectroscopy, of DSA<sup>®</sup> anodes and relating the electrochemical response to the DSA<sup>®</sup> anode performance. Electrochemical impedance spectroscopy is a powerful, highly sensitive electrochemical technique that, in order to give meaningful results, needs to be used with correctly designed electrochemical cells. A new electrochemical cell was designed, evaluated and optimised for studying the chlorine evolution reaction on DSA<sup>®</sup> anodes. In this cell, the anode was placed horizontally in the cell bottom and the electrolyte was mechanically stirred in order to keep the electrode surface free from gas bubbles, even at high current densities (up to 140 mA cm<sup>-2</sup>). This design allowed recording clean impedance spectra with low disturbance from bubble formation, allowing reliable information to be extracted concerning the state of the DSA<sup>®</sup> anode during intense chlorine production.

The designed cell was then used to study the kinetics of chlorine evolution on a commercial TiO<sub>2</sub>-RuO<sub>2</sub>-IrO<sub>2</sub> DSA<sup>®</sup> anode. The impedance spectra obtained at different potentials clearly showed the role of adsorption of intermediates by a well-defined semicircle at low frequencies. Based on the analysis of data from the impedance spectra and from polarisation curves it was concluded that the chlorine evolution reaction on the DSA<sup>®</sup> anode under study is well described by a Volmer-Tafel-Heyrovsky mechanism with an equilibrium Volmer step,  $K_1 = 3.8 \times 10^{-2}$ . This step is mostly followed by the Tafel step,  $k_3 = 1.2 \times 10^{-6} \text{ mol cm}^{-2} \text{ s}^{-1}$ , although the Heyrovsky step,  $k_2 = 9.1 \times 10^{-8} \text{ mol cm}^{-2} \text{ s}^{-1}$ , could

not be neglected. This was the first stage of a more comprehensive study of the chlorine evolution reaction (CIER) on DSA® anodes. Further studies should include the effect of pH and sodium chloride concentration.

The electrochemical response of the DSA® anode during an ageing test showed the high stability of the DSA® anode, the activity of which remained unchanged during the first 3586 h. The anode kept its electrochemical activity despite the progressive loss of the active metal oxides, ruthenium and iridium oxides, shown by EDS and XPS analyses. Based on the information from SEM, EDS, XPS, EIS and CV, a mechanism of anode deactivation, comprising three different processes, was proposed. During the first stage of the test the anode degradation occurs by coating erosion and by dissolution of ruthenium and iridium: these processes cause the widening of the coating pores that promote the penetration of electrolyte through the coating and thence an increase in electrode active area, which compensates the dissolution and erosion. The electrolyte eventually reaches the titanium substrate, at around 3600 h, causing its oxidation to titanium dioxide. The TiO<sub>2</sub> layer formed at the coating-substrate interface is seen to be the main deactivation mechanism of the DSA® anode. The growth of a TiO<sub>2</sub> layer at the coating-substrate interface was manifested by a high frequency semicircle appearing in the impedance spectra over the last phase of the test.

The accelerated ageing test was interrupted after 4600 h of operation when the loss of anode activity was already noticeable. More severe accelerated ageing test conditions should be evaluated and assessed, in order to decrease the experimentation time. To keep the focus on chlorine evolution, it is recommended that the sodium chloride concentration is not varied in these future experiments. The acceleration of the deactivation mechanism should be achieved by increasing the temperature to 90 °C and increasing the current density up to values around 4 A cm<sup>-2</sup>. Once the duration of the tests is reduced, a set of ageing experiments that investigate the influence of the most important process variables on the anode deactivation mechanism should be carried out. Assessing the effect of pH and electrolyte impurities is of great importance and could add

valuable information to improve the understanding of the deactivation mechanism proposed in this work.

Despite the fact that oxygen is known to be an important side reaction of the chlorine evolution reaction, its contribution was considered to be negligible. To evaluate the selectivity of the DSA<sup>®</sup> anode for chlorine evolution reaction and the impact of the oxygen evolution reaction, it is suggested that in future experiments the outlet gas composition is analysed by gas chromatography.

The effect of the pH has been mentioned as a critical variable in the chlorine/oxygen production ratio. To control this important variable, the electrochemical cell should be equipped with a pH controller. Also temperature controllers should be introduced in the cell to reduce the temperature fluctuations during the ageing tests.

The work described in this thesis provides relevant information on the kinetics and ageing mechanism of commercial DSA<sup>®</sup> anodes. Based on the newly developed electrochemical cell, EIS can be increasingly used to evaluate the behaviour of components of industrial chlor-alkali cells. This technique can be used as an offline supporting technique to monitor the performance of unmounted DSA<sup>®</sup> anodes. During this work, the optimisation of the conditions for characterising DSA<sup>®</sup> anodes was achieved. These findings are an important step towards carrying out more comprehensive studies that will help to decide the optimum time for replacement or recoating of DSA<sup>®</sup> anodes in industrial installations.

